



*Università degli studi di Cagliari
Dept. of Electrical and Electronic Engineering
Ph.D. in Electronic and Computer Engineering
XXXII Cycle*

Development of a Novel Dataset and Tools for Non-Invasive Fetal Electrocardiography Research

Scientific Disciplinary Sector: ING-INF/06

Eleonora Sulas

Ph.D. Coordinator: Prof. Alessandro Giua

Advisors: Dr. Danilo Pani

Prof. Luigi Raffo

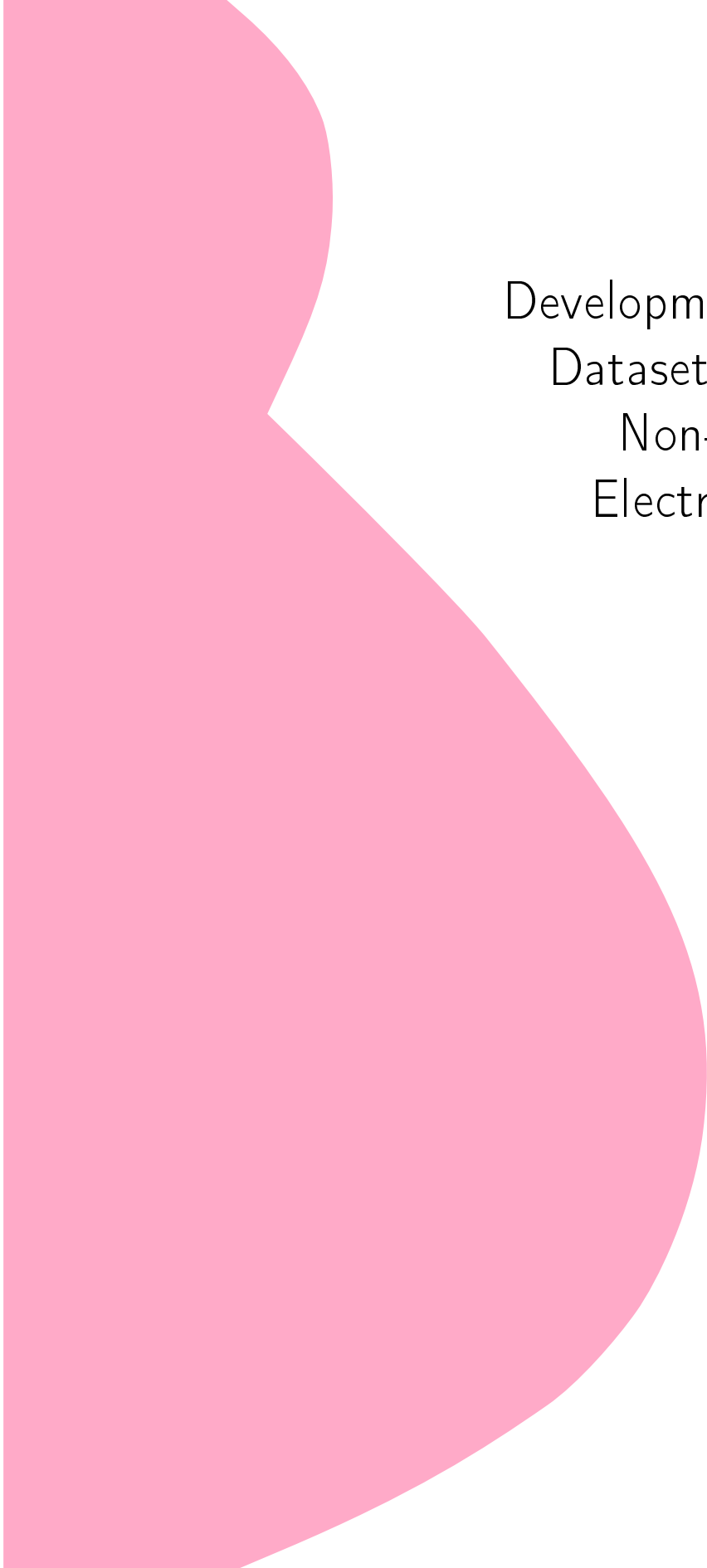
Final exam. Academic Year 2018 – 2019

Thesis defence: February 2020 Session



Eleonora Sulas gratefully acknowledges Sardinian Regional Government for the financial support of her/his PhD scholarship (P.O.R. Sardegna F.S.E. - Operational Programme of the Autonomous Region of Sardinia, European Social Fund 2014-2020 - Axis III Education and training, Thematic goal 10, Investment Priority 10ii, Specific goal 10.5).

Questa Tesi può essere utilizzata, nei limiti stabiliti dalla normativa vigente sul Diritto d'Autore (Legge 22 aprile 1941 n. 633 e succ. modificazioni e articoli da 2575 a 2583 del Codice civile) ed esclusivamente per scopi didattici e di ricerca; è vietato qualsiasi utilizzo per fini commerciali. In ogni caso tutti gli utilizzi devono riportare la corretta citazione delle fonti. La traduzione, l'adattamento totale e parziale, sono riservati per tutti i Paesi. I documenti depositati sono sottoposti alla legislazione italiana in vigore nel rispetto del Diritto di Autore, da qualunque luogo essi siano fruiti.

A large, abstract, light pink shape occupies the left side of the page, extending from the top to the bottom. It has a curved, organic form, resembling a stylized letter 'S' or a similar shape, with a smooth gradient and a soft, rounded edge.

Development of a Novel Dataset and Tools for Non-Invasive Fetal Electrocardiography Research

Eleonora Sulas

Abstract

This PhD thesis presents the development of a novel open multi-modal dataset for advanced studies on fetal cardiological assessment, along with a set of signal processing tools for its exploitation. The Non-Invasive Fetal Electrocardiography (ECG) Analysis (NInFEA) dataset features multi-channel electrophysiological recordings characterized by high sampling frequency and digital resolution, maternal respiration signal, synchronized fetal trans-abdominal pulsed-wave Doppler (PWD) recordings and clinical annotations provided by expert clinicians at the time of the signal collection. To the best of our knowledge, there are no similar dataset available.

The signal processing tools targeted both the PWD and the non-invasive fetal ECG, exploiting the recorded dataset. About the former, the study focuses on the processing aimed at the preparation of the signal for the automatic measurement of relevant morphological features, already adopted in the clinical practice for cardiac assessment. To this aim, a relevant step is the automatic identification of the complete and measurable cardiac cycles in the PWD videos: a rigorous methodology was deployed for the analysis of the different processing steps involved in the automatic delineation of the PWD envelope, then implementing different approaches for the supervised classification of the cardiac cycles, discriminating between complete and measurable vs. malformed or incomplete ones. Finally, preliminary measurement algorithms were also developed in order to extract clinically relevant parameters from the PWD.

About the fetal ECG, this thesis concentrated on the systematic analysis of the adaptive filters performance for non-invasive fetal ECG extraction processing, identified as the reference tool throughout the thesis. Then, two studies

are reported: one on the wavelet-based denoising of the extracted fetal ECG and another one on the fetal ECG quality assessment from the analysis of the raw abdominal recordings.

Overall, the thesis represents an important milestone in the field, by promoting the open-data approach and introducing automated analysis tools that could be easily integrated in future medical devices.

Contents

List of Figures	xi
List of Tables	xvii
1 Introduction	1
1.1 Motivation	1
1.2 Thesis outline	2
2 Fetal cardiac diagnosis and monitoring	5
2.1 Fetal cardiocirculatory system development	6
2.1.1 Pathology	8
2.2 Fetal cardiac diagnosis and monitoring tools	10
2.3 ECG-based technologies	11
2.3.1 Basic principles of ECG	11
2.3.2 Heart Rate variability	16
2.3.3 Fetal ECG-based technologies	17
2.3.4 Fetal monitoring during labour	18
2.4 Ultrasound-based technologies	19
2.4.1 Physical Principles	19
2.4.2 Doppler Ultrasound	21
2.4.3 Important Parameters	24
3 Methods and tools for fetal ECG and Doppler analysis	29
3.1 Non-invasive fetal ECG	30

3.1.1	Fetal ECG signal processing issues	30
3.1.2	Available Datasets	31
3.1.3	Signal preprocessing	35
3.1.4	Signal processing techniques	36
3.1.5	Signal post-processing	37
3.1.6	Signal quality assessment	37
3.1.7	Fetal ECG cardiac time intervals	42
3.2	Fetal Ultrasound	43
3.2.1	Doppler signal processing	43
3.2.2	Extraction of the PWD doppler	44
3.3	Studies relating fetal ECG and Doppler	45
3.4	Conclusion	47
4	Development of a novel multimodal dataset	49
4.1	Rationale	50
4.2	Acquisition protocol	50
4.3	Study Population	51
4.4	PWD signal acquisition	52
4.4.1	PWD processing	53
4.5	Fetal ECG and maternal respiration signal acquisition	54
4.6	Multimodal synchronisation	56
4.7	Dataset quality assessment	58
4.8	Conclusion	60
5	PWD processing and classification	69
5.1	Study population	70
5.2	Rationale	70
5.3	Dataset labelling	71
5.4	Background	72
5.5	Materials and Methods	75
5.5.1	PWD envelope extraction chain	75
5.5.2	PWD automatic classification	86
5.5.3	Parameters and indexes from Doppler Ultrasound	91
5.6	Performance assessment	94

5.7	Results and discussion	95
5.7.1	PWD envelope extraction chain	96
5.7.2	PWD automatic classification	98
5.7.3	Parameters and indexes from Doppler Ultrasound	99
5.8	Conclusion	101
6	Non-invasive fECG extraction	113
6.1	Rationale	114
6.2	Background	116
6.3	Materials and Methods	116
6.3.1	MECG cancellation by RLS adaptive filter	116
6.3.2	Wavelet denoising	123
6.3.3	Signal Quality Assessment	128
6.3.4	Adopted Dataset	131
6.4	Comparative analysis methods	137
6.5	Results	143
6.6	Conclusion	153
7	Conclusion	159
	Bibliography	161
	Acknowledgments	193
	Curriculum Vitae	195

List of Figures

2.1	Fetus Heart Development. [93]	6
2.2	Changes in sodium and potassium conductance during the course of the action potential. [75]	12
2.3	Rhythmical action potentials from a Purkinje fiber and from a ventricular muscle fiber. [75]	13
2.4	The transmission of the cardiac impulse through the human heart, leading to the known electrocardiography waveform. [75] .	14
2.5	Apical 5-chamber view of the fetal heart.	22
2.6	A PWD velocity image obtained using an apical 5-chamber window.	23
2.7	The sketch of the AV activity with identification of the main waveform components and intervals.	24
2.8	Fetal heart rate measured considering the peak of the ventricular activity.	24
2.9	E and A peaks in the PWD trace.	25
2.10	AV interval.	26
2.11	MPI index.	27
3.1	Amplitude and frequency characteristics of biopotentials and artifacts that are present in the fetal ECG recording.	31
3.2	Functional timings in fetal ECG and PWD envelopes.	46
4.1	Chosen dataset electrode positioning.	56
4.2	Matlab interface for synchronisation of the two traces.	57

4.3 Results for the comparison between the fetal HRs obtained from the fECG and from the PWD. 61

4.4 Example of synchronized fetal ECG and PWD signals. 62

4.5 Comparison of the dataset electrode positioning and state-of-the-art electrode positioning. 63

5.1 Labelling examples. 72

5.2 Matlab interface to annotate the PWD images and envelopes. . . 73

5.3 Column-wise, the different processing steps in the workflow for the extraction of the Doppler velocity envelope. The shaded boxes in the central row indicate the chosen prototypical processing chain, and the unshaded boxes indicate the available options evaluated in this study. 78

5.4 The different toolchains studied in this work. 86

5.5 Automatic detection methods. 88

5.6	a) Step 1: Image preprocessing 1, b) Step 2: image preprocessing 2, c) Step 3: image binarization, d) Step 4: image post-processing, e) Step 5: envelope extraction, f) Step 6: envelope post-processing, g) all tests in a zoom range between 40 and 100%, h) all tests in a zoom between 90 and 100%. The box-plots are divided according to the type of processing phase, and, in each one, the rightmost boxplot always shows the accuracy of the MC. Order: 1. MC with no filter application for image preprocessing 1; 2. MC using as an intensity adjustment the subtraction of the greyscale and modified images; 3. MC using no operation for the image preprocessing 2; 4. MC using Canny algorithm; 5. MC using NLLAP edge detector (NL); 6. MC using a combination of the NLLAP and Sobel edge detectors. 7. MC using an adaptive threshold; 8. MC using the steepest gradient histogram threshold; 9. MC using the Otsu threshold; 10. MC using the region-growing algorithm; 11-13 MC using a morphological operation (MO) with maximum N-connected pixels; 14. MC using the biggest-gap algorithm; 15-16. MC using median filter of different window lengths; 17. MC using a low-pass first-order Butterworth filter.	104
5.7	Chain 1: [209], chain 2: [72], chain 3: [200], chain 4: [123], chain 5: [106], chain 6: [235], chain 7: [196], chain 8: best work chain presented in this work, chain 9: random chain.	106
5.8	Confusion matrix for the first method.	106
5.9	Classification accuracy for the second and third methods, respectively on the left and right boxplots, with the two different classifiers model.	107
5.10	Fetal heart rate measured using the algorithm.	107
5.11	AV Conduction Time measured using the algorithm.	107
5.12	MPI measured using the algorithm.	108
5.13	E/A ratio measured using the algorithm.	108
5.14	Bland-Altman analysis regarding the fHR.	109
5.15	Bland-Altman analysis regarding the AV interval.	110
5.16	Bland-Altman analysis regarding the MPI index.	111

5.17	Bland-Altman analysis regarding the E/A ratio.	112
6.1	Single-reference adaptive filter used as adaptive noise canceller, applied to the non-invasive fECG extraction problem to remove the mECG contribution from the abdominal signals.	117
6.2	Block diagram of the multi-reference QRD-RLS adaptive filter used as adaptive noise canceller, applied to the non-invasive fECG extraction problem to remove the mECG contribution from the abdominal signals.	122
6.3	Example of SWT and SWPT 2-level decomposition of a real fECG signal. a) in the SWT decomposition, after the first step, only approximations are split. b) in the SWPT, both approximations and details are decomposed.	126
6.4	Electrodes positioning: the m channels are the bipolar maternal leads, while on the abdomen there are the unipolar ones.	132
6.5	A sample signal from the real dataset.	133
6.6	A sample recording from the real dataset.	134
6.7	Graphical representation illustrating the locations of the maternal heart (upper circle) and the fetal heart (lower circle). Squared boxes, located on the maternal abdomen, indicate electrode positions and are numbered for the corresponding output channel. The referenced electrode is labelled as GD (middle circle).	135
6.8	The first row represents the simulated signals, respectively the horizontal, vertical, oblique and unipolar channels, while the others, labelled as MC and FC, represent the associated mECG and fECG components.	136
6.9	Example of the two datasets.	137
6.10	Results on the real dataset. OR: original raw abdominal lead, SR: single-reference method, MR: multi-reference method, hor: horizontal lead, ver: vertical lead, obl: oblique lead, unip: unipolar channel.	145

-
- 6.11 Results on the synthetic dataset. OR: original raw abdominal lead, SR: single-reference method, MR: multi-reference method, hor: horizontal lead, ver: vertical lead, obl: oblique lead, unip: unipolar channel. 146
- 6.12 Accuracy of the fetal QRS detector applied on the output signals from SR and MR QRD-RSL algorithms, for real (left) and synthetic (right) datasets. 146
- 6.13 Real dataset: raw thoracic lead and raw processed abdominal leads at different zoom levels for a single subject. In detail: (i) on the first row, the thoracic horizontal maternal lead, used as reference in the SR implementation, is shown; (ii) in the second row, there are the four raw leads, so in order: horizontal, vertical, oblique lead and the unipolar channel; (iii) in the third row, the respective processed, by the SR method, signals, each one with its respective zoom, are plotted; (iv) in the last row, the processed signals by the MR technique and their zoom are displayed. 149
- 6.14 Synthetic dataset: raw thoracic lead and raw processed abdominal leads at different zoom levels for a single subject. In detail: (i) on the first row, the thoracic horizontal maternal lead, used as reference in the SR implementation, is shown; (ii) in the second row, there are the four raw leads, so in order: horizontal, vertical, oblique lead and the unipolar channel; (iii) in the third row, the respective processed, by the SR method, signals, each one with its respective zoom, are plotted; (iv) in the last row, the processed signals by the MR technique and their zoom are displayed. 150
- 6.15 SNR, Accuracy and TPR results for real data. 153
- 6.16 SNR, Accuracy, TPR, cSQI, Pearson's correlation coefficient, RMSE and Spearman's correlation coefficient results for synthetic data. 155
-

6.17 Example of SWT and SWPT denoising results with 7-level decomposition, with the three different thresholds. A: Han et al. threshold, B: Minimax and C: Universal. On the right, results obtained on a real fECG signal are reported, while on the left side results on a simulated signal are represented. Zoom on one-second of each denoised signal is reported in order to appreciate fetal peaks morphology after wavelet denoising. 156

6.18 Confusion matrix relative to the signal quality assessment of the unprocessed fetal ECG traces. 157

List of Tables

3.1	Available datasets.	34
3.2	Review of fECG intervals, as from different studies. CI stands for 95% Confidence Interval.	42
4.1	Clinical information about subjects and fetuses. Regarding the fetus, the presentation is first listed followed by the its position, in particular: L:left, R:right, O: occiput, S: sacrum, T: transverse, P: posterior A: anterior	64
4.2	Duration of the signal segments that composed the dataset. . .	66
4.3	Evaluation results of the peak detection.	66
5.1	Main works on the automated tracing of Doppler velocity envelope.	76

5.2	Best Chain Results: The MC comprises: Gaussian-shaped low-pass filter with $\sigma = 1.5$, a k-means algorithm to enhance the contrast, the Otsu 2D method, removal of small noisy clusters with 70 four-connected pixels, tracing the boundary pixels of all white regions to obtain contours, and a temporal median filter with a window size of three pixels. In the order: 1. MC using no filter application for the first preprocessing step; 2. MC using as an intensity adjustment the subtraction of the greyscale and modified images; 3. MC using no operation for the second preprocessing step; 4. MC using the Canny algorithm; 5. MC using the NLLAP edge detector (NL); 6. MC using a combination of the NLLAP and Sobel edge detectors; 7. MC using an adaptive threshold; 8. MC using the steepest gradient histogram threshold; 9. MC using the Otsu threshold; 10. MC using the region-growing algorithm; 11–13 MC removing spurious areas using a morphological operation with maximum N-connected pixels; 14. MC using the biggest-gap algorithm; 15–16. MC using median filters of different window lengths; 17. MC using a low-pass first-order Butterworth filter. The bold values indicate the best results.	105
6.1	Computed signal quality features.	130
6.2	Real and Synthetic dataset results: median values (first quartile third quartile)	147
6.3	Wilcoxon signed rank test results on the real dataset (significance threshold at $p < 0.05$, significant differences marked with *).	148
6.4	Wilcoxon signed rank test results on the synthetic dataset (significance threshold at $p < 0.05$, significant differences marked with *).	148

List of Publications

Conference Papers

[1] G. Barabino, G. Baldazzi, E. Sulas, C. Carboni, L. Raffo, and D. Pani, *Comparative evaluation of different wavelet thresholding methods for neural signal processing*, Annual International Conference of the IEEE Engineering in Medicine and Biology Society (EMBC), vol. 2017, pp. 1042-1045, July 2017.

[2] E. Sulas, M. Monticone, L. Raffo, and D. Pani, *Adaptive filtering for electromyographic signal processing in scoliosis indexes estimation*, in International Joint Conference on Biomedical Engineering Systems and Technologies (Biostec), 2018.

[3] E. Sulas, E. Ortu, L. Raffo, M. Urru, R. Tumbarello, and D. Pani, *Automatic Recognition of Complete Atrioventricular Activity in Fetal Pulsed-Wave Doppler Signals*, in 2018 40th Annual International Conference of the IEEE Engineering in Medicine and Biology Society (EMBC), pp. 917-920, 2018.

[4] E. Sulas, E. Ortu, M. Urru, A. Cadoni, R. Tumbarello, L. Raffo, and D. Pani, *Fetal Pulsed- Wave Doppler Atrioventricular Activity Detection by Envelope Extraction and Processing*, in Computing in Cardiology, vol. 45, 2018.

[5] E. Sulas, E. Ortu, M. Urru, A. Cadoni, R. Tumbarello, L. Raffo, and D. Pani, *The NlnFEA dataset for non-invasive fetal electrocardiography research*, in Computing in Cardiology Conference, Sept. 2018. (in press)

[6] E. Sulas, A. E. Martis, P. Cosseddu, A. Achilli, G. Sollai, I. T. Barbarossa, L. Raffo, A. Bonfiglio, and D. Pani, *Objective human gustatory sensitivity assessment through a portable electronic device*, in IEEE Biomedical Circuits and Systems Conference (BioCAS), pp. 1-4, 2018.

[7] E. Sulas, M. Urru, A. Cadoni, R. Tumbarello, L. Raffo, and D. Pani, *Comparison of Single and Multi-Reference QRD-RLS Adaptive Filter for Non-Invasive Fetal Electrocardiography*, in Annual International Conference of the IEEE Engineering in Medicine and Biology Society (EMBC), July 2019.

[8] G. Baldazzi¹, E. Sulas¹, E. Brungiu, M. Urru, R. Tumbarello, L. Raffo, D. Pani, *Wavelet-Based Post-Processing Methods for the Enhancement of Non-Invasive Fetal ECG*, in Computing in Cardiology Conference, Sept. 2019.

Journal papers

[9] E. Sulas, M. Urru, R. Tumbarello, L.Raffo, D.Pani, *Systematic analysis of single- and multi-reference adaptive filters for non-invasive fetal electrocardiography*, Mathematical Biosciences and Engineering, Sept. 2019.

[10] E. Sulas, M. Urru, R. Tumbarello, L.Raffo, D.Pani, *Automatic Detection of Complete Cardiac Cycles in an Antenatal Pulsed-Wave Doppler*, Computer Methods and Programs in Biomedicine (accepted)

[11] E. Sulas, M. Urru, R. Tumbarello, R. Sameni, L.Raffo, D.Pani, *Introducing the NInFEA Dataset for Non-Invasive Fetal Electrocardiography Research*, Scientific data (submitted)

[12] E. Sulas, E.Ortu, M. Urru, R. Tumbarello, L.Raffo, D.Pani, *Impact of pulsed-wave Doppler velocity envelope extraction techniques on the classification of complete foetal cardiac cycles* (ready to be submitted)

[13] G. Baldazzi², E. Sulas², G.Solinas, L.Raffo, D.Pani, *Wavelet denoising as post-processing enhancement for non-invasive fetal electrocardiography* (ready to be submitted)

[14] E. Sulas, D. Pani, R. Vullings, *Automatic signal quality assessment of raw trans-abdominal biopotential recordings for non-invasive fetal electrocardiography*(ready to be submitted)

¹Both authors contributed equally to the manuscript

²Both authors contributed equally to the manuscript

Chapter 1

Introduction

1.1 Motivation

The incidence of the Congenital Heart Disease (CHD) has been estimated at six to twelve per 1000 live births. [53] From the clinical viewpoint, cardiologists are interested in the early identification of structural [97] and electrical [223] defects occurring during the fetal development, which can be treated in uterus by trans-placental drugs administration [175] or surgery [179, 226], approval of instrumented delivery [1], or preparation for prompt after-birth surgery [53].

The introduction of the fetal electrocardiography (ECG) into clinical practice could represent a turning point in the diagnosis of the fetal heart pathologies and the possibility to treat the fetus also during the early pregnancy.

During the past decade, non-invasive fetal ECG (fECG) acquisition and signal processing technologies have evolved, but one of the main factor hampering the broad application of non-invasive fetal electrocardiography is the absence of public datasets, which enable the comparative evaluation of different techniques and multiple simultaneous modalities for researchers. The development of such reliable datasets is indeed expensive, time-consuming and difficult to obtain for many reasons. Some of the important properties of a standard fECG dataset, appropriate for algorithm development and research, include: adequate number of channels (sixteen and above), signal quality and quantization level

(sixteen *effective number of bits* and above), high sampling frequency (1 kHz and above), and alternative simultaneous modalities for cross validation and benchmarking.

My PhD project is based on a new fetal ECG open dataset development and acquisition, from the selection of the requirements to the development of the setup. It is a multi-modal dataset in terms of simultaneously acquired signals, recording multi-channel non-invasive fetal ECG, multi-leads maternal ECG, maternal respiration signal and synchronised fetal trans-abdominal pulsed-wave Doppler (PWD) recordings, enriched by clinical information and the position of the fetus. The main criteria of inclusion is the gestational age, in order to be able to perform the ultrasound recordings and the fetal ECG, without distortions due to the vernix caseosa and other interfering factors [144, 146].

This work focused also on both electrophysiological and ultrasound signal analysis that composed this dataset.

1.2 Thesis outline

Chapter 2 gives an overview of the fetal heart development, anatomy and physiology, focusing on the discussion of the electrical activity of the heart. Fetal cardiac diagnosis and monitoring tools are introduced, with particular care to the fetal electrocardiography and ultrasound technologies. Regarding the ultrasound technologies, the physical principles and the doppler technique are introduced. Moreover, the important clinical parameters that can be computed on the PWD signals, which are used in this thesis, are illustrated.

In chapter 3, the several state-of-the-art are reviewed. The fetal ECG processing involves different phase: preprocessing, processing, post-processing, and a general overview of the methods that have been applied in these contexts is given. A detailed description of the available fetal ECG open datasets is discussed, and, considering the work of this thesis, also an introduction to the methods used for the signal quality assessment in the ECG field is illustrated. PWD analysis, in terms of extraction of the PWD envelopes, is reviewed. Due to the complexity of the topic, an overview of the available literature is given, but a more detailed literature will be discussed specifically in each chapter.

Chapter 4 describes in detail the developed dataset. It illustrates the set-up, in terms of physiological acquisition instrumentation, ultrasound machine, synchronization of the two modalities, study population, electrode positioning. It gives an overview of the dataset quality in terms of fetal heart rate derived from the two modalities and by visual inspection.

Chapter 5 focuses on the pulsed-wave Doppler signal. Several works in literature investigated the extraction of the PWD velocity envelopes. This thesis focuses on the selection and comparison of the different signal processing chain steps that lead to the PWD envelopes. The envelopes are the inputs of a classifier in charge of identifying the PWD window where a meaningful and complete cardiac cycle is present. The performance assessment aimed to understand the impact of the different extraction steps in terms of classifier accuracy. Furthermore, this thesis proposes the comparison of three different algorithms for the detection of complete heartbeats. Finally, this chapter presents also a germinal work on the automatic computation of significant clinical parameters than can be measured in the PWD traces.

Chapter 6 focuses on the signal processing techniques for the fetal ECG signal. Among the different techniques proposed in the scientific literature, some variants of adaptive filters have been proposed for maternal ECG cancellation and fetal QRS complex enhancement. Such techniques encompass approaches using one or more reference signals, which is an important aspect for the development of accurate and unobtrusive monitoring systems. In this chapter, this aspect is systematically analyzed by comparing single- and multi-reference implementations of the QRD-RLS adaptive filter, and by challenging them in the fetal ECG enhancement on three abdominal leads differently oriented in space. Beyond the chosen processing technique, the studied adaptive filters seem to produce an output suffering from high levels of residual noise, deserving a post-processing to enable a study of the morphology of the fetal ECG. For this reason, different wavelet-based post-processing approaches for the denoising of the fECG were evaluated. The signals were decomposed with the stationary wavelet transform (SWT) and stationary wavelet packet transform (SWPT), using a 6- and 7-level decomposition with Haar mother wavelet and hard-thresholding, and level-independent and level-dependent thresholds were tested. Then, the enhancement of the fetal QRS complex was analyzed by com-

puting several parameters. Moreover, the chapter will discuss about a germinal work on the fetal ECG quality assessment, that is relevant considering wearable and unobtrusive monitoring systems, in order to select, prior to the application of the processing technique, the most informative fetal ECG channels.



Chapter 2

Fetal cardiac diagnosis and monitoring

The aim of this chapter is to give a brief introduction to the development, anatomy and physiology of fetus' heart. The second part will give an overview of the fetal cardiological diagnosis and monitoring techniques with particular emphasis to electrocardiography and echocardiography.

2.1 Fetal cardiocirculatory system development

The heart is one of the first organs that starts to develop in the fetus. There are several stages involved in the heart development. The heart begins to develop around the 19th day of fertilization with the appearance of endocardial tubes, in a region called the cardiogenic zone. Between the 22nd and 23rd days, due to the differentiation of cardiac cells as pacemaker cells, the first irregular heart contractions are observed. From the 5th week of gestation, the heart presents four chambers, an inflow (superior and inferior vena cava) and an efflux (aorta and pulmonary trunk) pump system, controlled by several valves [48].

During the pregnancy, the right atrium communicates with the left part through two shunts: the ostium secundum, near the roof of the left atrium, and the foramen ovale, near the floor of the right atrium. These openings allow blood from the lower vena cava, rich in oxygen, to go directly into the left atrium, then from the left ventricle into the systemic circulation, most of the blood eluding the pulmonary circulation. The ductus arteriosus, also called the

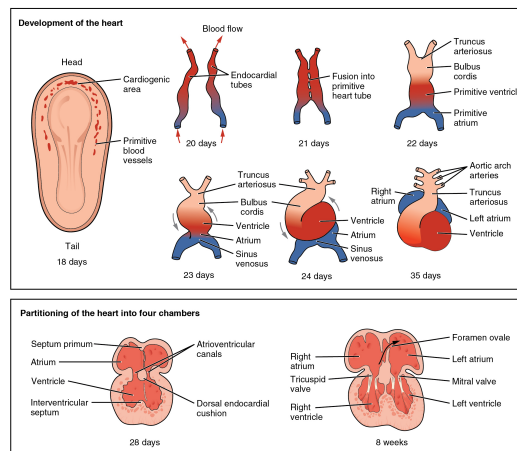


Figure 2.1: Fetus Heart Development. [93]

ductus Botalli, connects the pulmonary trunk and the descending aorta, and introduces oxygenated blood, coming mainly from the superior vena cava and the pulmonary artery, in the aorta, and most of the blood avoids the passage in the small pulmonary circulation. In fact, the pressure in the aorta is lower than the pressure in the adult, and also lower than in the pulmonary artery, this is another reason why the blood goes through the ductus arteriosus in the aorta. There is also another shunt, the ductus venosus, that connects the umbilical vein to the inferior vena cava, in order to bypass the liver. Definitive atria and ventricles develop in the second month of heart development.

The myocardium, that develops outside the heart chambers, plays a crucial role in heart development: it provides the base for the formation of the valves and the septa, and, moreover, the myocytes are intrinsically inclined to depolarize spontaneously. The myocardium development creates a dominant pacemaker activity in this region, which begins the slow propagation of the action potentials. The rapid conduction through the myocardium of the cardiac chambers is then acquired when they mature [48].

When the baby is born, the oxygen begins to be present in the lungs when he starts to breath. As a result, the baby's pulmonary vascular resistance substantially drops. The pressure in the pulmonary artery falls and that one in the aorta rises, causing the closure of the ductus arteriosus and the blood begins to flow backward. In fact, the increased systemic resistance raises the pressure in the left atrium, that becomes higher than the pressure in the right atrium, and these changes in the pressure cause the foramen ovale to close with a membrane called septum primum, within few hours to a few days in most babies. [59]

Anatomy and Physiology In the adult, the heart consists of two separate pumps: the right part of the heart that pumps blood through the lungs, and the left part that pumps blood through the peripheral organs. Each part is made of an atrium and a ventricle. The atrium pumps the blood in the ventricle, while the ventricle is the main pump that drives the blood in: (i) the pulmonary circulation by the right ventricle, (ii) the systemic circulation by the left ventricle.

The fetal heart exhibits significant differences with respect to the adult heart. In fact, the oxygen and the nutrients are provided to the fetus by the

mother via the umbilical cord, that is also responsible for the metabolic wastes and carbon dioxide removal. The oxygenated blood in the fetus goes from the umbilical vein to the inferior vena cava, bypassing the liver via the ductus venosus. Furthermore, in fetal circulation, there is greater pressure in the right atrium compared to the left atrium; therefore most of the blood is shunted from the right atrium to the left atrium through the foramen ovale, and then goes into the aorta and the systemic circulation. Because there is high resistance to blood flow in the lungs, the blood is shunted from the pulmonary artery into the aorta via the ductus arteriosus, and most of the blood bypasses the lungs. [59]

2.1.1 Pathology

The diagnosis of CHDs in early pregnancy represents an important clinical challenge. CHDs are the most common type of birth defect [112]; as recently as ten years ago, the CHD birth prevalence was approximately nine per 1,000 live births [213]. A critical problem is that excluding infections, the condition that accounts for the largest number of deaths during the first year of life is CHD [122]. Further, high levels of mortality are prevalent in children and adults because of CHD, which is also associated with lifelong comorbidity that impacts health service utilization and costs [127]. Because of the improvements in the medical and surgical treatments of CHDs, reduced morbidity and mortality following antenatal diagnosis have been reported for some critical diagnoses [188].

Pregnancies at a higher risk of fetal cardiac anomalies are those with: (1) a family or an obstetric history of CHD; (2) fetuses having an abnormal basic cardiac examination during the first trimester scan; (3) the presence of indirect markers for fetal CHD, such as increased nuchal translucency, abnormal flow in the ductus venosus, or tricuspid regurgitation; (4) fetuses with chromosomal anomalies; (5) fetuses with any other associated structural defect; (6) monozygotic twin pregnancies; and (7) pregnancies from assisted reproductive technologies. Early identification of specific cardiac anomalies, such as aortic stenosis, might allow intrauterine treatment to improve the perinatal outcome. Complete cardiac examination might be considered as part of the routine fetal anatomy scan at 11–13 + 6 weeks of gestation. [83]

Assessment of fetal heart rhythm

The assessment of abnormalities in the heart rhythm in the fetus is more challenging because the electrocardiogram cannot still be obtained in the clinical practice. [223] Alternatively, some modalities of the echocardiography can be applied for this purpose, such as the M-mode and the Doppler technologies. These modalities allow the study of the timing of the atrial and ventricular mechanical movements, that are the consequences of the electrical depolarization. [223] Even though the fetal heart rhythm can be studied, these modalities have not any information about the morphology of the electrical events, i.e. on the P-wave, QRS- and QT-interval. Despite these limitations, the ultrasound technology permits to correctly identify the arrhythmia mechanism based on characteristic echocardiographic pattern.

Irregularities in the rhythm can be due to several reasons. Most of them are associated with isolated premature atrial contractions, that are caused by the activation of the atrial cells before the normal atrial beat, and the occurrence of the ectopic beat resets the normal sinus beat. [223] There are different degrees of prematurity of the ectopic event, and on this basis, the electrical activation can be conducted to the ventricles or be blocked within the AV node, causing an extra or a missed beat. Thus, the irregular rhythm can cause:

- Bradycardia: it is conventionally defined when the heart rate is lower than 100 beats per minutes (bpm).
- Tachycardia: it is characterized by an heart rate higher than 180 bpm. Depending on the diagnosis, the tachycardia can be defined sinus tachycardia, supraventricular tachycardia or atrial flutter.

Assessment of other cardiac structures and function abnormalities

The echocardiographic examination permits to check the cardiac structures in detail. In fact, it displays the cardiovascular anatomy with high temporal resolution. Also the systolic and diastolic functions can be quantified using the

Doppler modality. Thus, pressure gradients, intracardiac pressures, valve areas, regurgitant volume, and shunt volume can be non-invasively determined. [9]

2.2 Fetal cardiac diagnosis and monitoring tools

Depending on the aim, period and speciality, different instrumental techniques could be adopted in the clinical practice [156], including ultrasonography (US) (e.g., cardiotocography (CTG) [73], pulsed-wave Doppler, continuous-wave Doppler, B-mode, and M-mode [182, 223]), phonocardiography [34, 111], fetal magnetocardiography (fMCG) [63, 94, 206], invasive fECG [170], and non-invasive fECG [25, 40, 42]. In particular:

- **Cardiotocography:** it is a US Doppler method, coupled with the recording of uterine activity through an external pressure transducer. The CTG is commonly used in the clinical routine leading to a reduction of intrapartum and precocious mortality [186]. In fact, CTG represents the most used non-invasive technique to monitor the antepartum fetal conditions. Despite the International Federation of Gynecology and Obstetrics (FIGO) guidelines [18] suggest the use of the CTG, the actual CTG analysis has demonstrated a low predictive value for the fetal danger and very poor indications about fetus/newborn illness. [133, 186] It can be also used in classification of normal and hypoxic fetuses. [222]
 - **Fetal magnetocardiography:** it is a non-invasive technique that allows the recording of the weak magnetic field variations associated to the electrical activity of the fetal heart. It is a passive and safe recording technique utilizing the extremely high sensitivity Superconducting Quantum Interference Device (SQUID) sensors. The SQUIDs amplify signals that are naturally occurring and extremely weak. [192] Because of the requirement for specialized equipment and expertise, fMCG is currently performed in only a small number of centers worldwide. [53]
-

- Phonocardiography: it contains acoustic information reflecting the contraction and relaxation of the heart, and enables the detection of fetal heart sounds and so the fetal heart activity. [44] This method allows to study the changes in beat-to-beat fetal heart rate, that are associated with the activity of the autonomic nervous system. [104]
- Ultrasonography: it is the leading technology among those adopted for fetal heart pathology diagnosis and monitoring. [223] This technology will be further introduced in this thesis.
- Electrocardiography: it includes the invasive and non-invasive techniques. Non-invasive fECG is currently used only to analyze the fetal heart rate and its variability. The invasive fECG can be used only intrapartum, when membranes are already broken.

2.3 ECG-based technologies

2.3.1 Basic principles of ECG

Electrical Activity

The basic living unit of the human body is the cell. Each organ is characterized by the presence of different type of cells, because they are able to perform specific functions. Several substances are essential to allow the cells to complete their tasks, first of all oxygen, glucose, different ions, amino acids, fatty substances, and other constituents.

The most important ions in the cell are potassium, magnesium, phosphate, sulfate, bicarbonate, and smaller quantities of sodium, chloride, and calcium. In particular, the ions are the responsible for the interrelations between the intracellular and extracellular fluids. In facts, the cells are enclosed by the cellular membrane. The cellular membrane is mostly composed of proteins and lipids: proteins, 55%; phospholipids, 25%; cholesterol, 13%; other lipids, 4%; and carbohydrates, 3%. [59]

The membrane has different ion channels, that can be open or close depending on the protein receptor that alters the permeability of the cellular membrane to ions. In particular, we are interested in the sodium and/or calcium ion channels, that cause the cellular membrane to be depolarized, and so exciting the cell. In fact, they are required for the transmission of electrochemical stimuli in nerve and muscle fibers (such as the cardiac cells). These cells have also the function of rapidly generating such electrochemical stimuli at their membranes, that are used to transmit signals along the nerve or muscle membranes. Nerve signals are transmitted by action potentials, which are indeed rapid changes in the membrane potential that spread rapidly along the nerve fiber.

At rest, the cellular membrane is characterized by a trans-membrane potential of about -90 mV. It means that the inside potential is 90 mV more negative than the potential in the extracellular fluid. Figure 2.2 shows the events occurring during and shortly after the action potential.

Initially, the conductance for potassium ions is 50 to 100 times as great as the conductance for sodium ions, caused by much greater leakage of potassium ions than sodium ions through the leak channels. The sodium channels instantaneously become activated and allow up to a 5000-fold increase in sodium conductance. At the beginning of the action potential, the sodium ions flow to

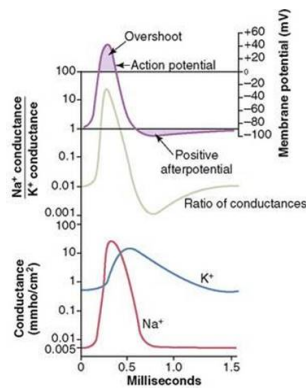


Figure 2.2: Changes in sodium and potassium conductance during the course of the action potential. [75]

the interior far more than the potassium ions to the exterior, causing the membrane potential to become positive. Then, the onset of the action potential also causes voltage gating of the potassium channels, allowing them to begin opening more slowly a fraction of a ms after the sodium channels open. The sodium channels begin to close and the potassium channels to open and, consequently, the action potential quickly returns to its baseline level. [75] Figure 2.3 shows the action potential in a ventricular muscle fiber.

Genesis of the cardiac impulse

Normally, the cardiac impulse starts in the sinus node. Also the A-V node and the Purkinje fibers are able to operate as pacemaker cells, as the sinus nodal fibers do. The difference lays in the rate. In fact, the sinus node is considerably faster than the A-V node or the Purkinje fibers, so that the sinus node controls the heart's rhythmicity.

Figure 2.4 shows the transmission of the cardiac impulse through the human heart.

The electrical impulse, generated in the sinus node, spreads slightly in the atria, but it is delayed in the A-V nodal region before arriving in the ventric-

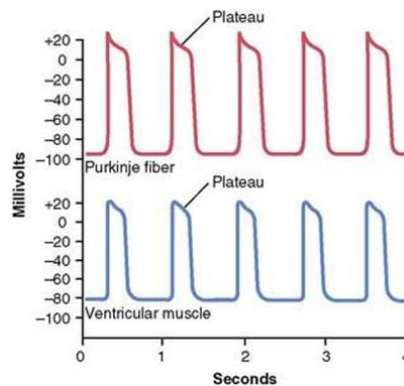


Figure 2.3: Rhythmic action potentials from a Purkinje fiber and from a ventricular muscle fiber. [75]

ular septal A-V bundle. Having reached the bundle, it goes rapidly through the Purkinje fibers and to the ventricles. Again, it spreads slightly less rapidly through the ventricular muscle. Therefore, the cardiac cycle consists of a relaxation phase, called diastole, in which the heart fills with blood, followed by contraction phase, called systole.

The ECG is based on the assumption that the electrical heart activity can be modelled by a single electrical dipole rotating around a fixed point in the chest. [66] We commonly refer to the electrical dipole as the heart (or cardiac) vector. Three assumptions are required to establish the general theory of heart-vector projection. They are [62]: (1) the human body is a heterogeneous linear resistive electrical conducting medium, (2) the distribution of currents associated with electrical activation of the heart muscle may be represented at each instant of time during the cardiac cycle by a single equivalent current dipole, whose orientation and moment are variable and function of the actual current distribution, and (3) the equivalent heart dipole remains fixed in position during the cardiac cycle.

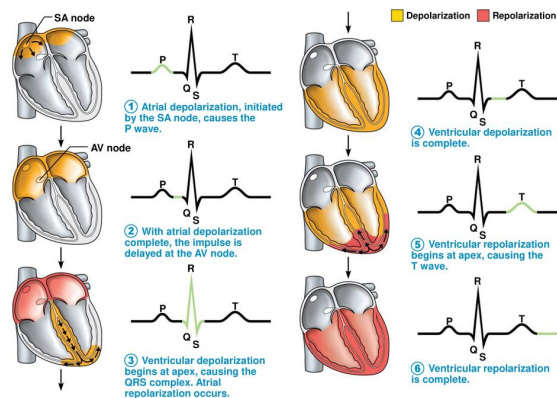


Figure 18.17

Figure 2.4: The transmission of the cardiac impulse through the human heart, leading to the known electrocardiography waveform. [75]

Figure 2.4 shows that, at each instant of the heart excitation, electrical current flows in the depolarized areas inside the heart, leading to the known electrocardiographic waveform.

Electrocardiogram morphology analysis

The ECG is a representation of the cardiac electrical signal in the time domain. The ECG is composed of the repetition of the main waves: P, Q, R, S, and T, see figure 2.4. They represent the electrical voltages generated by the heart and recorded by the electrocardiograph from electrodes on the surface of the body.

The P wave is caused by the depolarization through the atria, followed by atrial contraction. In healthy subjects, it has a width less than 0.25 mV and a duration of 60-120 ms.

About 0.16 s after the onset of the P wave, the QRS complex appears as a result of the electrical depolarization of the ventricles. Therefore, the QRS complex begins slightly before the onset of ventricular systole. The duration in a healthy subject is between 60 and 120 ms and the amplitude of the R peak can reach up to 1 mV.

Finally, the T wave represents the ventricles repolarization, so when the ventricular muscle fibers begin to relax. Therefore, the T wave occurs slightly before the end of ventricular contraction. The duration is less than 250 ms the amplitude is less than 0.3 mV.

P-R interval quantifies the time to complete the atria depolarization. Normally, it is between 120 and 200 ms. Q-T interval measures the time required for complete depolarization and repolarization of the ventricles. [75]

Morphologically, adults and fetuses have rather similar ECG patterns; however, the relative amplitudes of the fetal complexes are considerable lower and change throughout gestation. [173] The fECG can be acquired invasively, any in hospitals during labour, or non-invasively.

Invasive fetal electrocardiography

Invasive fetal electrocardiography involves the direct application of an electrode to the fetal scalp and requires adequate cervical dilation as well as rupture of the amniotic membranes. Therefore, this technique can be used only intrapartum, when membranes are already broken. [1] These techniques produce a signal of acceptable quality so they are currently adopted in the clinical practice [170]. It has well-known contraindications, mainly related to the increased risk of vertical transmission of infections. It should not be used in patients with active genital herpes infection, those who are seropositive to hepatitis B, C, D, E, or to HIV, in suspected fetal blood disorders. Fetal electrode placement should also preferably be avoided in very preterm fetuses (under 32 weeks of gestation) [18], so that this technique does not guarantee the monitoring in the prenatal period when therapeutic intervention in utero would still be possible.

Non-invasive fetal electrocardiography

Non-invasive fetal electrocardiography can be obtained at different gestational ages by means of surface electrodes applied on the maternal abdomen, with a relatively comfortable and safe procedure. Even though the availability of non-invasive fECG would help in mass screening and in the easiest identification of antenatal arrhythmias in early pregnancy, the adoption of this technique is still not widespread [223]. According to the American Heart Association, although non-invasive fECG has been available for decades (at least in research), its clinical application has been slowed for several reasons [53], including the complex setup, which requires skin abrasion and a large number of electrodes, and the relatively low signal-to-noise ratio (SNR) [53], due to different physiological factors including the maternal interference and the different layers of tissue between the fetal heart and the maternal skin [92, 144].

2.3.2 Heart Rate variability

In general, during exercise, the heart may be required to pump four to seven times the amount of oxygenated blood normally required. [75] The amount of

volume pumped by the heart is regulated by: (i) the intrinsic cardiac regulation of pumping in response to changes in volume of blood flowing into the heart, (ii) the control of heart rate by the autonomic nervous system (ANS).

The autonomic signals are transmitted through the sympathetic and the parasympathetic nervous system. In general, sympathetic stimulation increases the overall activity of the heart, while the parasympathetic stimulation causes mainly the decrease of the heart rate. As a result, the heart rate (HR) is known to contain reliable indications about the synergic activity of the autonomic nervous system, which regulates the heartbeat dynamics. [75]

Therefore, the heart rate variability (HRV) helps to monitor also the fetus development, although the exact contributions of the two branches of the ANS are still object of investigation even in adult subjects. [164]

Studies demonstrated that the fetal HR (fHR) signal could provide reliable indications on fetal status. Literature results underline that fetal distress can be appreciable in the interbeat intervals alterations. [186]

From the gynaecologist's perspective, heart rate monitoring has a paramount importance in different gestational ages [1, 88]. In early pregnancy, heart rate analysis can be used to define markers for the neurological development of the baby [87, 178], the intra-uterine growth restriction [58, 193] and general fetal well-being [52, 88]. In late pregnancy, and during delivery, heart rate analysis conveys information on the physiological reactions of the fetus to the evolving uterine conditions associated to delivery [1], including the capability to support vaginal delivery without distress, which could eventually lead to fetal brain injury [95, 113].

2.3.3 Fetal ECG-based technologies

As explain in the previous section, cardiac fetal monitoring in late pregnancy is mainly based on the analysis of the changes in the fetal heart rate [1, 185], to understand whether the fetus is responsive to different physiological stimuli or not [1, 58, 88, 185, 186].

The first fetal heart monitoring system using non-invasive fetal ECG that gained the US Food and Drug Administration (FDA) approval was the wireless fetal monitor Monica AN24 (Monica Healthcare, Nottingham, UK) in 2011.

Monica AN24, the Monica Novii Wireless Patch System (Monica Healthcare, Nottingham, UK), that also gained the FDA approval, and Nemo Fetal Monitoring System (Nemo Healthcare, Veldhoven, The Netherlands) monitor the fetal heart rate, without showing the ECG waveform, and the uterine muscle activity. The MERIDIAN M110 non-invasive fetal electrocardiograph monitor (Mind-Child Medical, Inc., North Andover, MA) non-invasively measures and displays fetal heart rate from abdominal surface electrodes that detect the fECG. It also achieved the FDA approval in 2012. More recently, Imec and BloomLife showcased a fetal ECG and mobility wearable monitoring device, featuring the first integrated circuit produced so far to this aim.

Furthermore, fetal movement counting can provide valuable information on the fetal health. A strong decrease in the number of movements can be seen as a precursor to fetal death, and it can be detected using methods based on amplitude and shape changes in the abdominally recorded fetal ECG. [165]

2.3.4 Fetal monitoring during labour

Particular attention has been given on the intrapartum monitoring [1]. Continuous monitoring during labour can involve both invasive fetal ECG and CTG recordings. CTG measures the fetal heart rate and the maternal uterine contractions.

Uterine contractions are quantified as the number of contractions in a 10 minutes window. Contractions, duration, intensity and relaxation time between contractions are important in clinical practice. [1]

The diagnosis of the fetal distress, caused by an oxygen deficiency condition, is based on the analysis of the T-wave amplitude relative to the R peak amplitude and on the presence or absence of a biphasic S-T section. [170] In fact, the T wave amplitude relative to the QRS complex width has been identified to happen when the fetus passes from an aerobic metabolism to an anaerobic one, that indicates the risk of hypoxia. An example of an invasive fetal ECG device is the STAN S31 from Neovinta Medical AB. [170] The STAN system can be used to diagnose, for example, fetal distress.

In another application [19], to monitor the fetus during the labour and to predict the preterm labour, the authors proposed a multichannel time–frequency

and multi-wavelet toolbox for uterine electromyography (EMG) processing and visualisation, which computes important uterine EMG features.

2.4 Ultrasound-based technologies

Ultrasound includes that portion of the sound spectrum having a frequency greater than 20 kHz, which is considerably above the audible range of human hearing. The use of ultrasound to study the structure and function of the heart and great vessels defines the field of echocardiography. [16]

2.4.1 Physical Principles

Ultrasound has different characteristics that make it a valuable technology to be used in diagnostic tools: ultrasound can be directed as a beam and focused, passing through a medium; the targets reflect the ultrasound that can be detected and characterized, and it obeys the laws of reflection and refraction. The disadvantages of ultrasound are that it is poorly transmitted through a gaseous medium and attenuation occurs rapidly, especially at higher frequencies. The amount of reflection, refraction, and attenuation depends on the acoustic properties of interested media, so that soft tissues and blood can be addressed by the ultrasound diagnostic tools.

The wavelength and frequency of sound wave are inversely related and their product represents the velocity of the sound wave:

$$v = f \cdot \lambda \quad (2.1)$$

where v is velocity, f is frequency (Hz), and λ is wavelength. The velocity and direction of the ultrasound beam are a function of the acoustic impedance of that medium. Acoustic impedance (Z , measured in Rayls) is simply the product of velocity (m/s) and physical density (ρ in kg/m^3).

$$Z = \rho \cdot v \quad (2.2)$$

A variation in the impedance creates an acoustic interface region. The bases for the ultrasound imaging are represented by the interaction between the

US beam and the acoustic interfaces. The use of gel between the transducer and the skin surface increases the air-tissue interface performance, in a way that more than 99% of the energy is reflected at this interface. Also the angle of incidence between the transmitted beam and the acoustic interface is important, because of the reflection and refraction physical laws.

The use of ultrasound becomes practical with the development of piezoelectric transducers. Piezoelectric crystals are able to vibrate when an alternating electric current is applied. The rapidly alternation of expansion and contraction of the crystal produces the sound waves. Then, a piezoelectric crystal will produce an electric impulse when it is deformed by reflected sound energy. [16]

There are different display options, according to the processing carried out on the output signal by the probe.

- A-mode: it is a one-dimensional representation. It has only one scan-line, so one reflected signal, and the obtained signal is showed as amplitude variation over time. The time is proportional to the tissue depth. It is rarely still used in medical diagnostics.
 - B-Mode (Brighness mode): the beams are composed of several crystals, with multiple scan-lines. It associates a specific gray level to a specific voltage. This representation allows to obtain a two-dimensional image in gray scale by converting the echoes, that arrive in each crystals, into signals whose brightness is proportional to the amplitude of the echo: the white corresponds to the maximum intensity, while the black corresponds to the absence of echoes. Multiple scans are performed by moving the probe.
 - M-Mode (Motion mode): it shows how the discontinuity position changes along one single scan-line. It provides a two-dimensional image because it associates to the reflected echoe amplitude a specific grey level. It is able to detect speed, frequency and amplitude of a movement. In fact, this type of visualization is widely used in cardiology for the study of heart chambers and valve movements.
-

2.4.2 Doppler Ultrasound

Doppler echocardiography detects the direction and the velocity of moving blood, exploiting the doppler effect, so that the probe emits a sound beam with a known frequency and detects the movement of the blood through the frequency variation perceived by the probe. [107]

In the medical equipment, the Doppler frequencies are converted into artificial audible sounds that can help the doctor to quickly understand the nature of the flow. Moreover, the Doppler frequencies are also represented as a speed spectrum, so a two-dimensional signal that represents speed of red blood cells as a function of time. The speed of the flow towards the transducer is displayed as positive on the y-axis, while the speed of the flow away from the transducer is displayed as negative. Time is represented on the abscissa. The intensity is a function of the number of red blood cells that move at that certain speed. [107]

Currently two types of Doppler echocardiography are used: the Continuous-Wave Doppler and the Pulsed-Wave Doppler. Continuous-wave (CW) Doppler involves continuous generation of ultrasound waves (one crystal) coupled with continuous ultrasound reception (another crystal). The main advantage of CW Doppler is its ability to measure high blood velocities accurately. The main disadvantage of CW Doppler is its lack of selectivity or depth discrimination. [107]

Pulsed-Wave Doppler

Pulsed-wave Doppler (PWD) uses a transducer that transmits and receives the ultrasound wave and echo. One main advantage of pulsed-wave Doppler is its ability to provide Doppler shift data selectively from a small segment along the ultrasound beam, referred to as the sample volume. The main disadvantage of PWD is its inability to accurately measure high blood flow velocities, due to the aliasing problem. [107]

The location of the sample volume is operator controlled. In fact, one of the main limitation of this technique is the intrinsic operator-dependency [188]. Moreover, also multiple settings can reduce the ultrasound artifacts and they depend on the operator choice. Improper setting, probe movements cause very

noisy recordings.

In fetal echocardiography, PWD can aid the assessment of cardiac rhythm [53, 210], particularly to make a differential diagnosis of abnormal patterns. Compared with other modalities, blood flow through the heart and great vessels, along with the movement of heart tissues, can be more objectively studied using Doppler ultrasonography by exploiting different measurements and validated reference parameters that assess the morphology of the PWD spectrum over complete and meaningful cardiac cycles [64].

PWD is commonly adopted in clinical practice for the diagnosis of CHD or functional problems during pregnancy [53]. The first clinical assessment is preferably performed between the 18th and 22nd week of gestation [53]. For the routine Doppler examination of patients with suspected valvular heart disease, it is usually best to begin by using an apical view [107], shown in figure 2.5.

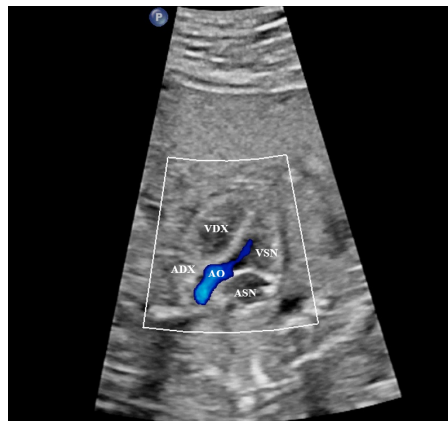


Figure 2.5: Apical 5-chamber view of the fetal heart.

In particular, an apical five-chamber view allows recognizing the four cardiac chambers and first part of the aorta. By choosing this view, it is possible to analyze the diastolic and systolic functions, producing morphologically well-defined envelopes in the PWD signal, as reported in figure 2.6 and from the sketch in figure 2.7. While the systolic phase produces a single peak in the flow velocity waveform (V), caused by blood flow through the aortic valve, the

diastolic phase results in a typical biphasic waveform [141], with an early peak (E) determined by the passive filling of the left ventricle through the mitral valve due to the differential pressure between the two chambers, and a second peak (A) during the active atrial contraction. Overall, the EA-wave represents the mitral inflow, whereas the V-wave represents the aortic outflow, and the two waves present opposite polarities. In healthy fetuses, each atrial event is followed by a ventricular event, which occurs within a well-defined time-interval in normal 1:1 atrioventricular (AV) conduction [223].

The spikes in the waveform of the recorded Doppler signal are indicators of the beginning of the opening or closure of both mitral and aortic valves. The opening and closing of the valve leaflets produce original click Doppler in the same direction as the blood flow (in the case of opening) or in the opposite direction (closure). The smaller Doppler spikes are present in the opposite direction to the originals and are called reflected clicks. The original clicks and the reflected clicks share a common peak time point. The spikes are not always present; for example, in figure 2.6, only the aortic valve closure clicks can be seen.

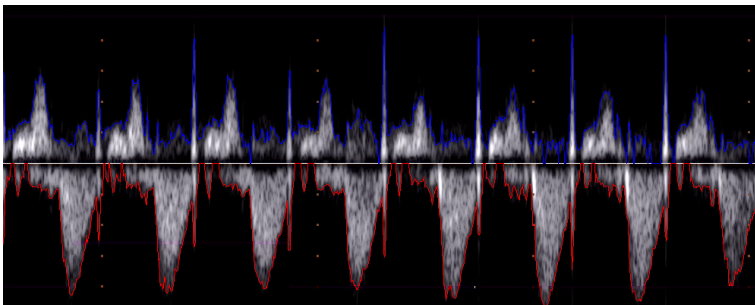


Figure 2.6: A PWD velocity image obtained using an apical 5-chamber window.

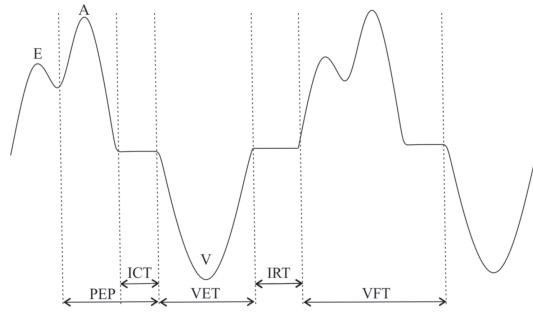


Figure 2.7: The sketch of the AV activity with identification of the main waveform components and intervals.

2.4.3 Important Parameters

The importance of the PWD signal interpretation is confirmed by the relevant number of indexes of clinical interest that can be extracted from it.

- The fHR is the simplest index: the guideline suggests a baseline value between 110 and 150–160 bpm before and during labor [157]. Considering the PWD traces acquired using an apical 5-chamber window, the heart rate can be measured as show in figure 2.8.

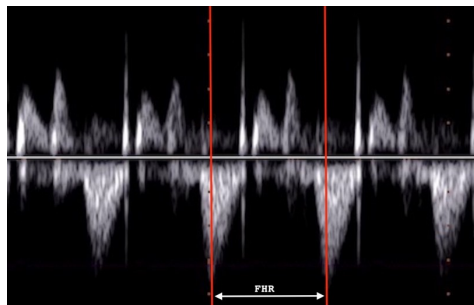


Figure 2.8: Fetal heart rate measured considering the peak of the ventricular activity.

- The E/A ratio is the index for the evaluation of the left ventricle functionality: E is smaller than A, and the E/A ratio increases during pregnancy towards one. After birth, the E/A ratio becomes greater than one [67]. During early pregnancy (8–20 weeks), anemic fetuses present a dominant E peak suggesting that in fetal anemia, there is an increased preload in the right atrium [141]. In fact, in the fetus, the aorta and the pulmonary artery have the same pressures, as the fetal circulation is characterized by having large shunts between systemic circulation and pulmonary circulation. After the birth, there is a significant change in pressure, and because of the significant difference in pressure between pulmonary and systemic circulation, most of the pulmonary arterial blood flows passively from the atrium to the left ventricle, according to pressure gradient, and only a minimal part of the refluxed blood is actively pumped by the atrium, so that, in the adult heart, it is reasonable to expect a wave E wider than the wave A. In the fetal heart instead, due to the minimal difference in pressure, it is necessary that the blood is actively pumped from atrium to ventricle, so that A wave is greater than E wave.

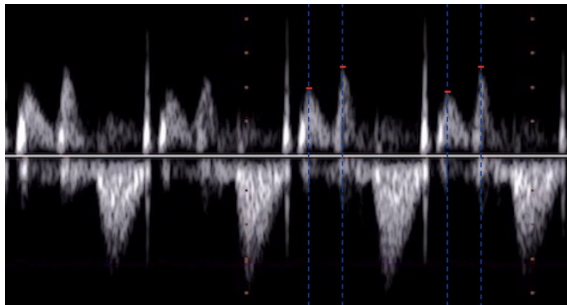


Figure 2.9: E and A peaks in the PWD trace.

- The AV interval, shown in figure 2.10, is an important index of conduction disorders that can be derived from PWD. In fact, the normal heart rate with a prolonged AV conduction time interval may progress to a complete form of the AV block. The measurement of the mechanical AV conduction time interval could aid in identifying fetuses with first-degree AV block.
-

These fetuses might benefit from transplacental steroid administration to avoid progression toward complete and irreversible AV block [142]. Several studies have shown the physiological AV values, that are also correlated to the gestational age and to the fetal heart rate. [10, 142, 208] The reasonable values can be also been predicted using the equation [208]:

$$AVConductionTime = 174.976 + (1.315WOG) - (0.612HR) \quad (2.3)$$

where WOG is the week of gestation and HR is the heart rate.

The electrical (PR interval) and mechanical (AV interval) atrioventricular intervals depend on the atrial depolarization (P wave) and ventricular depolarization (Q wave) and the respective mechanical consequences in the atrial (A) and ventricular (V) region. Despite the difference in delay between electrical and mechanical activation of the atria and ventricles, there is a good correlation between echocardiographic AV intervals and electrocardiographic PR intervals. Several studies have shown that Doppler intervals are longer than PR intervals [10, 142].

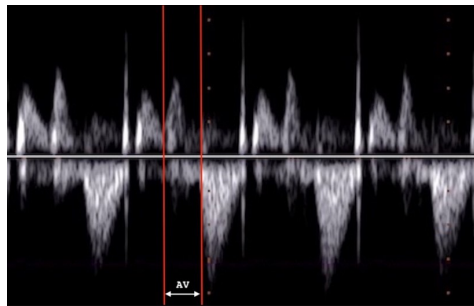


Figure 2.10: AV interval.

- The myocardial performance index (MPI) was reported by Tei [205], and then modified in 2005 with the introduction of the mod-MPI [82], as a helpful predictor of systolic and diastolic cardiac dysfunction. It is defined as the sum of the isovolumetric contraction time (ICT) and isovolumetric

relaxation time (IRT), divided by the ventricular ejection time (VET) of each ventricle (intervals shown in figure 2.11). Furthermore, these time indexes are very useful indicators of fetal wellbeing [103].

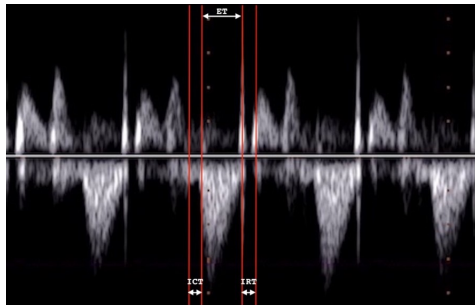


Figure 2.11: MPI index.



Chapter 3

Methods and tools for fetal ECG and Doppler analysis

This chapter is divided into two parts. The first part focused on a general overview of the the state-of-the-art techniques in the field of fECG extraction, while the second part introduces the PWD extraction and analysis methods already presented in literature.

3.1 Non-invasive fetal ECG

The first fECG was observed in 1906 [45] using galvanometers strings. The improvements in terms of measurement and amplification techniques led to a better feasibility of the fetal ECG recording. [119]

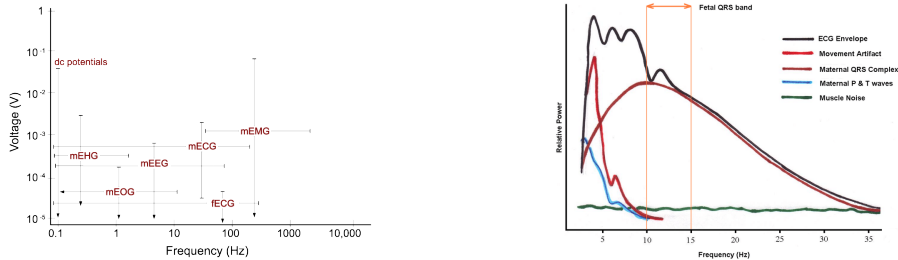
The use of the fetal ECG monitoring was improved when the use of the scalp electrode was introduced for monitoring the fetal heart rate. [71, 85, 168] Later, there was the introduction of signal processing techniques in the fetal non-invasive field, with the adoption of the adaptive filters [225] and the multichannel signal processing techniques [230]. In the last two decades, huge improvements have been introduced in this field, but not still able to extract a clean fetal ECG from abdominal recordings.

3.1.1 Fetal ECG signal processing issues

The non-invasive fECG is recorded using electrodes applied on the maternal abdomen. However, the signal-to-noise ratio (SNR) is low, due to the small size of the fetal heart, the feto-maternal compartments, the maternal physiological interferences and the instrumental noise.

The fetal heart source is characterized by the weakness of the fetal cardiac potentials. The fetus is covered by different anatomical layers that are characterized by different conductivities. The *vernix caseosa* is a layer that has considerable influence on the recordings of fetal ECG. In fact, it has electric insulating properties that can extremely attenuate or even suppress the fECG, especially during the time frame between the 28th and 34th week of gestation [144]. Insulating layers such as the vernix caseosa, also change the preferred conductive pathway of the fECG through its propagation path, resulting in potential morphological variations of the fECG [144].

The noises and interferences overlap with the fetal ECG in various domains. Figure 3.1 shows amplitude and frequency range of different biosignals, some of them represent the interferences to the fetal cardiac signals. In fact, the fetal ECG recordings are characterized by the presence of several noise sources that come also from the mother, such as the maternal ECG, the maternal respiration signal, the muscles artifacts, the uterine contractions. In particular, the fECG



(a) The amplitude and frequency range of different biosignals, some of which interfere with fetal cardiac signals. [173]

(b) A general representation of the signal, artifacts and noise present in the ECG in the frequency domain. [173]

Figure 3.1: Amplitude and frequency characteristics of biopotentials and artifacts that are present in the fetal ECG recording.

extraction from the interfering maternal ECG (mECG) is hampered by their spectral overlap. Moreover, the most common artifacts that characterize every physiological recordings need to be taken into account: device noise, power line interference, baseline wander and electrode motion.

The challenge is even more difficult considering that the fetus is always moving in the maternal abdomen, so that fetal body coordinates varies with fetal movements and rotations with respect to the maternal body coordinates (and the surface leads). This fact is the reason why a standard electrode positioning for recording the fetal ECG has not still been achieved. Remarkably, we note that the surface leads are described accordingly to the electrical axis of the maternal heart and not of the fetus heart.

Moreover, we should consider also the multiple pregnancies (twin, tripling, etc), where more than a fetal ECG source are recorded.

3.1.2 Available Datasets

A factor hampering the broad application of non-invasive fetal electrocardiography is the absence of public datasets, which would enable the comparative

evaluation of different techniques and multiple simultaneous modalities for researchers. [53, 173] At this moment, the available datasets present several weaknesses that make them unsuitable to really faster the progress in the field, mainly because of the number of recordings, number of leads, traces duration, homogeneity, multimodality and absence of a reference gold standard [173]. Table 3.1 presents the available datasets.

The first dataset in the field, Daisy [56], consists of a single 8-lead signal, 10 s long, sampled at 250 Hz.

The Non-Invasive Fetal Electrocardiogram Database [68] was also taken from a single subject but contains 55 variable-duration recordings, recorded between the 21st to 40th week of gestation. Recordings include three or four abdominal leads with variable electrode placement, sampled at 1 kHz with a 50 Hz notch analog filter and a bandwidth 0.01 Hz - 100 Hz.

The Abdominal and Direct Fetal Electrocardiogram Database (ADFECGDB) [109] contains 4-lead recordings from five women in labour, between the 38th and the 41st week of gestation, sampled at 1 kHz and 16 bit resolution, with a homogeneous placement of the electrodes around the navel. The reference invasive fECG is present as gold standard.

The most recent open dataset is composed of heterogeneous signals, prepared for the Physionet/Computing in Cardiology Challenge 2013 [187]. It is composed of one-minute recordings sampled at 1 kHz, including only four abdominal leads. For the sake of the challenge, data are non-homogeneous in terms of electrodes positioning, recording instrumentation (resolution, configuration and frequency response), and also includes synthetic signals [187].

In fact, beyond real datasets, synthetic ones are available [12], consisting of 34 channels (32 abdominal and two thoracic) at 250 Hz, representing signals from 10 simulated pregnant women. For each one, 7 different physiological events, such as fetal movement, maternal or fetal acceleration or decelerations, uterine contraction or ectopic beats, were produced, using five different SNR of the maternal ECG over noise (0, 3, 6, 9, 12) and producing five repetitions, for a total of 1750 synthetic signals.

Moreover, the FECGSYN tool [12, 21] is a reference open-source platform for non-invasive fetal electrocardiography research. In abdominal fECG recordings, surface electrodes measure the electrical potential created by cardiac sources

(i.e. maternal and fetal myocardia) and noise sources (e.g. muscle activity from movement or contractions), which propagate throughout the volume conductor. FECGSYN simulator considers all of them as point dipoles, that may be rotated and translated. These dipoles have two basic attributes: a vector, represented by three coordinates in the Cartesian coordinates system, and a location, which, together with the electrodes location, define the propagation matrix of the signals to the observation points. A projection matrix built upon the cardiac dipole model is used to project the ECG signals. The projection matrix contains information about the permittivity of the conductor (assumed constant), dipole origin and relative location between observing electrodes and source. [12] By exploiting this principle, FECGSYN is able to generate maternal-fetal ECG mixtures with realistic amplitude, morphology, beat-to-beat variability, heart rate changes and noise [21]. Movements (in terms of rotations and translations) of fetal and maternal hearts, fetal activity and uterine contractions, can also be considered by the simulator. Cardiac and noise signals are calibrated with respect to the maternal signal, choosing the SNR of the fECG relative to the mECG and the SNR of the mECG relative to noise.

Table 3.1: Available datasets.

Dataset	Description	Number of channels	Length of Recordings	Technical details
Dalsy [56]	single pregnant woman	8 channels, 5 of them abdominal and 3 thoracic	10 s	Sampling Frequency: 250 Hz
NIFECGDB [68]	55 multichannel abdominal fecg recordings from a single subject between 21 to 40 weeks of pregnancy, taken weekly.	2 thoracic signals, 3 or 4 abdominal signals (most records include 4).	Variable durations	Bandwidth: 0.01 Hz-100 Hz (synchronous sampling of all signals) Sampling rate: 1 kHz. Resolution: 16 bits. Sampling Frequency: 1000 Hz.
CinC Challenge 2013 [187]	Multiple sources using a variety of instrumentation with differing frequency response, resolution, and configuration.	4 abdominal signals	One minute	
FECGSYN [12]	10 (simulated pregnant) x 7 (cases) x 5 (SNR levels) x 5 (repetitions) = 1750 synthetic signals were produced.	channels 1-32 are the abdominal ECG channels and channels 33-34 are the maternal reference ECG channels.	5 minutes	Sampling Frequency: 250 Hz Resolution: 16 bits.
ADFECGDB [109]	5 different women in labor, between 38 and 41 weeks of gestation.	four electrodes placed around the navel, a reference electrode placed on the left leg.	5 minute length	Bandwidth: 1 Hz - 150 Hz Sampling rate: 1 kHz Resolution: 16 bits Additional digital filtering for removal of power-line interference (50 Hz) and baseline drift.
OB1DB	More than 100 data sets have been collected, consisting of fetal scalp electrograms and uterine muscular activity, accompanied by maternal clinical data and newborn clinical data.	a continuous fetal ECG signal and a simultaneously recorded UC (uterine muscular activity) signal.	typically several hours in length.	

3.1.3 Signal preprocessing

In general, physiological recordings are affected by common interferences, for instance, the power line interference of 50/60 Hz, which is unavoidable, and then, to follow, the baseline wandering. These noises should be removed before the main processing. There are different signal preprocessing techniques that could be used in order to preserve the several fECG components, both in time and frequency domain. In literature, different works investigated the suppression of the baseline wander and the power line interference.

Power-line interference is a strong noise component, being sometimes 10 times greater than the fECG signal. Levkov et al. [115] described the removal of the power-line interference using subtraction procedures, while [171] introduced a linear Kalman notch filter. In [207], several techniques are compared: Finite Impulse Response (FIR) and Infinite Impulse Response (IIR) filters, adaptive filter, and wavelet transform (WT) using different type of thresholding.

Baseline wandering could be a strong interference component. In fact, several factors contribute to its generation, from maternal breathing to fetal and cable movements, which have different reflections on different leads. To this aim, at least a simple preprocessing step is usually recommended before fECG extraction. In the adult ECG for example, if a high-pass filter is selected, the cut-off frequency should be 0.67 Hz, as it is imposed by the current guidelines [108].

The reduction of the ECG baseline wander in adult recordings has been investigated for a long time: in [212] a linear phase filter with a low cut-off frequency was used, in [134] the correction of the baseline drift was done using the interpolation of consecutive isoelectric points with third order lines, while in [150] they investigated the use of the Short Time Fourier Transform technique to estimate the low frequency drift, that was removed by time varying filtering. Also the local regression estimation [169], discrete wavelet transform (DWT) [216], DWT in combination with mean-median filter [77], and empirical mode decomposition (EMD) [27] have been utilized to this aim. The work [14] illustrated and compared the use of several techniques: high pass filter (FIR and IIR), wavelet approach, moving average techniques, Savitzky-Golay Filtering, Polynomial fitting.

Regarding specifically the fetal electrocardiography, [130] tested wavelet

transform as a tool to suppress to common types of interference, but the results deformed the desired signal, especially P and T waves. In [202] several different principles are analyzed and discussed for removing the interference of power line. They compared six methods: a new class of digital parameter varying IIR multiple-notch filters with reduced transient response, an improved version of the adaptive canceller, a new ICA algorithm, based on a fixed-point iteration scheme when finding a maximum of the nongaussianity (FastICA), a new algorithm based on EMD methods and the Hilbert Huang Transform, an adaptive filtering approach based on discrete wavelet transform and artificial neural network, and a method based on the stationary wavelet packet transform. Their performance were evaluated on simulated data, in three different scenarios, based on five quantitative performance indices, corresponding to different SNRs. The results showed that most of the algorithms have good results, but the Hilbert Huang Transform based algorithm shows the overall best performance.

3.1.4 Signal processing techniques

Despite the number of techniques developed in literature for fECG extraction, the identification of a clean and undistorted fECG signal is still an open research issue. The investigated techniques in fECG extraction from non-invasive recordings are based on very different principles, among them, the adaptive filtering techniques [22, 99, 129, 159, 161, 181, 225], wavelet transform methods [6, 7, 78, 102, 234], blind source separation techniques and their variants [31, 49, 229], singular value decomposition approach [2, 100], or adaptive neural network algorithm [29]. WT-based methods have been combined with ICA [90, 121, 220], with adaptive filtering algorithms [118, 194, 227], or with the adaptive neuro fuzzy interference system [199]. Also combined methods based on singular value decomposition and independent component analysis [65] have been explored.

Multimodal analysis has been also proposed in the fetal ECG extraction problem, using both the fetal ECG and the phonocardiogram as reference [143, 198]. Data fusion, in terms of a combination of information that come from different modalities, has not still being enough exploited and would probably be

the turning point in the fetal monitoring field.

Chapter 6 presents the detail of the signal processing techniques used in this thesis.

3.1.5 Signal post-processing

Few works focused on the post-processing of the signals generated by non-invasive fECG extraction methods. The oldest and most widely used technique is the averaging of the consecutive QRS complexes [86, 89]. In [61], the time-sequenced adaptive filter was applied to enhance the quality of multichannel fetal ECG after the maternal ECG was removed. In [4], the enhancement achievable by the application of WT to fECG signals extracted by polynomial networks was reported. In particular, to examine the effectiveness of wavelet denoising (WD) on fECG, three different scenarios were investigated: as a preprocessing tool before polynomial networks, as post-processing denoising and then both as pre- and post- processing. The research revealed a slight advantage deriving from the adoption of WD as post-processing tool, for both synthetic fECG signals (assessment based on the SNR) and real fECG (assessment performed by visual inspection).

3.1.6 Signal quality assessment

Several works in literature focused on the signal quality assessment of the ECG in adult recordings. Many works addressed the signal quality assessment in order to increase the performance of the detection of arrhythmias, then other works focused on the estimation of the HR using signal quality indices (SQI) based methods.

The work [116] estimated the HR using a method based on the data fusion between SQI and Kalman filter. In particular, it used: (1) comparison of multiple beat detection algorithms on a single lead, (2) comparison of the same beat detection algorithm on different ECG leads, (3) evaluation of the kurtosis of a segment of ECG (kSQI) and (4) calculation of the proportion of the spectral distribution of a given ECG segment found to be within a certain physiological frequency band. The authors combined these four metrics into a single index.

If the kSQI and spectral distribution metrics indicated a good quality ECG, the two beat detection based indices could be trustable and be combined as a single one. If, however, the spectral contribution metrics was low, showing that out-of-band noise was present, they took into account only the intra-lead beat detection index, because the inter-lead beat detection parameter could reach a higher value because of matched detection of artifacts. If the kurtosis was low, the authors followed the same logic. This work asserted that the SQIs played an important role in eliminating the effect of noise and artifact from HR estimation, when an appropriate signal quality threshold was selected. However, the single combined metric was undersensitive to electrode motion.

The aim of [50] was to identify when the level of noise is really high so that it can cause a wrong ECG interpretation. There, several methods for ECG quality estimation were implemented for comparative evaluation: (1) difference between the original signal and the aligned averaged signal, (2) Karhunen-Loeve transform, (3) activity or variance of the signal, (4) mobility, defined as the squared root of the ratio between the variance of the first derivative of the signal and the variance of the original signal, (5) complexity, so the ratio of the mobility of the first derivative of the signals to the mobility of the signal itself, (6) counting of the number of local minima with amplitude higher than a threshold, (7) Zero Crossing Rate, (8) T-P interval average power divided by the QRS, (9) cumulative mismatch histogram (mismatch values of consecutives QRS complex are stored as histograms for subsequent analysis generating a mismatch histogram), (10) First-Difference histogram of R-R intervals, (11) frequency content in six bandwidth (0.05–0.25, 0.25–10, 10–20, 20–48, 48–52, and 52–100 Hz) and Out of range event (counting of the number of times the signal goes above or below a threshold). Furthermore, they proposed also three novel methods: (12) the LMS adaptive filtering is used to remove the ECG signal and, therefore, the adaptive filter estimates the noise content, where the SNR is computed, (13) kurtosis of the signal, (14) temporal dispersion. In this work, the kurtosis gave the best performance.

In [20], a support vector machine was trained to classify the ECGs as clinically acceptable or not. Each channel was first downsampled to 125 Hz and, for each 10 s record, six SQIs were calculated for each lead: (1) the relative power in the QRS complex (pSQI), (2) kSQI, (3) the relative power in the baseline,

considering as baseline the frequencies lower than 1 Hz (basSQI), (4) the percentage of beats detected by two different peak detectors (bSQI), (5) the ratio of the number of beats detected by two different peak detectors, (6) the ratio of the sum of the eigenvalues associated with the five principal components over the sum of all eigenvalues obtained by principal component analysis applied to the time-aligned ECG cycles detected in the window selected for the analysis (from a length of 5 s to 10 s) by the eplimited algorithm, which segmented 100 ms either side of the R-peak (pcaSQI). For each 10 s record, the six SQIs were computed and used as the input features of the SVM classifier. The best result was obtained by using all the six indices.

In [38], they used seven quality indices, adding three other metrics to the four used in [116]: the percentage of beats detected on each lead which were detected on all leads (iSQI), the bSQI, the pSQI, the third moment (or skewness) of the distribution (sSQI), the percentage of the signal which appeared to be a flat line (fSQI), the basSQI. They compared two different classifiers, a support vector machine and a multi-layer perceptron artificial neural network. Using only one index, bSQI, kSQI and basSQI gave the best result. All combinations of pairs, triplets etc were used in order to identify which provided better results than all SQIs together. The authors found that the best result was obtained when considering four SQIs (bSQI, basSQI, kSQI and pSQI).

In [24], the authors presented an algorithm for assessing the ECG quality for false arrhythmia alarm suppression of intensive care unit monitors. Seven quality indices were used: kSQI, sSQI, basSQI, pSQI, pcaSQI, the fraction of beats and the ratio of the number of beats detected by two different peak detectors. The best result was obtained using all SQIs as classifier input.

The work [98] proposed a multimodal heart beat detection using signal quality indices. The ECG SQI was based upon the agreement between two distinct peak detectors on the ECG signal on the arterial blood pressure waveform. Detections from these two signals were merged by selecting the R peak positions from the signal with a higher SQI.

In [47], the authors found that the ability of SQIs to discriminate between ECG artefacts and arrhythmic ECG varies based on arrhythmia type, since the pathology of each arrhythmic ECG waveform is different. They used several parameters based on the detected RR interval, already presented in [147]. The

average template matching correlation coefficient consistently differentiated 'ECG artefacts' from 'arrhythmic ECG' for asystole, bradycardia and tachycardia alarms. This SQI used a normal beat template and compared it to each individual detected beat. [147]. Measures of baseline wander well distinguished bradycardia from artefacts but not asystole. For tachycardia alarms, two of the highest discriminating SQIs were the maximum RR interval for 10 s and mean heart rate for 10 s.

In [117], thirteen signal quality indices were extracted from the ECG waveform by expanding earlier works and published papers: bSQI, sSQI, kSQI, pSQI, basSQI, bsSQI (baseline wander check in time domain), eSQI (the relative energy in the QRS complex), hfSQI (the relative amplitude of high frequency noise), purSQI (signal purity of ECG), rsdSQI (the relative standard deviation (std) of QRS complex), entSQI (the sample entropy of the ECG waveform), hfMSQI (high frequency mask of ECG waveform), pcaSQI. Classification accuracy was used to evaluate the performance of the algorithm, together with the acceptable single class overlap accuracy. The performance of the individual SQIs was determined using the training and test datasets of the simulated data, and hfSQI got the best result. The best SQIs combination was obtained by selecting 10 SQIs: hfSQI, kSQI, pcsSQI, sSQI, basSQI, bsSQI, entSQI, pSQI, purSQI and hfMSQI.

The presented works introduced several SQIs for the assessment of the ECG quality and the studies mostly evaluate the indices significance through the obtained classification result. In [176], a recent and complete review of the different SQIs can be found. They presented several SQIs based on the ECG signal and/or noise features and the machine learning classifiers and/or heuristic decision rules. This work spotlighted practical limitations of the existing SQIs, for example, as the QRS feature-based SQI methods request a reliable QRS complex detector, which is still a challenging task even under ambulatory recording environments for adult ECGs.

For fetal ECG quality assessment, the study [11] aimed at characterizing extracted non-invasive fECG signals by using signal quality measures. It was based on previous works [13] and explored the signal quality estimation and multichannel information fusion. It divided the SQIs into four domains:

- Time:
 1. stdSQL: standard deviation of the signal
 2. sSQL: third moment, or skewness, of the signal
 3. kSQL: fourth moment, or kurtosis, of the signal
 - Frequency
 1. pSQL: relative power of the fetal QRS complex
 2. basSQL: relative power of the baseline
 - Detection-based
 1. bSQL: percentage of beats commonly detected by two different QRS detectors.
 2. iSQL: percentage of beats detected on current lead that were detected on all other leads.
 3. rSQL: regularity measure of the fetal QRS interval.
 4. cSQL: conformity measure, and it is the average value for the correlation coefficient between each beat and the fECG template.
 5. xSQL: the extravagance measure represents the contrast between the detected fQRS complexes and the embedded noise, so that it is calculated comparing the fECG peak against the power of the signal within three times a chosen window length (around 25 ms).
 - fECG-specific
 1. mxSQL: is the analogous of xSQL with focus on the amplitude of the maternal QRS peaks.
 2. mpSQL: is the magnitude-squared spectrum for the residuals and the median reference maternal HR.
 3. mcSQL: spectral coherence that assesses the similarity between the MCG chest-lead and extracted fECG on the [0, 100] Hz band.
-

Table 3.2: Review of fECG intervals, as from different studies.
CI stands for 95% Confidence Interval.

Study (ms)	#subject	QT	CI	QRS	CI	PR	CI
[3]	21						
[203]	199	251	289-304	47	61-65	102	110-114
[35]	374	228.4	219-239	49.4	45-54	105.6	99-118
[204]	15	225	62	92.5			
[79]	48						
[17]	13	96	132.8				
Yilmaz et al. (2015)	64	235.5	54	47-57	97.5	91-105	
[219]	117						

4. $miSQI$: is based on the $iSQI$, and it is $miSQI = 1 - iSQI$.

The classification aimed at generating a combined signal quality estimation based on the several SQI features available. For the purpose of classification, a Naive Bayes classifier was employed. The authors also evaluated the individual features according to their class separation capabilities. Time and frequency metrics showed little importance, which could be explained by the well-known similarities and spectral overlap between abdominal ECG/mECG/fECG, detection-based algorithms were relevant, while the fECG-specific features showed modest importance.

3.1.7 Fetal ECG cardiac time intervals

By considering the non-invasive fECG still an evolving research field, there is only limited evidence of normative cardiac time intervals. The systematic review [190], published in 2018, divided the groups according to the week of gestation. Several studies [3, 17, 79, 203, 204, 219] were analyzed. The table 3.2 shows the extracted intervals achieved in those works, only for the weeks of gestation that are of interest for this thesis (between the 21st to the 27th week of gestation).

3.2 Fetal Ultrasound

In 1954, a cardiologist and a physicist were the first researchers to perform the time-motion or M-mode recording of heart movements using an ultrasound device called reflectoscope. [57] For fetal applications, in 1964 Wang was the first [136] to report M-mode echocardiography of the fetal heart. [228] The innovation involved again the fetal cardiac application with the introduction of the Doppler sonography. Continuous-wave spectral Doppler had been available for many years, but, as it was already said in the previous chapter, it does not allow to select the source of the Doppler signal, and this limitation was overcome by the pulsed-wave Doppler, which allowed selecting the space-source for the Doppler analysis. In [135], they used the Doppler echocardiography for assessing human fetal intracardiac flow. In a systematic review of five studies, Randall et al [160] reported that fetal echocardiography correctly detected CHD in 85% of unselected population and 35%–86% of low-risk population.

3.2.1 Doppler signal processing

As already explained in section 2.4.2, pulsed-wave Doppler can aid the assessment of cardiac rhythm [53, 210], particularly to make a differential diagnosis of abnormal patterns, also by exploiting different measurements and validated reference parameters that assess the morphology of the PWD spectrum over complete and meaningful cardiac cycles [64].

In order to enable the automatic computation of the aforementioned parameters from the PWD waveform, section 2.4.3, complete and clinically meaningful cardiac cycles must be first recognized. This process is usually performed by the operator via visual inspection. However, the automatic identification of completely measurable cardiac cycles in the PWD could be introduced in the echocardiographs as a first step for the automated measurements of the main parameters that can be computed from this signal.

Furthermore, this detection shall be reasonably automatized for long traces or the offline analysis of PWD datasets. This is the case of a multimodal dataset, when the PWD is used as reference signals for the analysis, as it is for the dataset presented in this thesis.

In this context, the automatic detection of the meaningful cardiac cycle would represent an invaluable tool for the assessment of the quality of the trace and analysis of long traces, both for studying and computing several important indexes and parameters on the recording and to produce a gold standard reference for benchmarking fetal ECG extraction methods.

To the best of our knowledge, only the works have been presented during the work for this thesis [195, 196], and that will be illustrated in chapter 5, are the first ones addressing the automatical identification of uncorrupted, complete, and measurable cardiac cycles in antenatal PWD signals.

3.2.2 Extraction of the PWD doppler

Several methods have been presented thus far for the extraction of the PWD envelope. The aforementioned methods require the manual selection of the cardiac cycles for additional information. For instance, most require an electrocardiogram because they are ECG gated. Typically, in these works, the results are presented by comparing either the manual and automatic tracing of the envelopes or the parameters extracted from them (or simply by visual inspection).

The first studies addressing the automatic tracing of Doppler envelopes were based on the edge detection techniques [36, 72, 106, 123, 183, 184, 200, 209, 235]. Some of this works will be discussed in detail in chapter 5.

Further, learning-based and probabilistic-framework algorithms for the automatic detection and segmentation of the Doppler traces were reported. In [152], an algorithm for automatically tracing the envelope of mitral valve inflow Doppler spectra was presented. The algorithm was built on the techniques used in the probabilistic hierarchical and discriminant framework [233]. In this case, a single triangular object represented an isolated *E*- or *A*-wave, whereas a double triangle represented a pair of overlapping *E* and *A* waves. A single triangle model comprised three points: a left root, a right root and a peak. A double triangle model had five points: a left root, a right root, a left peak, a right peak, and an intersection point. Three detectors were trained: left root detector, right root detector, and peak detector. Additionally, two global box detectors were trained: a single triangle detector and a double triangle detector. Each candidate was associated with a posterior detection probabil-

ity. For each shape candidate, either specified or inferred, the shape profile model was invoked to score it with a posterior probability. Based on these two probabilities, the algorithm selected the best candidates from the single and double triangle candidate pools. To quantify the performance of the algorithm, four measurements were computed: *E*-wave peak velocity, *E*-wave deceleration time, *A*-wave peak velocity, and *A*-wave duration. These values were compared with the measurements individually computed using annotations made by two experts.

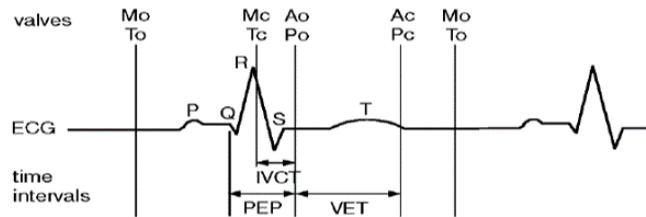
Some related works focused on model-based image segmentation algorithms. In fact, knowing the expected shape can improve velocity envelope tracing. In [221], a novel model-based feedback and adaptive-weighting tracing algorithm using the Kalman filter was proposed. The algorithm incorporated a non-parametric statistical comparison of image intensities to estimate edges in noisy PWD signals, as well as a statistical shape model learnt in an offline process using manually-traced envelopes. The results were compared with the manual tracing.

3.3 Studies relating fetal ECG and Doppler

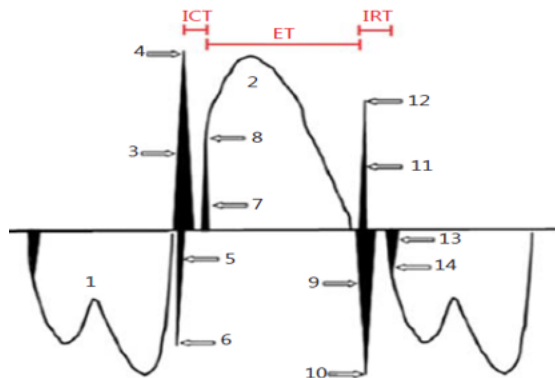
Most of the studies presented in literature focus on the recognition of the timings of fetal cardiac events on the basis of analysis of fetal ECG and Doppler ultrasound signals. In [105], a multiresolution wavelet analysis enables the frequency contents of the Doppler signals to be linked to the opening (o) and closing (c) of the heart valves (Aortic (A) and Mitral (M)). In normal fetuses, the time intervals from Q-wave of QRS complex of fECG to opening and closing of aortic valve, i.e., Q-Ao and Q-Ac are found to be 79.3 ± 17.4 ms and 224.7 ± 13.3 ms, respectively. For the mitral valve, Q-Mc and Q-Mo are found to be 27.7 ± 9.4 ms and 294.6 ± 21.3 ms, respectively. In the study [132], they assess the fetal physiological development using cardiac valve intervals estimated automatically from one-dimensional Doppler Ultrasound and non-invasive fECG. In the work [137], the assessment of the pre-ejection period in the fetus, using simultaneous magnetocardiography and echocardiography, is performed.

Considering the studies [124, 182], and looking at figure 3.2, we can identify

the valves timings on the Doppler envelopes (figure 3.2a) while, from figure 3.2b, the timings of the opening and closing of the heart valves can be seen in relation to the ECG.



(a) Diagram showing the timings of the opening and closing of the heart's valves in relation to the electrocardiogram. Mitral (M), tricuspid (T), aortic (A) and pulmonic (P); opening (o), closing (c); isovolumic contraction time (ICVT), pre-ejection period (PEP) and volumetric ejection time (VET) [182]



(b) Schematic representation of valve clicks and time intervals for the Doppler waveform waveforms. [124]

Figure 3.2: Functional timings in fetal ECG and PWD envelopes.

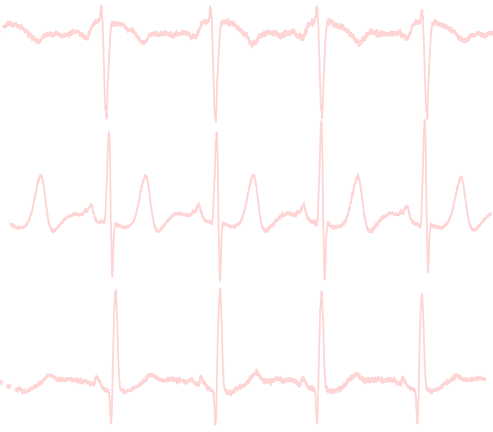
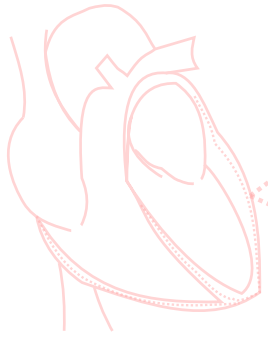
3.4 Conclusion

During the past decades, the signal acquisition and processing technologies have evolved, and several algorithms have been proposed so far, but the fECG is still not used into clinical practice.

In this chapter, the physiological aspects and the signal characteristics that make the fECG difficult to be acquired and extracted have been explained. The state-of-the-art dedicated to the fECG extraction, including preprocessing, processing and postprocessing, was briefly discussed. The need for open datasets, to be adopted as benchmark and development tools, was also stressed.

In light of all those aspects limiting the fECG tools development and clinical adoption, this PhD thesis aims to provide hitherto unavailable signals and tools. In particular, this thesis proposes a unique dataset that can be appropriate for algorithm development and clinical research, by providing multimodal recordings of the fetal and maternal hearts activity.

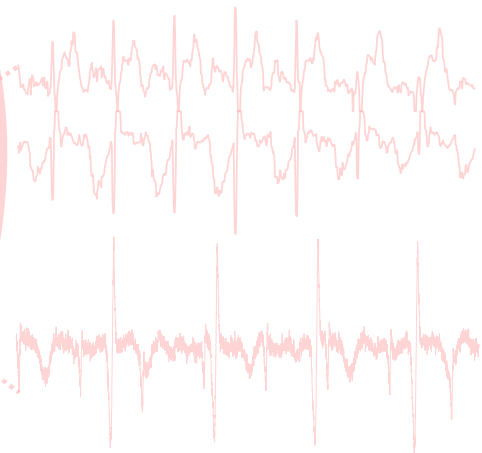
The multimodality can be a turning point in the fetal monitoring field. For this reason, the dataset presented in this thesis includes electrophysiological signals and the fetal heart PWD signal. In order to improve the combined use of the two techniques, new methods for the Doppler envelope extraction and analysis will be presented. Moreover, this PhD work will also present processing techniques that can be exploited for unobtrusive (e.g., wearable) monitoring systems.



Chapter 4

Development of a novel multimodal dataset

The objective of this chapter is to present the developed multimodal dataset and to discuss its potentialities for advancements in the field. Remarkably, as part of a continuous research project, the dataset will be further enlarged in the future, in order to provide more recordings using the same homogeneous setup.



4.1 Rationale

As it was underlined several times, the non-invasive fECG acquisition and signal processing technologies have evolved, but one factor hampering the broad application of non-invasive fetal electrocardiography is the absence of public datasets, which could enable the comparative evaluation of different techniques and multiple simultaneous modalities for researchers. The development of such reliable datasets is indeed expensive, time-consuming and difficult to obtain for many reasons. Some of the important properties of a standard fECG dataset, appropriate for algorithm development and research include: adequate number of channels (sixteen and above), signal quality and quantization level (sixteen *effective number of bits* and above), high sampling frequency (1 kHz and above), and alternative simultaneous modalities for cross validation and benchmarking.

To the best of our knowledge, the dataset developed during my PhD project is the first one of its kind. It features multi-channel electrophysiological recordings characterised by high sampling frequency and digital resolution, maternal respiration signal, synchronised fetal trans-abdominal pulsed-wave Doppler recordings and clinical annotations provided by expert clinicians at the time of the signal collection.

4.2 Acquisition protocol

The study was approved by the Independent Ethical Committee of the Cagliari University Hospital (AOU Cagliari) and performed following the principles outlined in the 1975 Helsinki Declaration, as revised in 2000. All volunteers provided their signed informed consent to the protocol. During the collection of the dataset, all the information relevant to the pregnancy were recorded; specifically, the maternal weight and height, the number of previous pregnancies, the associated risk factors, the gestational diabetes condition and in case of its presence, the prescribed/undergoing treatment. The initial position of the fetus was also annotated by an expert practitioner.

Before each recording session, the cardiologist performed the medical examination as per the guideline, and screened the morphology and the functionality

of the fetal heart. After the confirmation of a healthy status for the fetus, the ethical approval was signed by the subject and the acquisition setup was arranged. Prior to electrode attachment, a mild skin treatment was performed on the maternal abdomen using NuPrep (by Weaver and Company, USA), an abrasive gel enhancing the conductivity by reducing the skin contact impedance.

Recordings were performed with the subject at rest, in a comfortable semi-sitting position on bed. After the electrodes were attached, the respiration belt was connected around the subject's chest, and all the cables were connected to the Porti7 acquisition system. Once the set up was ready, the cardiologist checked the position of the fetus, which is included in the metadata of the dataset. Then, the simultaneously recording started, in which the cardiologist was asked to record a good quality PWD trace using an apical 5 chamber window. This obligation was time taking and required significant expertise in pediatric echocardiography. In fact, the duration of a good PWD trace depends on the fetal movements, since such movements usually lead to a PWD sample volume, requiring probe re-positioning and the repetition of PWD acquisition.

4.3 Study Population

From a cardiological perspective, ultrasound screenings are typically scheduled from 18th to 22th weeks of gestation [53], due to the possibility of in-uterus pharmacological treatment during this period. Below 18 weeks of gestation, a fetal echocardiogram may be possible, but due to the small size of the fetal heart, the image resolution is typically low. For this reason, all pregnancies screened before 15th to 16th weeks of gestation are repeated during the mid-trimester [53].

The inclusion criteria for selecting the subjects were: healthy fetus (from the cardiological perspective) and week of gestation between the 21st and the 27th. The former criterion was set to guarantee a dataset without pathological anomalies that would be poorly represented due to the reduced sample size. The latter criterion was set to obtain signals with acceptable quality in all modalities. In fact, the *volume conductor* (maternal body organs, layers of tissues and fat, etc. between the fetus and the maternal body surface electrodes) attenu-

ates the propagation of the fetal ECG signal towards the maternal abdominal electrodes [144, 146]. Among all, the layer with the lowest conductivity is the *vernix caseosa* a protective waxy substance that covers the fetus and acts as an electromagnetic insulator. It starts to develop around the 28th week of gestation and (commonly) begins to disappear from the 32nd week of gestation. The biological dissolving process may cause punctures on the vernix caseosa, which again gives the possibility to record the fECG noninvasively. However, the conduction paths that were uniform before the 28th week of gestation, could become non-uniform after the 32nd week and the fECG is distorted for morphological analysis [146].

4.4 PWD signal acquisition

From a technical viewpoint, the Philips iE33 Ultrasound Machine (Philips Healthcare, The Netherlands) was used to perform the PWD. The native resolution of the video was 1680×1050 pixels, at a frame rate of 60 Hz; the sweep speed was set to 75 mm/s. The PWD signal was recorded through the DVI output with a USB3HDCAP USB3.0 Video Capture Device (StarTech, UK). This frame grabber was able to record 1080p HD videos with a frame rate up to 60 frames per second and H.264 encoding.

The PWD shows the blood flow velocities, the direction of the flow, the timing of the cardiac events and the intensity of the flow. The PWD also has the ability of representing the blood-flow information from a particular location in the heart or in the great vessels. For the recording of the PWD signal, the 5-chamber apical window was adopted [107] (see figure 2.5), which allows flow monitoring across the mitral and aortic valves. In particular, an apical five-chamber view allows for recognizing the four cardiac chambers (in figure 2.5 VDX, ADX, VSN, ASN) and first part of the aorta (in figure 2.5 AO). This window is characterised by a specific PWD pattern, typical of the atrial and the ventricular function, as already explained in section 2.4.2.

4.4.1 PWD processing

The iE33 updates the PWD signal on the screen from left to right, and once the updated signal reaches the rightmost end of the visualisation window, the new samples replace the old one from left to right. Based on this knowledge, the whole video was converted into a single wide image by means of a Matlab custom tool by (i) decomposition of the video into single frames, (ii) crop of the images to isolate the region of interest which only contains the PWD signal, (iii) identification of the useful non-redundant frames as those where the update front of the PWD wraps to the leftmost side of the image, (iv) append of these frames to create the single wide image containing all the Doppler velocity spectrum of the processed video.

The whole images representing the PWD signals are provided with this dataset. Due to the variable position of the fetus in the womb, the mitral blood inflow can be direct towards the ultrasound transducer or moving away from it. Therefore, the $EA-V$ can have a positive balance (positive EA wave, negative V wave) or a negative balance (negative EA wave, positive V wave).

Even though the dataset is composed of the single wide images, the users of the dataset could take advantage from the envelope of the PWD signal extracted from the image. The envelope extraction leads to two signals, the upper envelope and the lower envelope. The envelope extraction involved the following three steps, detailed in [196]:

1. *Image binarization*: based on 2D Otsu's method, we adopted a global threshold from a gray-level-median histogram [180].
2. *Area opening*: removal of four-connected components with a small area (70 pixels). In addition to the noise, this step removed also the dotted line characterizing the vertical grid of the iE33 video.
3. *Edge detection*: extraction of the two 1D envelopes, representing the upper and lower profile of the PWD image, which were traced by considering the boundary pixels of the white regions.

4.5 Fetal ECG and maternal respiration signal acquisition

The fECG can be ten to twenty times smaller than the maternal ECG and wider in bandwidth: 0.05 Hz to 250 Hz (due to the QRS duration shortening caused by the higher heart rate) [134]. In order to fulfil these requirements, previous research have proposed minimum sampling frequencies between 1 kHz to 2 kHz and an analogue-to-digital quantization resolution of 16 bits [173]. For this dataset, the bio-potentials were recorded with the Porti7 portable physiological measurement system (TMSi, The Netherlands). It records simultaneous the available input channels with a sampling frequency of 2048 Hz, but with an input bandwidth limited by a digital decimation filter to approximately 550 Hz ($0.27\times$ sampling frequency). No high-pass filtering is present (DC coupling), and the digitisation at 22 bits provides a 71.526 nV resolution. Active cables shielding and high input impedance, equal to $10^{12}\Omega$, reduce the needs of hard skin preparation and protect from the power-line interference. The adopted device has 32 channels: 24 unipolar (all the unipolar channel are acquired with respect to their average), four bipolar (for differential recordings) and four auxiliary (used for sensors requiring polarisation).

Since now, there was no agreement on a standard electrode placement for non-invasive fECG. A recent review [126] reports twenty abdominal electrode configurations, four of them using 32 or more electrodes, the others less than 16. In order to ensure the maximum versatility of the dataset, and considering that no standard electrode positioning is universally accepted, a redundant number of surface electrodes was adopted. In particular, 32 electrodes were applied, as shown in figure 4.1a and 4.1b, so that it is possible to reproduce, by spatial sub-sampling, the most important placements in [126] characterised by maximum 32 electrodes, as shown in figure 4.5. In fact, figure 4.5 shows how, by selecting only a subset of electrodes recorded in this dataset, I could reproduce several placements from that review and also simulate the adoption of differential measurements. Moreover, a redundant number of electrodes also guarantees to record good-quality signals from a large number of channels, even when the ultrasound probe placement introduces artefacts in the electrodes in

close proximity.

The chosen electrode configuration includes:

- twenty two electrodes connected to unipolar channels, covering a large area of the maternal abdomen, avoiding iliac crest and rib regions (electrode number 1-22, see figure 4.1a),
- two further unipolar channels on the maternal back (electrode number 23-24, see figure 4.1a),
- three bipolar channels (to record the maternal components of the ECG), positioned on the thorax in order to capture three non-coplanar maternal leads (electrode number 25-27, see figure 4.1a),
- a signal ground electrode, positioned on the right maternal hip.

The thoracic leads enable the evaluation of fECG extraction algorithms requiring maternal reference signals, as for the adaptive filters. [161, 224, 225] Considering the large number of abdominal channels, small electrodes have been chosen: the BlueSensor N electrodes (Ambu, Denmark) have been developed for neonates, have a highly conductive liquid gel that reduces the skin-electrode contact impedance, the offset connector helps reducing the cable movement artefacts.

Moreover, a piezo-resistive respiration belt is placed around the maternal chest and it is connected to one of the auxiliary inputs of the Porti7. The application of the respiration belt enables different signal processing on the electrophysiological signals, e.g. removal of the baseline drift caused by the thoracic wall movements during inspiration and expiration. Moreover, it can support more physiological studies.

Fetal ECG extraction

The sample codes and functions for performing the described hereafter fECG extraction scheme are online available in the *open-source electrophysiological toolbox* (OSET) [172].

The raw multi-channel signals are first preprocessed by a band-pass filter with a pass-band between 0.05 Hz and 250 Hz. The maternal R-peaks are next detected from one of the reference thoracic channels. These peaks are used in a so-called deflation algorithm, based on *periodic component analysis* to remove the maternal ECG components [174]. The resultant multi-channel signals are given to a blind-source separation algorithm, known as *joint approximate diagonalization of eigenmatrices* (JADE), using the `jadeR.m` Matlab implementation by J. F. Cardoso [32], for extracting the fECG components. Since JADE does not guarantee the order of the fECG in the extracted channels, an automatic channel ranking algorithm developed in [92] were used for the automatic ranking of the fetal components. The ranking results were confirmed by an expert, subject-by-subject.

The R-peaks of the fetus were next detected from the fECG channel, by using a matched filter with predefined templates [92].

4.6 Multimodal synchronisation

The Porti7 device and the iE33 ultrasound machine cannot be directly synchronised for the acquisition of long traces. For this reason, offline synchronisation was performed on the signals recorded from the Porti7 and the frame-grabber by exploiting an external trigger signal. This trigger was a low-voltage monophasic positive square wave at 100 mHz and with a duty cycle of 10%, sent to

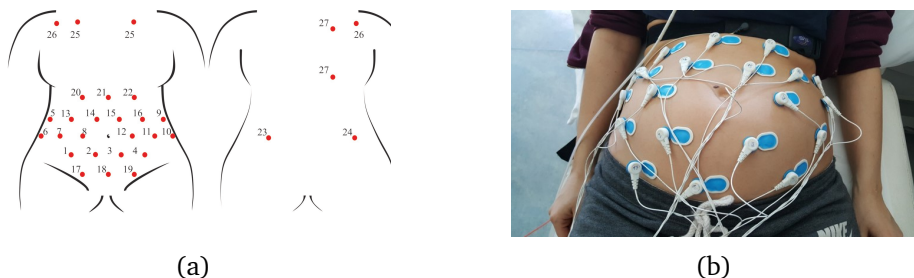


Figure 4.1: Chosen dataset electrode positioning.

the Porti7 through a dedicated isolated digital input, and to the Philips iE33 through its AUX channel. It had two different amplitudes for the two devices: 4 V for the Porti7 and 100 mV for the iE33. The trigger was recorded on the Porti7 as a digital signal, synchronised with the other inputs, whereas it was sampled as an analog signal by the iE33, producing a green trace on the lowest part of the screen, normally reserved to the electrophysiological input when the ECG leads of the ultrasound device are connected to the subject.

The synchronisation of the two traces was accomplished in post-processing by means of a custom Matlab interface, shown in figure 4.2. The custom interface presented to the user the PWD video frames with the embedded trigger signal. The user can select how to synchronise the recordings on the first rising or falling edge of the trigger. Then, the user can scroll the video frames in order to identify the exact frame where the trigger started to rise, or to fall, then marking the frame number. Finally, PWD video and the electrophysiological and respiration signals are cut in order to represent exactly the same epochs of the signals in the two modalities.

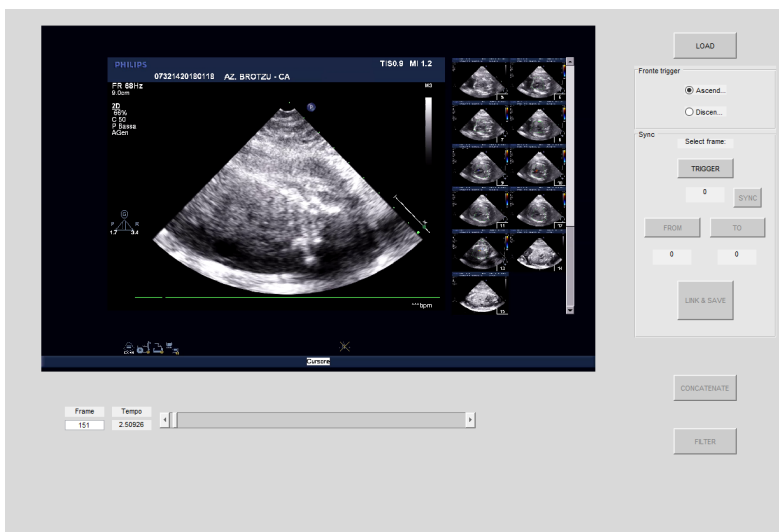


Figure 4.2: Matlab interface for synchronisation of the two traces.

4.7 Dataset quality assessment

In order to assess the quality of the presented dataset, we choose to analyse some important aspects that could help the interested researcher in the selection and use of our data. In particular, the following aspects of the dataset were analysed:

1. R-peak detection performance from the fECG, by using as reference the V peaks that were annotated by visual inspection from the PWD signals. Performance was assessed in terms of Accuracy (Acc), Sensitivity (or true positive rate, TPR) and Precision (P^+), computed as:

$$Acc = \frac{TP}{TP + FP + FN} \quad (4.1)$$

$$TPR = \frac{TP}{TP + FN} \quad (4.2)$$

$$P^+ = \frac{TP}{TP + FP} \quad (4.3)$$

where TP is the number of true positive detections, FP is the number of false positive detections and FN is the number of false negative detections.

2. fetal heart rate obtained from the fECG as compared with the fHR obtained from the PWD.
3. Visual comparison between different fECG and PWD morphologies.

The first two quality indexes are both related to the fHR, which is the most commonly used parameter in fetal health evaluation. As it was explained in section 2.3.2, fHR monitoring has an important role from different medical perspectives, such as gynaecologic and neurologic. In fact, the fHR signal provides information on fetal well-being during labour. Several conditions, such

as hypoxia, acidemia and drug induction if the labour, affect the fHR variations, both in the time and in the frequency domain. [186]

In order to estimate the fHR from the PWD traces, the V peaks were labelled by visual inspection whereas, on the fECG signal, the R peaks from the OSET toolbox was considered [172]. Agreement between the simultaneous measurements of fHR was assessed by computing the correlation analysis and the Bland-Altman [8] plots.

By exploiting the methods described in section 4.5, it was not possible to easily extract the fECGs from the 15% of the segments. In the segments in which it was possible to clearly observe the fetal QRS complexes, the agreement between the simultaneous measurements was evaluated.

Table 4.3 listed the R-peak detection results for each trace. The median Accuracy, Sensitivity and Precision values are approximately 0.79, 0.97 and 0.81 respectively, considering also the channels where the extraction of the fecg had not reached a good output. In those traces, the range of the Accuracy decreased below 0.50. A more advanced technique should be applied for the extraction of the fecg in those recordings.

The Bland-Altman plots, depicted in figure 4.3a and 4.3b, confirm the agreement between the mean HR calculated on the two different modalities, i.e. PWD and fECG. The $r^2 = 0.89$ reveals a high correlation, but the explanation could be seen in figure 4.3c. Figure 4.3c shows three different tacograms (HR time series), belonging to three different fetuses, along with the correlation study results between the points of the two traces. The two methods share always the same range of HRs, and also the variations in the HR during the acquisition are reproduced by both the techniques. Considering the leftmost plot in figure 4.3c, r^2 is 0.80, but on the rightmost plot we can observe how $r^2 = 0.50$, a quite low value, even though the two HR signals follow the same pattern. This is probably due to the steps that lead to the PWD envelopes extraction, that caused a high variability and poor precision in the identification of repeatable V-peak. To solve this variability in the Doppler tacograms, a median filter could be applied on the HR time series, resulting also in a higher agreement of the two modalities. However, in this study, the raw tacograms have been used for this analysis.

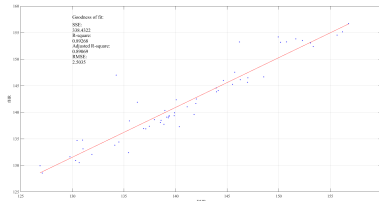
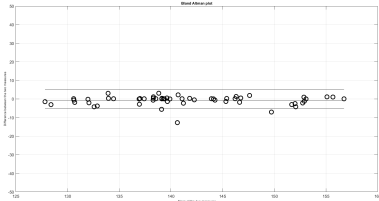
For a visual comparison between the different modalities, we can consider

signals in figure 4.4. Considering the physiological behaviour of the heart, and visually comparing figure 3.2, we can see the relation between the electrical and the mechanical activity. In fact, figure 3.2 shows a sketch of the relative timings of the heart valves in relation to the ECG and in the PWD. If we compare figure 3.2 and 4.4, the same pattern can be observed.

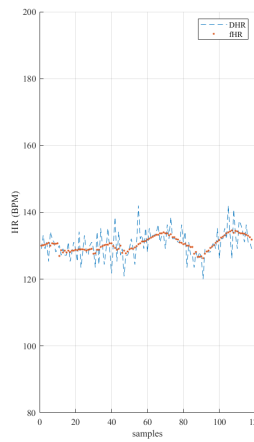
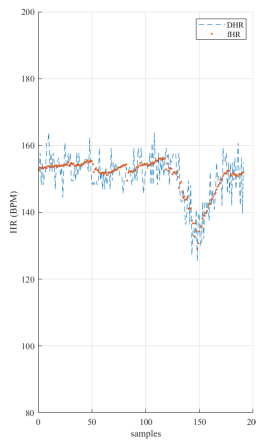
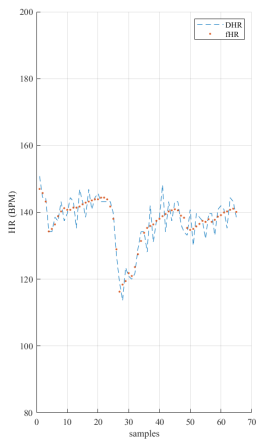
4.8 Conclusion

The released dataset is unique in terms of features. Developed by bioengineers and paediatric cardiologists, it includes multimodal sensing (electrophysiological leads from the maternal torso, respiration and fetal PWD), redundant leads to enable testing multiple signal processing techniques for fECG extraction, possibility to study the relationship between fetal PWD and fECG, roughly defining time intervals for the annotation of the fECG main events, thus providing a ground truth hitherto unavailable in early pregnancy.

As can be seen, the dataset provides unique features that can be effectively exploited by researchers working in the field of antenatal cardiological assessment. The complete dataset will be made very soon available on Physionet.



(a) Bland Altman plot of the relationship of the difference between mean fetal heart rate from ECG and from PWD signals. (b) Correlation between mean fetal heart rate from ECG and from PWD signals.



(c) Example of fetal heart rate from fetal ECG and PWD data. The graph show the signals from three subjects.

Figure 4.3: Results for the comparison between the fetal HRs obtained from the fECG and from the PWD.

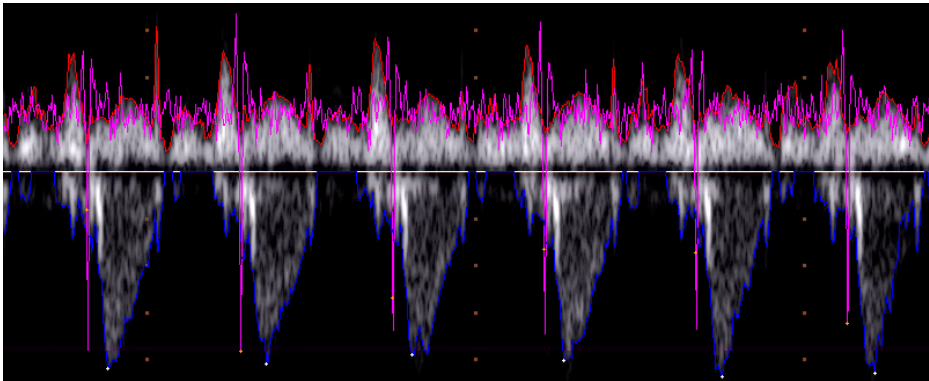


Figure 4.4: Example of synchronized fetal ECG and PWD signals.



Figure 4.5: Comparison of the dataset electrode positioning and state-of-the-art electrode positioning.

Table 4.1: Clinical information about subjects and fetuses. Regarding the fetus, the presentation is first listed followed by the its position, in particular: L:left, R:right, O: occiput, S: sacrum, T: transverse, P: posterior A: anterior

Subject	Week	Age	Height [m]	Weight [kg]	# previous pregnancies	High-Risk Pregnancies	Gestational diabetes	Preeclampsia	Risk Factors	Fetus Presentation and Position
1-3	27	27	1.7	60	0	No	no	no		vertex, OT
4-5	25	34	1.6	60	1	No	no	no	daughter with pulmonary hypertension related to surfactant deficiency disorder	vertex, ROT
6-7	21+1	30	1.5	53	0	yes	no	no	mother affected by congenital heart disease	vertex, ROT
8	22+4	32	1.65	57	0	yes	no	no	fibrosis	vertex, LOT
9	24	38	1.7	66	1	No	no	no		vertex, LOT
10-11	24+4	35	1.6	68	2	no	no	no		breech, LST
12	25+4	38	1.5	71	1	yes	yes, insulin-treated	no		breech, LSA
13-14	21+5	29	1.6	64	0	no	no	no		breech, RSP
15-16	25+2	34	1.58	67	1	no	no	no		vertex, ROP
17	24	41	1.55	63	2	no	no	no		vertex, ROP
18	26+6	37	1.7	83	2	yes	no	no		breech, RST
19	22+4	36	1.6	73	3	yes	no	gestational hypertension		breech, LSP
20-21	26+2	30	1.51	71.5	0	no	no	no		breech, LST
22	25+1	28	1.51	61.8	0	no	no	no		vertex, LOP
23	24+1	33	1.6	69	0	no	no	no		breech, RSP
24	26+6	32	1.6	78	0	yes	hyperinsulinemic	no		breech, LSP
25	26+3	36	1.75	69	0	no	no	no		vertex, LOP
26	24+1	38	1.6	63	1	no	no	no		vertex, LOP
27	27+1	42	1.48	45	0	yes	yes, treated	no		vertex, LOP
28-29	26+6	39	1.6	69	0	no	no	no		vertex, ROP
30	22+3	31	1.6	60	1	no	no	no		breech, LSP
31-33	27+5	31	1.56	65	0	no	no	no		vertex, ROP

34	25	39	1,6	63	3 abortions	yes	yes	no	breech, RSP
35-36	27	37	1,63	64	1	no	no	no	vertex, ROP
37-38	25+1	24	1,73	85	1 abortion	yes	no	no	vertex, LOP
39	24	20	1,68	91	0	no	no	no	vertex, OA
40-41	21+3	43	1,61	62	yes	no	no	no	breech, RSP
42	24+6	31	1,5	60	0	no	no	no	breech, LSP
43-44	23+4	29	1,57	63	0	no	no	no	vertex, ROP
45	23	37	1,53	60	2 + 1 abortion	no	no	no	vertex, OP
46	24+4	39	1,64	55	1	no	no	no	breech, LSP
47-48	21+1	34	1,59	47	1	yes	no	no	vertex, LP
49-50	22	29	1,65	77	1	yes	no	no	breech, LSP
51-52	24+2	36	1,53	49	1	no	no	no	vertex, LOP
53-54	21	40	1,55	54	1 abortion	yes	no	no	vertex, LOP
55-56	25	25	1,65	60	0	no	no	no	breech, LSP
57	23+6	30	1,55	70	0	no	no	no	vertex, OA
58	23	26	1,7	52	2 abortions	yes	no	no	vertex, ROP
59-60	27+3	31	1,68	63	1	no	no	no	vertex, LOP

Table 4.2: Duration of the signal segments that composed the dataset.

signals from the same subject	number of signal segments	duration of one trace [s]	duration of one trace [s]	duration of one trace [s]
1-3	3	28.07	28.64	53.06
4-5	2	44.33	47.31	
6-7	2	43.43	52.60	
8	1	13.02		
9	1	12.58		
10-11	2	37.24	17.43	
12	1	7.50		
13-14	2	23.92	45.60	
15-16	2	58.74	14.73	
17	1	31.11		
18	1	25.88		
19	1	28.87		
20-21	2	46.90	46.44	
22	1	14.32		
23	1	29.31		
24	1	64.37		
25	1	119.78		
26	1	76.04		
27	1	41.69		
28-29	2	15.39	13.22	
30	1	57.21		
31-33	3	13.88	20.88	28.10
34	1	15.46		
35-36	2	12.68	11.88	
37-38	2	25.43	10.10	
39	1	15.86		
40-41	2	12.51	25.09	
42	1	10.97		
43-44	2	50.15	34.66	
45	1	22.15		
46	1	54.80		
47-48	2	11.78	15.39	
49-50	2	9.07	46.74	
51-52	2	24.32	12.90	
53-54	2	11.44	12.25	
55-56	2	13.75	42.46	
57	1	12.88		
58	1	59.57		
59-60	2	23.99	32.93	

Table 4.3: Evaluation results of the peak detection.

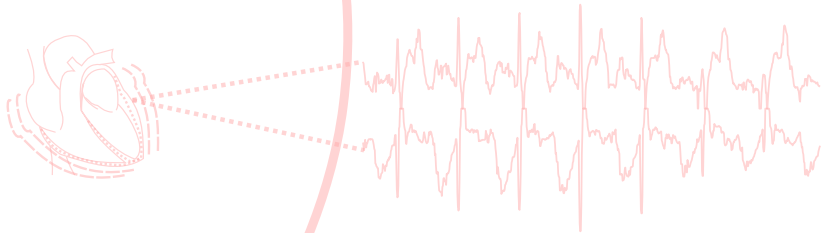
segment	Accuracy	Sensitivity	P+
1	0.90	0.97	0.93
2	0.96	0.97	0.99
3	0.72	0.99	0.73
4	0.86	0.99	0.87
5	0.84	0.98	0.86
6	0.93	0.99	0.94
7	0.23	0.93	0.23
8	0.75	0.93	0.79

9	0.82	0.94	0.86
10	0.43	0.97	0.44
11	0.33	0.88	0.35
12	0.95	0.95	1.00
13	0.90	0.97	0.93
14	0.88	0.99	0.89
15	0.23	0.97	0.23
16	0.82	0.97	0.85
17	0.75	0.97	0.77
18	0.88	0.98	0.90
19	0.97	0.97	1.00
20	0.95	0.99	0.96
21	0.26	0.97	0.26
22	0.89	0.94	0.94
23	0.80	0.98	0.81
24	0.87	0.98	0.88
25	0.63	0.99	0.64
26	0.51	0.99	0.52
27	0.33	0.97	0.33
28	0.78	0.94	0.83
29	0.79	0.96	0.81
30	0.20	0.97	0.20
31	0.66	0.91	0.70
32	0.85	0.98	0.87
33	0.46	1.00	0.46
34	0.71	0.97	0.73
35	0.74	0.96	0.77
36	0.97	0.97	1.00
37	0.37	0.92	0.38
38	0.93	0.96	0.96
39	0.68	0.93	0.72
40	0.97	0.97	1.00
41	0.38	0.92	0.40
42	0.88	0.92	0.96
43	0.64	0.99	0.65
44	0.54	0.96	0.55
45	0.84	0.98	0.86
46	0.21	0.93	0.21
47	0.68	0.95	0.70
48	0.53	0.95	0.54
49	0.19	0.80	0.20
50	0.50	0.96	0.51
51	0.46	0.97	0.47
52	0.80	0.93	0.85
53	0.86	0.96	0.89
54	0.81	0.93	0.86
55	0.84	0.96	0.87
56	0.71	0.97	0.73
57	0.82	0.97	0.85
58	0.97	0.99	0.98
59	0.63	0.97	0.64
60	0.89	0.99	0.90

Chapter 5

PWD processing and classification

Exploiting the multimodal dataset presented in chapter 4, this chapter focuses on three aspects related to PWD processing and automated analysis: (i) the several steps used to achieve the PWD envelopes, (ii) the automatic identification of complete and clinically acceptable fetal heartbeats in the PWD traces, (iii) the automatic computation of several parameters in the PWD envelopes.



5.1 Study population

For all the studies presented in this chapter, the same dataset was adopted. It consists of 43 PWD signals, collected from 25 low-risk voluntary pregnant women between the 21st and 27th weeks of gestation. The duration of the recordings was variable, from 6.4 s to 119.8 s. The recordings were performed following the same acquisition protocol described in chapter 4.

The acquired video was initially converted into a single wide image, as explained in section 4.4.

Based on the time information and image resolution, the envelopes presented 284 Hz, which can be assumed to be the sampling rate for the 1-D envelopes.

5.2 Rationale

Several works in literature investigated the extraction of the PWD velocity envelope. One of the study exposed in this chapter focuses on the selection and comparison of the different signal processing steps that lead to the PWD envelopes, which will be used as inputs for the complete heartbeats detection. The performance assessment aimed to understand the impact of the different steps in terms of classifier accuracy.

To the best of our knowledge, there are no published works addressing the automatic detection of complete and measurable cardiac cycles from PWD, neither for adults nor for fetuses. Conversely, as said before, several works deal with the automatic tracing of the PWD envelope, which is a preliminary step required by the algorithms implemented for this second study. One of the aspect investigated in this chapter is to propose and compare three different algorithms for the automatic detection of complete and measurable cardiac cycles, based on the preliminary extraction of the PWD velocity spectrum envelopes: template matching, supervised classification over a reduced set of relevant waveshape features, and supervised classification over the whole waveshape potentially representing a cardiac cycle.

Moreover, in section 2.4.3, a brief introduction of clinical relevant parame-

ters was presented. Hereafter, a preliminar work on the computation of several indices for the evaluation of fetal development and well-being is described.

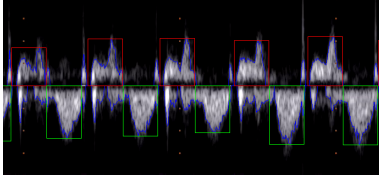
5.3 Dataset labelling

PWD automatic classification For the assessment of the algorithms discussed through this chapter, 174,319 signal windows had been labelled by using a custom graphical user interface developed using MATLAB. The interface allowed the cardiologist for scrolling over the trace to label multiple cardiac cycles. In order to represent the window under examination to the clinician, the interface showed the PWD image with two rectangular canvas, one enclosing the atrial activity (red box, 64 sample long, in figure 5.1a) and one the ventricular activity (blue box, 64 sample long, in figure 5.1a). The window size was 128 samples, as it is explained in section 5.5.2. If the two boxes overall contained a well-recorded cardiac cycle in terms of both atrial and ventricular activities, thus useful for computing clinical inspection and parameters, the cardiologist could label the selected window as “complete and measurable”, otherwise she could keep scrolling over the trace.

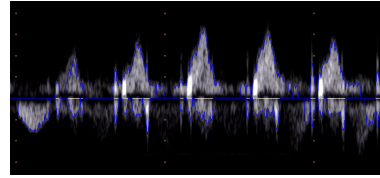
Figure 5.1 shows some examples of cardiac cycles labelled as “complete and measurable”, figure 5.1a, and a segment of PWD signal where no one was labelled in that way, figure 5.1b. As can be seen from figure 5.1a, complete cycles are neither noise-free nor perfect from a morphological perspective, conversely being affected by artifacts but still meaningful for diagnostic purposes.

Moreover, for each window labelled as complete and measurable, the tool also applied the same label to those preceding and following it, up to 15 samples. Similarly, incomplete or unreadable beats were taken on the remainder of the traces. Overall, 87,736 signal windows represented complete and measurable cycles, and 86,583 windows represented incomplete or malformed fetal cardiac cycles. Such an approach led to a balanced dataset.

Parameters and indexes from Doppler Ultrasound Furthermore, to evaluate the algorithms for the computation of the parameters on the PWD trace, another custom graphical interface has been developed to enable the



(a) Cardiac cycles labelled as “complete and measurable”.



(b) Segment of a PWD trace where no cardiac cycle was labelled as “complete and measurable”.

Figure 5.1: Labelling examples.

cardiologists to annotate the parameters, inserting specific markers for each index, shown in figure 5.2. The manual annotations were carried out by an expert cardiologist. Being a preliminary work, for each index, only 4 intervals were annotated per 40 images, so, overall, we have 40 annotations per index.

5.4 Background

Over the past few decades, several methods have been implemented for approximating the velocity envelope from Doppler ultrasound flow videos. The first studies focusing on the automatic tracing of Doppler envelopes were based on edge-detection techniques [196], [209], [72], [200], [123], [106], [235].

Table 5.1 lists the main processing steps adopted in these studies. In the first work [209], Tschirren et al. introduced the automated analysis of a general Doppler ultrasound velocity flow and presented a method comprising the following steps: (i) image filtering, using a Gaussian-shaped low-pass filter with a $\sigma = 1.5$ to remove high-frequency noise, and detection of the horizontal axis, (ii) edge detection by a non-linear Laplace edge detector (NNLAP), (iii) suppression of spurious edges and (iv) extraction of the overall envelope function using the biggest-gap algorithm. The authors compared the envelope extraction results with manual tracings and their concordance was determined using Bland–Altman analysis.

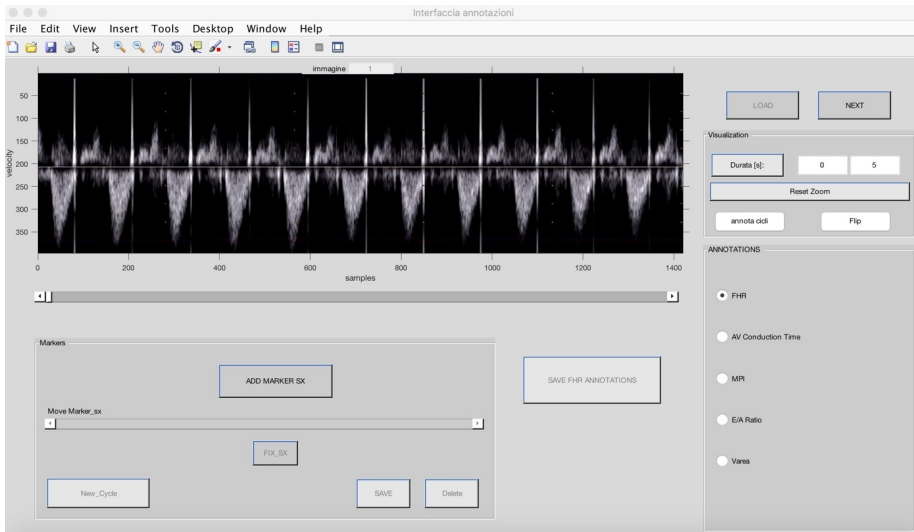


Figure 5.2: Matlab interface to annotate the PWD images and envelopes.

In [72], Greenspan et al. studied patients with atrial fibrillation. Using the same process described in [209], they focused more on contrast enhancement. In fact, just after the application of the Gaussian kernel to the images to remove background noise, they focused on the stretching of the contrast of the relevant signal. They used a k-means algorithm to cluster the pixel intensities of the image into three main clusters, representing the weak-signal, strong-signal and background pixels. The centres of these three clusters were adopted to find two optimal thresholds, which were used on the image to enhance important signal information. Moreover, after extraction of the envelope, the authors used a parametric model fitting for each cardiac cycle, based on the sum of cosines. To annotate the Doppler traces, the recordings also included the ECG signal. The results were evaluated by comparing the automatic procedure and the manual tracing, once again using Bland–Altman analysis.

Later, [200] focused on the shape-based similarity retrieval of Doppler images for clinical decision support. They binarised the images based on an Otsu threshold, followed by a dilation step and, then, the extraction of the envelope,

which was traced by considering the boundary pixels of the white regions. A temporal median filter of three taps was then applied to smooth the envelope.

In [123], Magagnin et al. adopted 2D Doppler echocardiography for non-invasive automated assessment of the severity of aortic regurgitation. These authors employed a local adaptive threshold to binarise images, and filtered the envelope with a median filter with 15 taps. Then, they interpolated the envelope using a cubic spline to achieve a sampling frequency of 1 kHz. This method also relied on an ECG gating to identify the required fiducial points. The results were then compared with manual tracings by Bland–Altman analysis.

In [106], the main aim of Kiruthika et al. was again the automated assessment of aortic regurgitation using 2D Doppler echocardiography. The applied algorithm was decomposed into the following steps: (i) application of a 5×5 Gaussian kernel with $\sigma = 1.5$, (ii) conversion to greyscale image of the filtered image, (iii) morphological operation on the image by disk approximation, (iv) subtraction of the images obtained in the first and second steps to adjust the intensity and (v) Canny edge detection ($\sigma = 0.5$). These results were also compared with the manual tracing of the envelope.

In [235], Zolgharni et al. analysed 30-s adult Doppler traces acquired by exploiting an apical five-chamber window positioned in the left ventricular outflow tract. First, they identified the Doppler region of interest and converted it from RGB to greyscale format. To filter out small noisy clusters, they removed connected areas that had fewer than a predefined number of pixels (empirically chosen as 500 pixels). The maximum velocity profile was then extracted from the resulting filtered image using the biggest-gap method. To filter out high-frequency noise, the authors applied a low-pass first-order Butterworth digital filter to the initial velocity profile. ECG data were collected simultaneously from a subgroup of patients with heart rates of 60–96 bpm. Since this study analysed Doppler envelopes in the left ventricular outflow tract, based on the typical monophasic cardiac cycle pattern, they considered each cardiac cycle to have two base points, one at the start and the other at the end of the curve, as well as a peak. Peak points on the smoothed velocity profile were identified by imposing the constraint that the distance between two consecutive peaks should be not smaller than 80% of the duration of the cardiac cycle. To detect the location of the pattern base points, they computed the first derivative of

the velocity curve. Lastly, to obtain the final automated traces, they fitted a third-order Gaussian model to each cardiac cycle of the velocity profile.

In [195], and then in a subsequent development of the original technique in [196], Sulas et al. focused on automatic recognition of the meaningful fetal cardiac cycle in Doppler ultrasound videos, acquired using an apical five-chamber window and characterised by two envelopes: one for the diastolic phase and the other for the systolic phase. The idea behind these methods is to reduce the complexity of the classification by using the upper and lower PWD velocity spectral envelopes, rather than the PWD image. Towards this end, the authors fed an artificial neural network (ANN) with 264 input features, 128 samples for each of the two envelopes, upper and lower, four area features (the area under the curve of the first 64 samples of the two envelopes, and the area under the remaining 64 samples of both envelopes), and another four features based on the pixels brightness.

5.5 Materials and Methods

This section is divided in three different parts, one for each of the aspects investigated in this chapter.

5.5.1 PWD envelope extraction chain

In order to evaluate the impact of the different steps of the envelope extraction processing, the workflow can be divided into phases: (i) image preprocessing, (ii) image binarisation, (iii) image post-processing, (iv) envelope extraction and (v) envelope post-processing. Focusing on the state-of-the-art in the field, and considering the different steps used in previous works (table 5.1), we were able to identify six different steps, because of the presence of a double image preprocessing phase. Figure 5.3 shows the complete workflow considering the different processing options presented in the literature.

To enable the evaluation of the role played by each step, we produced a prototypical processing chain (highlighted in grey in figure 5.3), which we labelled the main work chain (MC). The MC comprises a Gaussian-shaped low-

Table 5.1: Main works on the automated tracing of Doppler velocity envelope.

	Image pre-processing 1	Image pre-processing 2	Image binarization	Image post-processing	Envelope extraction	Envelope post processing
Tschirren et al. [209]	Gaussian-shaped low-pass filter with $\sigma = 1.5$		modified non-linear Laplace edge detector	Region-growing algorithm	Biggest-gap algorithm	5-point averaging filter
Greenspan et al. [72]	Gaussian-shaped 5×5 low-pass filter with a $\sigma = 1.5$	k-means algorithm to enhance the contrast	Combination of modified non-linear Laplace and Sobel edge detectors	Removal of spurious areas	Biggest-gap algorithm	
Syeda-Mahmood et al. [200]			Otsu Threshold	Removal of spurious areas with < 50 connected pixels' + Dilation step	Trace the boundary pixels of all white regions to get contours	Median filter with 3 taps, cut-off frequency ≈ 70 Hz
Magagnin et al. [123]			Local adaptive threshold		Envelope extraction	Median filter with 15 taps
Kiruthika et al. [106]	Gaussian kernel of 5×5 with a $\sigma = 1.5$	Intensity adjustment by images subtraction	Canny Algorithm ($\sigma = 0.5$)		Peak velocity extraction	
Zolgharni et al. [235]			Steepest gradient histogram threshold	Removal of small noisy clusters with < 500 connected pixels	Biggest-gap algorithm	low-pass first-order Butterworth.
Sulas et al. [195]			Otsu 2D method	Removal of small noisy clusters with < 70 4-connected pixels	Trace the boundary pixels of all white regions to get contours	

pass filter with $\sigma = 1.5$, a k-means algorithm to enhance the contrast, the Otsu 2D method, removal of small noisy clusters with 70 4-connected pixels, traces of the boundary pixels of all white regions to obtain contours, and a temporal median filter.

The impact of every possible choice on this prototypical chain was assessed. Starting from the first processing step to the last, we evaluated the various choices available for each step, while leaving the rest of the processing chain unchanged.

To identified the best work chain, once we had selected the best solution for

a single step, we modified the processing chain to include it in the assessment of the next steps.

Finally, we compared the different state-of-the-art chains (listed and described in table 5.1), the best work chain and a randomly built work chain.

The evaluations were based on the accuracy of the chosen classifier results. In the next sections, we briefly illustrate the options available for each of the processing steps in the overall PWD velocity-envelope extraction. Then, we describe our performance assessment methodology and the results.

Image preprocessing

Image preprocessing is performed to remove noise and emphasises the aspects of interest in the image. From our analysis of the scientific literature, we found that this phase can also involve two steps, as described in the following sections.

Image filter Image filtering techniques are traditionally associated with image enhancement. A low-pass filter is usually adopted to remove high-frequency noise while preserving the frequency components at the lower end of the spectrum, [69]. A Gaussian low-pass filter is a smoothing filter, which produces a particular Gaussian shape of the blurred kernel with the radius related to the standard deviation σ of the distribution. In [209], [72], [106], the authors used a Gaussian low-pass filter with $\sigma = 1.5$, which had been determined empirically, based on a trade-off between noise suppression and blurring of the image data. Some algorithms for Doppler tracing include no low-pass filtering at the beginning of the processing chain.

Contrast enhancing In [72], the authors achieved both background noise removal and stretch of the signal contrast by exploiting two thresholds, whose values were chosen based on the range in which the signal needed to be enhanced. These two thresholds were defined using a k-means algorithm that clustered pixels by their intensity into three different classes, i.e. background pixels (class 1), weak-signal pixels (class 2) and strong-signal pixels (class 3). Using the values of the cluster centres, low and high thresholds were identified. The Th_{low} value was determined as the point where the histogram value

drops by $\frac{1}{\sqrt{2}}$ of its value at the class-1-cluster centroid μ_1 . The other threshold, Th_{high} , was similarly selected using the value of the class-3-cluster centroid μ_3 .

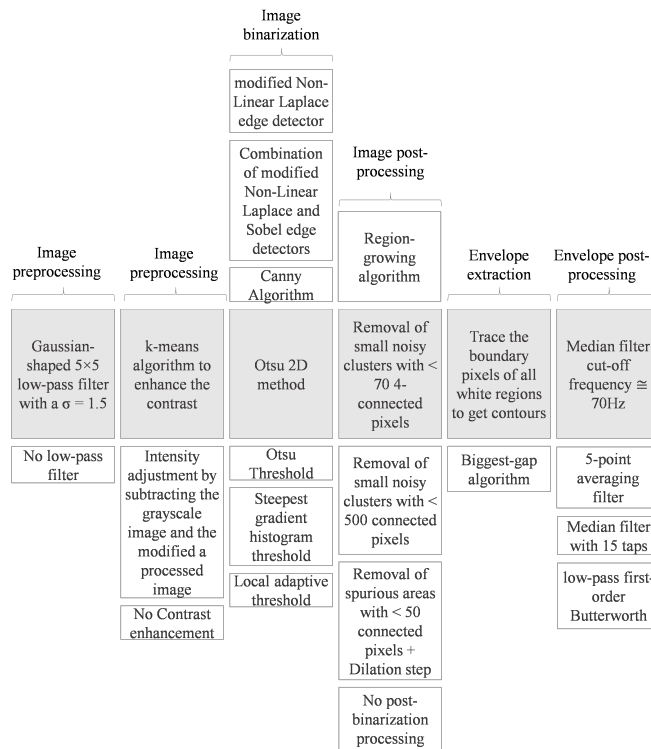


Figure 5.3: Column-wise, the different processing steps in the workflow for the extraction of the Doppler velocity envelope. The shaded boxes in the central row indicate the chosen prototypical processing chain, and the unshaded boxes indicate the available options evaluated in this study.

Using both thresholds, contrast stretching was implemented as follows:

$$g(s) = \begin{cases} 0 & s < Th_{low} \\ \frac{1}{Th_{high}-Th_{low}} s - \frac{Th_{low}}{Th_{high}-Th_{low}} & Th_{low} \leq s \leq Th_{high} \\ 1 & s > Th_{high} \end{cases} \quad (5.1)$$

where s is the pixel brightness.

Intensity adjustment An image must have sufficient brightness and contrast for easy viewing. Brightness refers to the overall lightness or darkness of the image, whereas contrast is the difference in brightness between objects or regions. Adjustment of the contrast and brightness enable visualisation of different features in the image [189]. However, some algorithms used for Doppler velocity tracing include no such adjustments.

In [106], the authors performed contrast adjustment by subtracting the original greyscale image from the image obtained by morphological operations using disk approximations.

Image binarization

To extract the velocity profile from the Doppler, the image is usually binarised. In general, an image can be binarised using an edge detector or threshold techniques. Specifically, segmentation is used to subdivide an image into its constituent regions or objects. Most segmentation algorithms are based on one or two basic properties of intensity values: discontinuity and similarity. Regarding discontinuity, the idea is to partition an image based on abrupt changes in intensity, such as edges. Considering similarity, the idea is to partition an image into uniform regions according to predefined criteria, such as colour, grey level, etc. Thresholding, region growing, region splitting and merging are examples of these approaches [189].

Edge detectors Edge detection is based on detecting sharp and local changes in intensity. There are different types of edge detectors, which were used for

this specific application, that will be presented hereafter.

Non-linear Laplace edge detector A modified version of the NLLAP edge detector [214] was adopted by the authors of [209], whereas others have used a combination of the NLLAP and the Sobel edge detectors [72].

The NLLAP edge detector, [214], exhibits excellent performance even at very low signal-to-noise ratios. Its algorithm, derived from the original NLLAP detector, is as follows:

$$NLLAP(x, y) = grandmax(x, y) + grandmin(x, y) \quad (5.2)$$

where:

$$grandmax(x, y) = \max_{i \in N_4} [I(x_i, y_i)] - I(x, y) \quad (5.3)$$

$$grandmin(x, y) = \min_{i \in N_4} [I(x_i, y_i)] - I(x, y) \quad (5.4)$$

for every pixel in the input-image. The pair (x, y) represents the set of coordinates of the centre pixel. N_4 is the set of all four neighbours connected to the centre pixel. The function $I(x_i, y_i)$ represents the intensity (brightness) of the underlying pixel.

We note that this algorithm is adaptive in nature. At each kernel position, the neighbours delivering the highest and lowest gradients are chosen, and the other neighbours do not contribute to the result in that point. The result obtained from Eq. 5.2 consists of regions with positive and negative values, possibly separated by a band of zeros. Each pixel with a zero value is assigned to its nearest region, either positive or negative. Edges are then positioned at the locations of the zero-crossings. The strength i_e of an edge is given by:

$$i_e = \min[grandmax(x, y) - grandmin(x, y)] \quad (5.5)$$

The edge detector delivers a greyscale image with intensities corresponding to the edge strength. However, a binary image is needed to extract the

Doppler envelope. Weak edges are often spurious and due to noise, which varies significantly across Doppler images. This means that the choice of an appropriate threshold for tracing the velocity envelope is directly related to the image content and must be determined adaptively. This is achieved by taking several small areas of the original image near the horizontal axis and evaluating their means and standard deviations. The sample with the lowest mean value is taken as representative of the background and the values of its mean (m_b) and standard deviation (σ_b) are used for selecting the threshold value t using Eq. 5.6:

$$t = \begin{cases} l_1 & \text{if } m_b < m_{th} \text{ or } \sigma_b > \sigma_{th} \\ l_2 & \text{otherwise} \end{cases} \quad (5.6)$$

where l_1 , l_2 , m_{th} , and σ_{th} are empirically determined beforehand. The authors in [72] used a combination of a Sobel operator [70] and a NLLAP edge detector [214].

The Sobel edge detector [70] is a gradient-based method that uses first-order derivatives approximated using 3×3 kernels. The results can be combined to find the absolute magnitude of the gradient, which represents the output edges with larger values.

Canny Edge detector In [106], the authors applied Canny edge detection to binarise the image. After performing noise reduction using a Gaussian filter, the Canny algorithm [30] employs four filters to identify the horizontal, vertical and oblique edges (in given ranges), which are obtained by the first derivatives of a Gaussian. Then, edge points are detected as local maxima of the derivative (in a given direction). To trace the contours, a hysteresis-based process is controlled by two thresholds to limit fragmentation of the reconstructed edges.

Threshold binarization Because of its simplicity and low computational cost, image thresholding holds a central position in image segmentation applications [69]. Several threshold techniques have been presented in the literature with respect to Doppler velocity-envelope tracing.

Otsu Threshold The Otsu threshold [148] is based on the assumption that the histogram of a given image is bimodal, so that two classes of pixels (the background and the content of interest) can be identified. To this end, it computes the optimum threshold that can separate the two classes, where the intra-class variance is minimal. This threshold was used by the authors of [200]. The Doppler spectrum covers a large part of the greyscale range. To effectively separate information of interest, in [195, 196], the authors binarised the image using a global threshold obtained from a grey-level-median histogram based on the two-dimensional (2D) Otsu method. In this method, a 2D histogram is built, but instead of using the grey level and average grey value of the neighbourhood of image pixels, the grey level and the median of the neighbourhood of image pixels is used, which can effectively separate noise pixels from the object and background regions [180].

Steepest gradient histogram In [235], the authors empirically selected the optimum value for contrast thresholding using the steepest gradient method. To separate the foreground from the background, a good threshold has been suggested to be 80% of the x-intercept of the steepest tangential line to the gradient of the image histogram [114]. However, in [235], the authors considered the optimum threshold to be the value for which the gradient of the image histogram reached its peak, which represents the background pixel values in a greyscale Doppler image.

Local adaptive threshold To automatically extract the Doppler velocity profile from Doppler images, a local adaptive thresholding algorithm was developed and applied by the authors of [123]. Adaptive thresholding takes into account the spatial variations in illumination. To account for variations in illumination, a different threshold is computed for each pixel in the image. In their study, first, the region of interest (ROI) was divided into three partially overlapping and rectangular regions of equal size. Then, for each ROI, an inverse normalised cumulative intensity histogram was computed. The threshold for a given ROI was estimated as the 25th percentile of the pixel intensities. In overlapping areas, they used the average of the thresholds of the two adjacent

regions.

Image post-processing: Noise Suppression

Mathematical morphological operations are commonly used as image processing tools for extracting image components that are useful for representing and describing a shape in the image. Image enhancement using morphological approaches has been widely addressed in previous experimental research on Doppler velocity-envelope tracing, primarily to reduce residual noise [91]. The two most common types of additive noises are Gaussian and salt-and-pepper noise [91]. Even though noise is ordinarily removed by spatial or frequency-domain filters, morphological processing may be more frequently adopted to reduce noise in binary images. Basically, a dilation step is applied to fill the small holes in bright regions to yield a clean velocity signal. Therefore, to filter out small noisy clusters, connected areas with fewer than a predefined number of pixels are removed; this number was empirically selected to be 500 pixels in [235], 50 in [200] and 70 in [196]. Region growing [60] a simple region-based image segmentation method, was used in the post-processing image phase by the authors of [209]. This segmentation approach examines the neighbouring pixels of initial seed points and determines whether these pixel neighbours should be added to the region. Starting from a seed-point, the flood-fill algorithm finds all connected pixels of the same value and deletes small spurious areas from the image.

Envelope Extraction

The outline of the part of interest in the image, that differs from the background, should be a good estimate of the Doppler velocity profile and can be extracted in two lines representing the upper and lower profiles, respectively. In the literature, two main envelope extraction methods are presented, as follows.

The biggest gap method The biggest-gap method [72] defines a column vector that moves across the image from left to right. Within this column vector, the sub-vector with the highest count of consecutive black pixels is

identified. A gap comprises the identified consecutive black pixels. The biggest-gap algorithm weights gap values according to their vertical positions, so that a gap in the central part of the search space is more significant than those in the upper and lower parts. The lowest pixel of the largest gap, considering all the position-dependent weighted gaps, is labelled as part of the envelope function.

White region contour method Another method, used in [196, 235], traces the boundary pixels of all white regions to obtain contours as follows:

$$G_u(x) = (\operatorname{argmax}_y I(x, y) = 1) - y_b \quad (5.7)$$

$$G_l(x) = (\operatorname{argmin}_y I(x, y) = 1) - y_b \quad (5.8)$$

where y_b is the baseline position, the horizontal axis line that separates the image into two parts containing the negative and the positive waves, whose polarities depend on the direction of the blood flow away from, or towards, the transducer.

Envelope post-processing

Finally, to remove the effect of spiking artefacts or to smooth the velocity signal, a temporal median filter with a variable window size can be applied. A median filter operates by evaluating the median value within a sliding window of a given size, thus providing a smoothing effect that is less sensitive to outlier values than the moving average filter. In [209], to suppress the effect of remaining noise, a five-point averaging filter is applied to the envelope curve, whereas in [123], the extracted envelope is filtered using a median filter, with order 15, to remove outliers and artefacts. The sampling frequencies of the envelope were not specified in that paper, so that the cut-off frequency of this filter is not clear. In the study reported in [200], to remove the effect of spiking artefacts on the extracted envelopes, the authors employed a temporal median filter with a window size of three pixels. Considering a sampling frequency of 500 Hz, the cut-off frequency was around 78 Hz. In [235], a Butterworth

low-pass filter was used to suppress high-amplitude outliers and artefacts in the velocity profile. Any frequency ten times higher than the fundamental frequency of the heart motion was filtered out. This ratio was selected empirically as a trade-off between noise removal and waveform accuracy. The low-pass filter is also crucial for isolating individual cardiac cycles. In this study, we compared four different filters, a median filter of order 15, a five-point averaging filter, a median filter with a window size of two samples and a cut-off frequency of 71 Hz, and a first-order Butterworth filter with a cut-off frequency of 70 Hz.

Classifier

In this study, to evaluate the impact of the different steps in terms of classifier accuracy, an ANN was chosen as classifier. The use of this ANN was previously investigated in [196], in order to classify the window of the signal where there is a complete and measurable cardiac cycle.

The classification problem has a binary output: 0 for an incomplete, malformed or unrecognized cardiac cycle and 1 for a complete and measurable one.

The number of inputs of the ANN depends on the size of the feature vector. In this work, the ANN is feed by windows of the two vectors $G_u(x)$ and $G_l(x)$, normalizing them respectively between 0 and 1 and between -1 and 0, and the area under the remaining 64 samples of both signal. Moreover, the mean values of the pixel included in the aforementioned four areas, were computed.

The windows length was chosen in order to be the most representative length of a cardiac cycle of a fetus between the 21st to the 27th gestational week. A healthy fetus of that gestation age could have a heart rate ranging from 110 to 160 bpm [157], so considering a sampling frequency for the envelope signals resulting from the video equal to 284 Hz, a length of 128 samples was chosen.

Therefore, the ANN characterized by 264 input nodes, 10 hidden nodes and 2 output nodes was trained using the scaled conjugate gradient backpropagation algorithm.

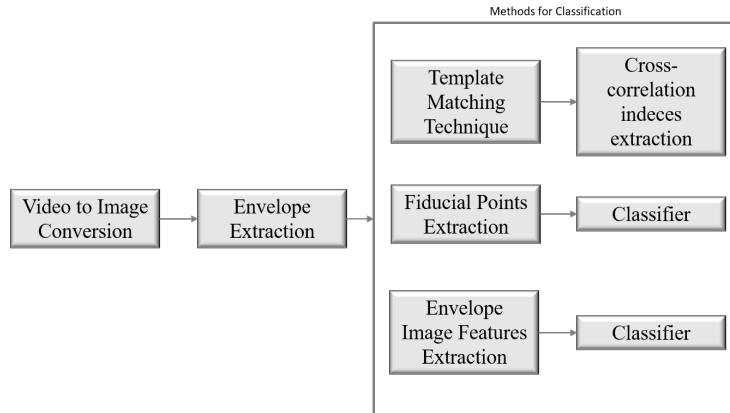


Figure 5.4: The different toolchains studied in this work.

5.5.2 PWD automatic classification

In this section, three techniques developed for the automatic identification of the complete fetal cardiac cycle in PWD signals are presented. The three methods share the same procedure for the extraction of the envelope from the PWD video (see figure 5.4).

Based on the original single wide PWD image, the envelopes were affected by different artifacts. For instance, with a moderate increase in gain, the velocity tracing thickened and the spectrum broadened [158]. Additionally, a typical mirror image artifact could appear. Furthermore, with the chosen apical five-chamber view, mitral and aortic valve closure were typically present as spikes in the PWD envelopes. Regardless of the method, the presence of these residual artifacts limits automatic detection.

Method 1: Template matching

The morphology of the PWD presents a typical $EA-V$ pattern of the chosen apical five-chamber view of healthy fetuses. In particular, the atrial activity is characterized by two peak velocities, E and A , which form an “M” shape. The shape of the V wave, that is present after the EA -wave, is reasonably the same

across subjects, changing only for its amplitude. However, *EA*-wave can slightly change, as can be seen from figure 5.5a. By identifying different templates for the atrial activity, well represented in the available signals, it is possible, in principle, to identify the complete fetal heart beats by a template matching approach. Figure 5.5b shows the selected set of atrial activity templates (upper envelope) used for this method, that respectively corresponds to the real PWD atrial parts in figure 5.5a. Such templates were chosen by looking at the PWD signals available in the adopted dataset, according to the pediatric cardiologist's indications, in order to represent the largest part of *EA*-patterns.

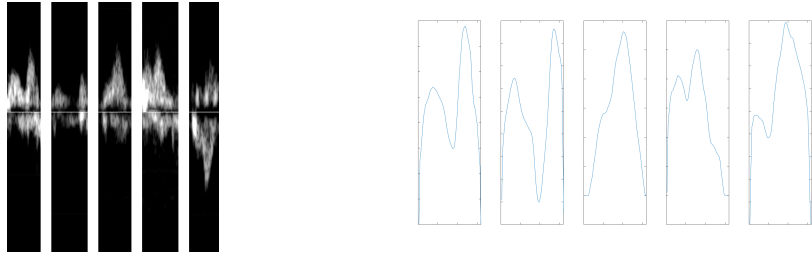
The *E* and *A* waves of the transmitral spectral Doppler envelope could be completely detached, with an *E*-wave that is occasionally barely identifiable as a separate peak. By considering the envelopes sampling rate and the mean cardiac cycle duration, which is approximately 128 samples, and considering that the available dataset includes only healthy fetuses with a 1:1 *AV* conduction, on average, the length of the templates for the fetal atrial activity is about 64 samples.

A sample-by-sample sliding window to compute the normalized cross-correlation between the five templates and the whole upper PWD envelope was adopted. A complete and measurable fetal cardiac cycle was detected using this method when at least one cross-correlation signal in that point was above a threshold (equal to 0.6) chosen to maximize the performance on the available dataset. This simple method did not require any classification stage downstream as opposed to the other methods.

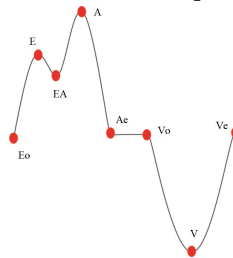
Method 2: Classification Based on Fiducial Points

A more sophisticated delineation-based approach was developed to characterize the envelopes over a time frame lasting as long as a full cardiac cycle. To this end, a supervised classification approach was adopted by extracting meaningful features from each signal frame. Eight fiducial points characterizing the two envelopes (five for the upper envelope and three for the lower envelope, see figure 5.5c) were identified:

1. Onset of the *E* wave (E_o)
2. *E* peak (E)



(a) Five different atrial activity patterns (b) The five atrial activity templates obtained by extracting the upper envelope of the PWD signals in (a).



(c) Fiducial points on the PWD cardiac cycle pattern.

Figure 5.5: Automatic detection methods.

3. The intersection point between the *E* and the *A* waves (EA)
4. *A* peak (A)
5. End point of the *A* wave (Ae)
6. Onset of the *V* wave (Vo)
7. *V* peak (V)
8. End point of the *V* wave (Ve).

In order to smooth the velocity profile, a three-tap median filter was applied to the initial velocity profile. Then, the average fetal cardiac cycle duration was estimated for that signal by detecting the *V* wave in the lower envelope and computing the *V-V* intervals. Unfortunately, valve closure clicks can affect the estimation of the *V-V* interval, which is used to set some thresholds needed for

the fiducial points detection. Fiducial points were detected in the order reported in the aforementioned list.

Because the onset of the *E* wave lays on the *x* axis, it was detected by selecting the first non-zero sample after a sequence of zeros. Since, in the presence of noise, the onset is no longer on the *x* axis, if such method fails, the *E* wave onset was detected by imposing the constraint that the distance between two consecutive onsets should be not larger than the duration of two average cardiac cycles, and detecting the local minimum within a window of reasonable length, according to physiological constraints. Furthermore, because of the presence of the valve clicks, the detection of some *E*-wave onset points could be erroneously marked at the onset of the valve click rather than at its end. To correct these cases, the valve click was detected by using the first derivative of the upper envelope and the *E*-wave onset identified at the end of the valve click.

The *A* peak was detected as the local maximum in the interval between the *E* onset and half of the average cardiac cycle duration. Then, the *E* peak was detected as the local maximum in the interval between the *E* wave onset and the *A* peak.

The conjunction between the *E* and *A* waves was detected as a minimum (see the first, second, fourth and fifth templates in figure 5.5b) or a flat portion (see the third template in figure 5.5b) of the curve. The last point of the upper envelope was the end of the *A* wave, recognized by the sharp decrease in the envelope, taking the minimum reached in the declining slope.

Regarding the lower envelope, the first point to be searched was the onset of the *V* wave owing to the known position of the end of the previous *A* wave. Then, the end of the *V* wave was found in the interval lasting as long the average cardiac cycle duration and starting from the onset of the *V* wave. Again, the first derivative of the velocity curve was used to correct the position of that point in case of the presence of valve click artifacts.

Between the onset and the end of the *V* wave, the local minimum was recognized as the *V* peak.

These eight fiducial points can be described using 16 coordinates (time and amplitude). All the time coordinates can be referred to the *E* wave onset of that cardiac cycle, such that their values are not dependent on their occurrence over

time in that cycle. This implies that the E onset time is no longer useful for the remainder of the algorithm; as such, seven time features can be extracted from the eight fiducial points. The other eight amplitude features can be extracted, as the amplitudes of the eight fiducial points, for a total of 15 features. Then, a supervised classifier was trained to identify the complete and measurable cardiac cycles in the PWD signal from these features. Since this last step is common to the third method as well, it is described later in this section.

Method 3: Classification based on the envelope, area and pixels

Residual ultrasound artifacts, including mirror images, may hide the cardiac cycle information, limiting the fiducial point detection and reducing the effectiveness of template matching. The third method was created to overcome these limitations exploiting as classifier features the complete envelopes of the PWD signal. This approach, first investigated in [196] and [195], provides the largest set of available information to the classifier without any preliminary identification of the waveshapes of interest or any delineation of the PWD trace, the errors of which could impact the quality of the final solution. Simultaneously, the dimensionality of the problem was significantly reduced using the envelopes rather than the image. The upper and lower envelopes were considered over a time frame representative of the duration of a fetal cardiac cycle in the studied gestational weeks, as previously performed for the template matching approach. Then, an analysis window size of 128 samples was adopted, leading to 256 features for the classifier (128 for each of the upper and lower envelopes).

Moreover, four additional features associated with the area under the curve were introduced. Based on an AV conduction of 1:1 in healthy fetuses so that the ventricular activity was always expected after the atrial activity, the areas between the x axis and upper and lower profile envelopes were computed on the first and second half of the analysis window.

Furthermore, four additional features based on the pixel analysis were added to improve the classifier performance (shown in the work [196]). The brightness information is very useful for the recognition of the meaningful part of the image. In fact, ultrasound artifacts could be less bright than the portion of the signal of interest; moreover, the cardiac cycle parts are characterized by the same

brightness across different heart beats in the same trace. Therefore, the mean brightness of the pixel enclosed in the four areas were computed. Overall, 264 features were chosen: 128 samples of G_u , 128 samples of G_l , four area features and four brightness features.

Pattern Recognition

Two different classifiers were adopted to assess the robustness of the second and third methods described in the previous sections for the automatic identification of complete and measurable fetal cardiac cycles in the PWD signal: ANN [80] and SVM [215]. Again, the classification problem has a binary output: incomplete or complete and measurable heartbeats. The use of an ANN was previously investigated in [196] for the third method, whereas the SVM was introduced in this work because of its capability to solve non-linearly separable classification problems by the adoption of non-linear kernels.

Depending on the method (exploiting the fiducial points or whole envelope), the ANN was characterized by a different number of input neurons. However, in both cases, ten hidden neurons and two output nodes were always used, and the scaled conjugate gradient backpropagation algorithm was exploited for training. The number of neurons in the hidden layer was empirically chosen to obtain an acceptable performance on the available dataset without incurring an overfitting problem.

A second classifier was also tested, i.e., an SVM with a Gaussian radial basis function kernel, $\nu = 0.5$, and box constraint set to 1.

5.5.3 Parameters and indexes from Doppler Ultrasound

The algorithms described in this part are related to the computation of the clinical parameters extracted from the PWD. The algorithms described in this part are beat-gated, it means that they need that the cardiac cycles are previously labelled by the cardiologist or by an automated classifier, as the ones that are presented in this chapter.

Fetal Heart Rate

Referring to section 2.4.3, the fetal HR can be estimated computing the time interval between the V peaks.

First of all, the absolute value of the lower envelope, where the V peaks are located, is considered. The signal is filtered by applying an average filter of 16 taps, able to reduce the noise on the signal, especially to remove the spikes due to the aortic valve closure. Considering the labelled cardiac cycles, knowing the average length of a cardiac fetal beat, through appropriate indexing it is possible to obtain the portion of the signal where the V wave should be located. In this part of the signal, the maximum is selected as the V location.

AV interval

The AV interval is computed through the distance between the onset of the A-wave and the beginning of the V-wave. To obtain the AV interval, it is necessary to work on both envelopes. Each signal is first filtered using a moving average filter with a length of 4. For the onset of the A-wave, the upper envelope is used and through appropriate indexing, the algorithm extracts the portion of the signal representing the biphasic atrial wave.

First, we want to identify the portion of the signal where the slopes change. Looking at the points where the first derivative is equal to zero, several local maxima and minima are selected. Now, we want to discriminate the onset of the A wave and the A peak. This couple of points are going to be found using heuristic methods. The signal is noisy so that several local maxima and minima characterized the trace. Working on the maxima and minima obtained from the zero crossing on the first derivative, the algorithm excludes the couple of points that are at the beginning of the atrial window and those ones that are too close to each other, since they show irrelevant changes in slope. The result is a profile of the derivative with significant local maxima and minima. At this point, the algorithm tries to discriminate the desired local minimum. The onset of the A-wave is a minimum reasonably between two maxima, the E and the A peaks; therefore, during the processing, several configurations of the 2 maxima and one minimum are analyzed. Interpolating the points of the examined configuration,

the algorithm calculates two areas, the first between the maximum that is the peak index of A wave and the minimum, and the second calculated between the other maximum and the minimum. Considering the ratio between the two areas and evaluating the distance between the maxima and minimum indices, the algorithm, by applying an adaptive threshold, is able to discriminate the local minimum that identifies the onset of the atrial A wave.

Regarding the detection of the onset of the V wave, the used approach is the same.

The myocardial performance index (MPI)

The myocardial performance index (MPI) depends on three intervals, ICT, IRT and ET.

For the computation of the ICT interval, we still need to obtain the offset of the A wave, since the onset of the V wave can be identified using the algorithm described in the previous section. By analyzing the upper envelope, the offset of wave A was calculated using the same approach described in the previous section that exploited the maxima and minima, the areas identification and the adaptive threshold method.

To calculate the IRT interval, the offset of the V wave is identified with the same method used to define the onset of the V wave, while the onset of the E wave was detected selecting the points where the signal changes slope and by applying a threshold on the identified points.

Regarding the ET interval, the onset and the offset of the V-peaks are needed, and they can be obtained as previously described.

E/A ratio

The Doppler signal envelope used for the E/A ratio computation is the upper envelope. The signal is filtered by applying a moving average filter with a narrow window of 4 taps. The peaks are identified as the maxima in a physiological-appropriate window.

Remarkably, detecting the E-peak is more complicated since the atrial wave morphology is not always the same.

5.6 Performance assessment

To evaluate the impact of the different steps on the whole envelope extraction processing chain, we determined the accuracy (*Acc*) as follows:

$$Acc = \frac{TP + TN}{P + N} \cdot 100 \quad (5.9)$$

where *TP* is the number of true positive detections, *TN* is the number of true negative detections, *P* is the number of positive samples and *N* is the number of negative samples.

The aim of the performance assessment was to first highlight the impact of the different steps in the prototypical processing chain, and then identify (without performing an exhaustive search) the 'best' chain. To meet the first objective, we changed the prototypical processing chain one step at a time and experimented on the different solutions available for that step.

To identify the 'best' processing chain, the prototypical chain was changed first by adopting the best performing solution among those available. Then, using this modified chain, the second step was investigated to find the method with the best performance and the processing chain was changed accordingly, continuing in this way to test the third, fourth, fifth and sixth block, each time by improving the previously defined chain. Even if the ultimate version is not the 'best' chain, it is a reasonable approximation of it.

Next, a statistical analysis was performed to investigate the significance of the results of the different steps and to build the 'best' processing chain. First, the normalities of the distributions were determined using the Lilliefors test. If a result did not satisfy the assumption of normal distribution, a non-parametric statistical test was adopted. In particular, we used the Kruskal–Wallis test for comparisons involving more than two distributions to verify that they all actually came from the same distribution. Otherwise, we used the Wilcoxon signed rank test when comparing only two distributions to verify the statistical difference between the two. When the results of the Lilliefors test satisfied the assumption of normal distribution, we then adopted the Student's *t*-test for paired data. In all the statistical tests, we considered 'statistical significance' to be $p < 0.05$.

To assess the performance of the comparison of the three methods for the automatic recognition of the complete heartbeats, the accuracy (Acc) was computed as Eq. 5.9. For the template matching technique, the results were compared directly with the annotated cardiac cycles leading to a single accuracy value. Furthermore, statistical analysis was performed to investigate the significant differences between the following: (i) the two classifiers (ANN and SVM) among the second and third techniques and (ii) the second and third methods.

We adopted a leave-one-subject-out cross-validation scheme corresponding to a 25-fold cross-validation but without any randomness in the selection of the samples in the test set. This approach was considered to be fairer than a normal k-fold stratified cross-validation since the leave-one-subject-out approach did not train the classifier at all on any heartbeat coming from a given subject, which is what can happen when this type of system is integrated into an ultrasound device. Using this validation scheme, we obtained 25 accuracy values. To assess the symmetry of the distributions, we adopted box-and-whiskers plots. In these plots, the median value is highlighted inside a box ranging from the 25th to the 75th percentiles and the whiskers range from the minimum to the maximum number of samples that cannot be considered to be outliers (represented by red crosses).

Regarding the indexes from the PWD trace, the results obtained from the automatic intervals computations are shown and compared to the literature values and to the manual annotations carried out by an expert cardiologist.

5.7 Results and discussion

In the three following sections, the results of three different parts of the study are shown and briefly commented.

5.7.1 PWD envelope extraction chain

Results for the individual steps assessment

The accuracy values in figure 5.6 clearly demonstrate that two main steps have a big influence on classification: image binarisation and envelope extraction. For image binarisation, the Kruskal–Wallis test revealed that the accuracy values are from different distributions ($p < 0.001$). The results from the pairwise Wilcoxon tests for those steps show a significant difference between the method adopted by the MC and the others ($p < 0.001$).

Conversely, the same analysis applied to the image preprocessing and post-processing steps revealed no statistically significant differences ($p > 0.05$). Lastly, for the last step of the chain, even though the accuracy values are from different distributions, according to the Kruskal–Wallis test ($p = 0.04$), the envelope post-processing methods exhibit no statistically significant differences in their pairwise comparisons ($p > 0.05$).

From this analysis, we can conclude that, regarding preprocessing and post-processing of the images, performing no operation or trying to improve the image quality to emphasise the signal of interest has no effect on the classification. This finding also applies to the post-processing of envelopes, for which the performance improvement is very limited.

Regarding image binarisation, we can observe that the Canny and NLLAP edge detectors are not reliable for PWD images. The combination of NLLAP and Sobel edge detectors improved the output, compared to the use of the NLLAP alone, thus confirming the conclusions drawn by the authors of [72]. Nevertheless, of the group, the Otsu 2D method demonstrates clear superiority ($p < 0.001$). Considering envelope extraction, the comparison of the two methods reveals the clear superiority of the white-region contour method ($p < 0.001$).

Identification of an effective processing chain

Table 5.2 presents the results regarding the selection of the best processing chain. At each step, we evaluated the different options, leaving the rest of the processing chain unchanged. To highlight the significant differences between the achieved results, the last row of table 5.2 lists the p -values obtained from

the Kruskal–Wallis test for all the options available for that step. We identified the best method for a single step by selecting the one that achieved the best accuracy (based on a consideration of the mean for the 25-fold validation scheme). Then, we used the Wilcoxon signed rank test to make a pairwise comparison with the others, the p -values for which are reported below.

Based on this approach, the following best chain was identified. Step 1: Gaussian low-pass filter ($p = 0.54$); Step 2: k-means clustering contrast adjustment ($p > 0.05$); Step 3: binarisation using 2D Otsu thresholding ($p < 0.001$); Step 4: removal of spurious areas (less than 500 pixels) ($p > 0.05$); Step 5: trace the boundary pixels of all white regions to obtain contours ($p < 0.001$); and Step 6: smooth the envelope using the median filter with a cut-off frequency of 70 Hz ($p > 0.05$).

Comparison of different chains

The last analysis we performed in this study was a comparison of the workflows presented in the literature (see table 5.1) with those of the ‘best’ chain and a randomly-composed chain, composed of the concatenation of six methods that were selected randomly among all the available processings, one for each step. Figure 5.7 shows the results of this comparison. Based on their performances, the Kruskal–Wallis test clearly indicates that the distributions of the tested chains are statistically different ($p < 0.001$). Moreover, we pairwise compared all the distributions with that of the best chain (chain 8) using the Wilcoxon signed rank test. All the comparisons, except that with chain 7, revealed statistically significant differences ($p < 0.05$). It is not surprising that chains 7 and 8 achieved almost the same accuracy values because they adopted the same methods for image binarisation and envelope extraction, which were identified as the most important steps in the work chain.

The results also reveal that the chains presented in [209], [72], [235] and the random chain exhibit accuracy performances far below minimum expectations and should be avoided as reference scenarios. Even though the techniques presented in [200], [106] achieve higher median accuracies than the worst chains,

above 90%, their distributions are wider. This result suggests again that image binarisation is a critical step and it is better to use a thresholding technique than an edge detector for the purposes of our study involving PWD signals.

Chain 4 [123] uses the same envelope extraction adopted by chains 7 and 8, but not the same binarisation technique (adaptive thresholding rather than the Otsu 2D). If we look at figure 5.6, the adaptive threshold (method 7) and Otsu 2D (method MC) present similar distributions. Moreover, from table 5.2, we can see that the adaptive threshold (method 7) achieved high performance in terms of classification accuracy.

5.7.2 PWD automatic classification

The accuracy for the first method (template matching) is limited to 48.5%. The poor performance could be attributed to the selection of templates based on the fetal heart rate. To exclude the possible occurrence of this effect, different heart rates within the dataset were checked to prevent the presence of outliers that could affect the performance of the algorithm. Since no outliers were detected, the results of the first method were not influenced by the chosen length of the templates. Another explanation for this unsatisfactory result could be the set of templates identified to represent the atrial activity patterns. However, the templates were extracted as those resembling the largest part of the atrial activities in the beats annotated as complete and measurable by the cardiologist. Further analyses, possibly including the ventricular activities, did not improve the algorithm performance (data not shown). Another parameter that could have influenced the results is the template matching threshold. The confusion matrix, which represents this result (figure 5.8), shows a really high number of the FP with the chosen threshold. By increasing the threshold, the number of FP decreases, but the number of FN grows. The selected threshold was chosen to be a good compromise. In the end, the noisy nature of the signals, imperfect envelopes, and presence of the valve clicks could have contributed to this poor performance.

About the second and third methods, figure 5.9 allows appreciating the robustness of the proposed solutions with respect to the chosen classifier model, excluding a large bias in the results due to this choice. The SVM and ANN

performed similarly. However, from the statistical analysis it is possible to exclude the significant superiority of a classifier compared with the other for the second method, where the achieved p -value was 0.97, whereas the p -value was 0.001 for the third method, which revealed a significantly better performance of the SVM with respect to the ANN.

From a comparison of the second and third methods, the superiority of the latter compared with the former is evident ($p < 0.0001$ regardless the classifier model). The reduced feature set for the second method, possibly along with an imprecise identification of the fiducial points in the presence of noise, was probably responsible for its relatively poor performance. This problem could be overcome by a more sophisticated algorithm for the detection of the fiducial points characterizing EA and V waves. However, either the optimization of the delineation algorithm or its validation through manual annotation (requiring a huge annotation work by the cardiologists) was beyond the scope of this research. Conversely, the third method, not requiring complex feature extraction stages, was able to accurately distinguish complete and measurable fetal cardiac cycles from incomplete or not meaningful cycles, reaching a mean accuracy of 98% with a standard deviation of 1% using the SVM classifier ($97.63\% \pm 2.09\%$ for ANN). Remarkably, the number of features is significantly lower than the number of pixels in the images corresponding to the extracted windows, so the complexity of the classifier model is reduced.

5.7.3 Parameters and indexes from Doppler Ultrasound

Comparison with literature values

The reference values for each interval were already presented in section 2.4.3. For the sake of clearness, hereafter, they are reported again.

- fHR: the literature shows that a normal fetal HR is between 110 and 160 bpm among the 21st and the 27th week of gestation.
- AV Conduction Time: this time interval, indicating a good condition in fetuses with a gestational age between 21st and 27th weeks, presents

acceptable values in the range 137 to 146 ms.

- MPI: it is based on gestational age and the normal values are between 0.3 and 0.65. The limitation of this computation is due to the possible error propagations caused by the three different measurements.
- E/A ratio: in a fetus, it is always a value < 1 .

As it can be observed from figures 5.10, 5.11, 5.12 and 5.13, the indices obtained from the automatic measurements are in line with the values in literature.

Comparisons with the manual annotation

For this preliminary work, we have 40 manual annotations per index.

In order to assess the agreement between the manual annotation and the interval computed using the above-described algorithms, we used the Bland-Altman analysis, that quantifies the agreement between the two measurements by studying the mean difference and constructing limits of agreement.

The Bland-Altman analysis for the fHR, figure 5.14, reveals how the adoption of the algorithm is promising.

The AV interval results, figure 5.15, show that the algorithm needs to be improved. In fact, detecting the beginning of the A wave is often difficult because of the different atrial activity morphologies (figure 5.5). As it was previously explained, the E and A waves of the transmitral spectral Doppler envelope could be completely detached or the E-wave can be occasionally barely identifiable as a separate peak. The E peaks sometimes are not even appreciable, so that also the performances for the E/A ratio algorithm, (figure 5.17), are lower.

Regarding the low performance of the MPI index, figure 5.16, as already mentioned, it can be due to the error propagation generated by the computation of three intervals that depend on six markers.

5.8 Conclusion

To date, many studies of cardiac ultrasound signal processing have been reported with the aim of identifying good processing chains to achieve an optimal approximation of the Doppler velocity profile. In this work, we leveraged these studies by combining the techniques they used with a supervised classifier, a simple ANN, as described in [196], to obtain indications of the presence of complete and measurable fetal heartbeats from the PWD envelope. We investigated the impact of the different steps in the processing chain and compared the different techniques on the same dataset to define the ‘best’ processing chain in terms of classifier accuracy.

Even though we could identify a ‘best’ processing chain and our comparison of different techniques revealed the superiority of some methods over others, when the aim is the recognition of complete and measurable fetal cardiac cycles within a trace rather than the quality of the envelope itself, the role of a single processing step in the chain can have a limited effect. In fact, we found only binarisation and envelope extraction to have a major effect on the final result, so the greatest attention should be paid to the selection of these processing steps.

The analysis of the computational cost of the different solutions presented in this study is beyond the scope of this research work. Even though this aspect is interesting from an engineering perspective, some considerations should be done. At first, for an embedded implementation inside a US machine, the signal would be available in a different form, so that several parts of the proposed envelope extraction methods would be changed. Contemporarily, for the signal post-processing, the computational cost is remarkably less important than the quality of the solution. Nevertheless, this aspect deserves further investigations for time-critical applications.

Moreover, this study analyzed also different methods for the automatic identification of complete and measurable heart beats in PWD traces, acquired based on an apical five-chamber window. The proposed approach can be adopted for the automatic analysis of long PWD traces or embedded in ultrasound devices as a first step for the measurements of useful clinical parameters.

The results reveal how the adoption of a supervised classifier trained with the samples representing the upper and lower envelopes of the PWD, with eight additional features based on the area under the curve of the envelopes and the brightness of the pixels enclosed in such areas, helps in achieving excellent detection results. The results are significantly better ($p < 0.0001$) than those of similar approaches based on reduced feature sets that exploit only some fiducial points on the signal, and dramatically better than the simplest template matching technique.

An important aspect to be considered is that, by dealing with the mitral flow, which is biphasic and characterized by high inter-patient variability in the shape of the PWD, this problem is more challenging than the detection of the monophasic waves [235], so the accuracy results are significantly high and important.

It is also important to underline that the work focused the attention on antenatal PWD, but the same method could also work on the adult cardiac PWD, where the pattern is almost the same, apart from the inversion of the E/A ratio. From this perspective, it is worth to note that the adoption of the proposed method on adults would be definitely easier. In fact, on fetuses, the considered sample volume for a five-chamber apical window is tiny and the fetus is often moving in the womb, whereas the sample volume in adults is bigger and its position is more stable. Remarkably, no compensation for fetal movements can be introduced since their occurrence simply leads to losing the correct sample volume.

The last aspect investigated in this chapter regards the computation of several clinical parameters on the PWD trace. This is only a germinal work, but it can represent a first step to the implementation of a valuable software that can be used real-time by the cardiologist.

By looking at the presented results, some important remarks should be discussed. The achieved results could have been biased by the labelling performed by a single cardiologist. Having a second expert would avoid any bias.

The main limitation of these studies is that the available dataset included

only healthy fetuses, which is motivated by the specific data acquisition protocol approved by the Ethical Committee of the Cagliari University Hospital. A comprehensive study including a large population with CHD and functional problems, showing main changes in the apical five-chamber window PWD pattern, is beyond the scope of the present work. However, it is conceivable that a hierarchical classification scheme can identify the different patterns from incomplete or noisy portions of the recordings. The most significant complexity of this study extension would be the incidence of such diseases in antenatal screening, limiting the acquisition of a significant number of cases for classifier training. Nevertheless, we planned to investigate such an extension in the future.

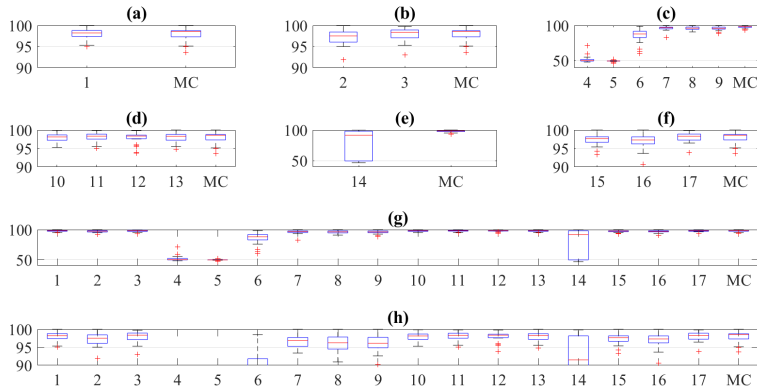


Figure 5.6: a) Step 1: Image preprocessing 1, b) Step 2: image preprocessing 2, c) Step 3: image binarization, d) Step 4: image post-processing, e) Step 5: envelope extraction, f) Step 6: envelope post-processing, g) all tests in a zoom range between 40 and 100%, h) all tests in a zoom between 90 and 100%. The boxplots are divided according to the type of processing phase, and, in each one, the rightmost boxplot always shows the accuracy of the MC. Order: 1. MC with no filter application for image preprocessing 1; 2. MC using as an intensity adjustment the subtraction of the greyscale and modified images; 3. MC using no operation for the image preprocessing 2; 4. MC using Canny algorithm; 5. MC using NLLAP edge detector (NL); 6. MC using a combination of the NLLAP and Sobel edge detectors. 7. MC using an adaptive threshold; 8. MC using the steepest gradient histogram threshold; 9. MC using the Otsu threshold; 10. MC using the region-growing algorithm; 11-13 MC using a morphological operation (MO) with maximum N-connected pixels; 14. MC using the biggest-gap algorithm; 15-16. MC using median filter of different window lengths; 17. MC using a low-pass first-order Butterworth filter.

Table 5.2: Best Chain Results: The MC comprises: Gaussian-shaped low-pass filter with $\sigma = 1.5$, a k-means algorithm to enhance the contrast, the Otsu 2D method, removal of small noisy clusters with 70 four-connected pixels, tracing the boundary pixels of all white regions to obtain contours, and a temporal median filter with a window size of three pixels. In the order: 1. MC using no filter application for the first preprocessing step; 2. MC using as an intensity adjustment the subtraction of the greyscale and modified images; 3. MC using no operation for the second preprocessing step; 4. MC using the Canny algorithm; 5. MC using the NLLAP edge detector (NL); 6. MC using a combination of the NLLAP and Sobel edge detectors; 7. MC using an adaptive threshold; 8. MC using the steepest gradient histogram threshold; 9. MC using the Otsu threshold; 10. MC using the region-growing algorithm; 11–13 MC removing spurious areas using a morphological operation with maximum N-connected pixels; 14. MC using the biggest-gap algorithm; 15–16. MC using median filters of different window lengths; 17. MC using a low-pass first-order Butterworth filter. The bold values indicate the best results.

Step 1	Step 2	Step 3	Step 4	Step 5	Step 6
98.33 (1)	98.12 (2)	51.72(4)	97.83 (10)	49.79 (14)	98.35 (15)
98.36 (MC)	96.15 (3)	49.58(5)	98.06 (11)	98.44 (MC)	98.44 (16)
	98.44 (MC)	85.33 (6)	97.77 (12)		98.05 (17)
		96.08 (7)	97.95 (13)		98.45 (MC)
		95.98 (8)	97.93 (MC)		
		95.96 (9)			
		97.93 (MC)			
p-value = 0.54	p-value = 0.38	p-value = 0.00	p-value = 0.000	p-value = 0.000	p-value = 0.99

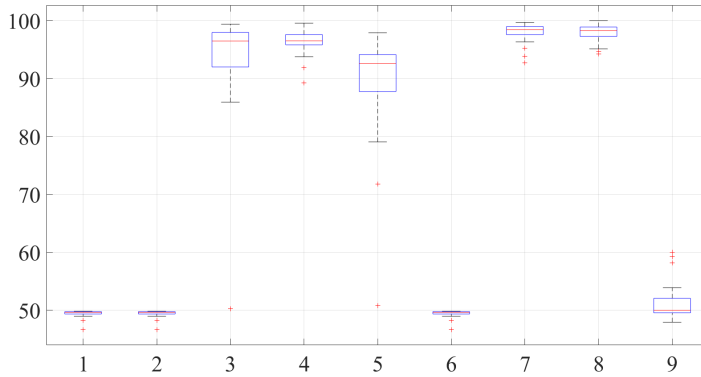


Figure 5.7: Chain 1: [209], chain 2: [72], chain 3: [200], chain 4: [123], chain 5: [106], chain 6: [235], chain 7: [196], chain 8: best work chain presented in this work, chain 9: random chain.

Method 1 result.

	1	2	3
Output Class 1	73842 42.4%	75802 43.5%	49.3% 50.7%
Output Class 2	13894 8.0%	10781 6.2%	43.7% 56.3%
Output Class 3	84.2% 15.8%	12.5% 87.5%	48.5% 51.5%
	1	2	3
	Target Class		

Figure 5.8: Confusion matrix for the first method.

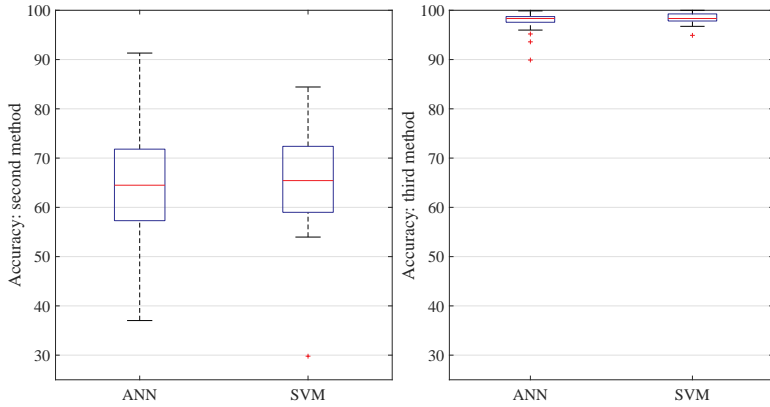


Figure 5.9: Classification accuracy for the second and third methods, respectively on the left and right boxplots, with the two different classifiers model.

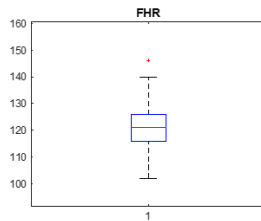


Figure 5.10: Fetal heart rate measured using the algorithm.

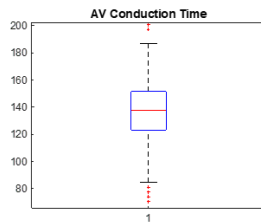


Figure 5.11: AV Conduction Time measured using the algorithm.

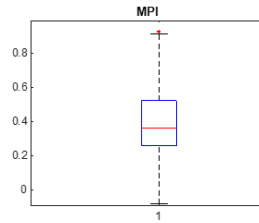


Figure 5.12: MPI measured using the algorithm.

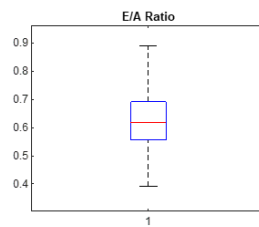
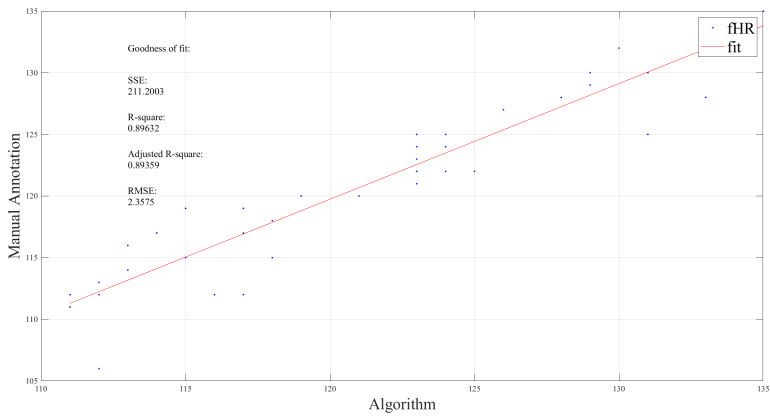
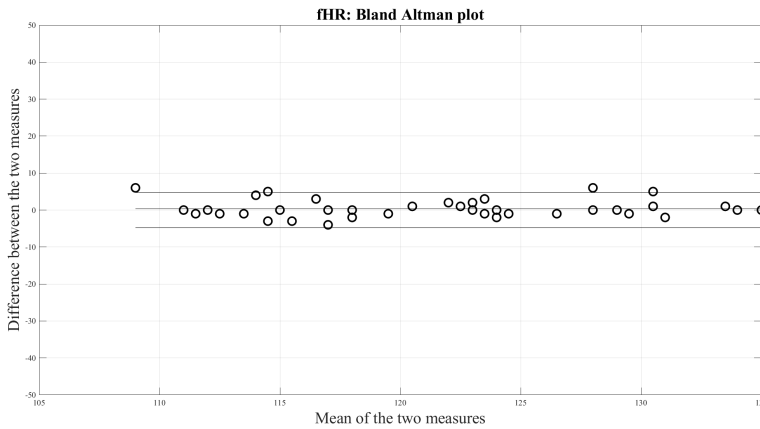


Figure 5.13: E/A ratio measured using the algorithm.



(a)



(b)

Figure 5.14: Bland-Altman analysis regarding the fHR.

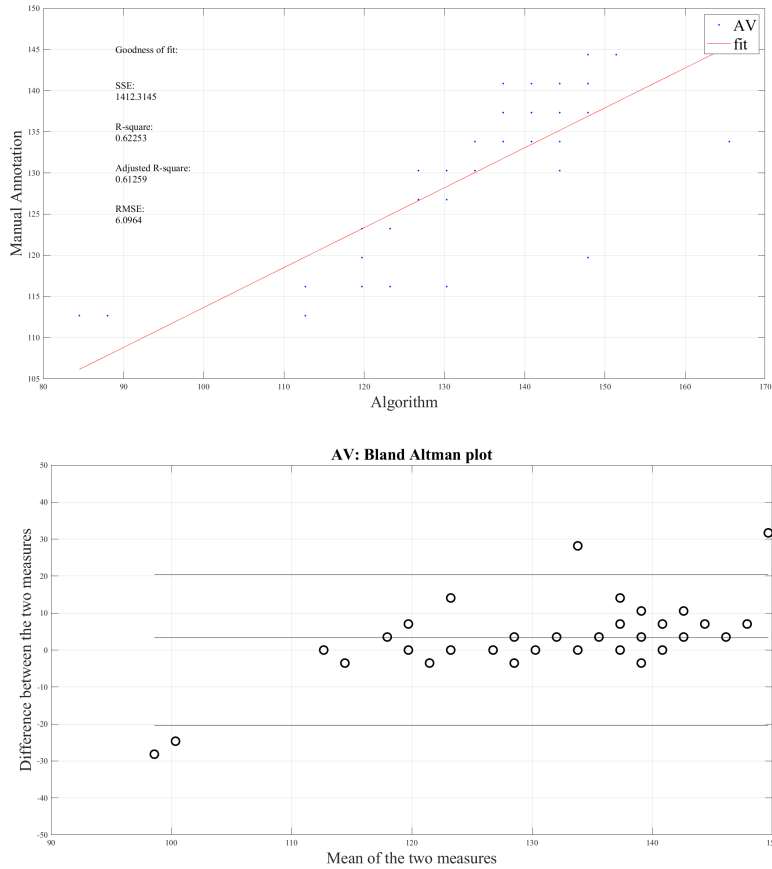
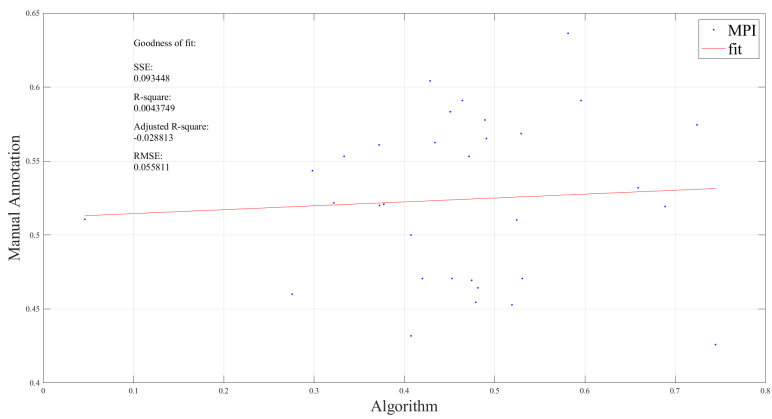
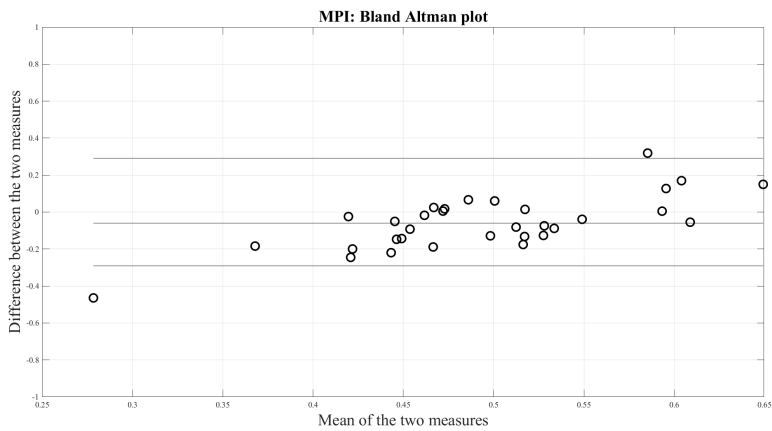


Figure 5.15: Bland-Altman analysis regarding the AV interval.

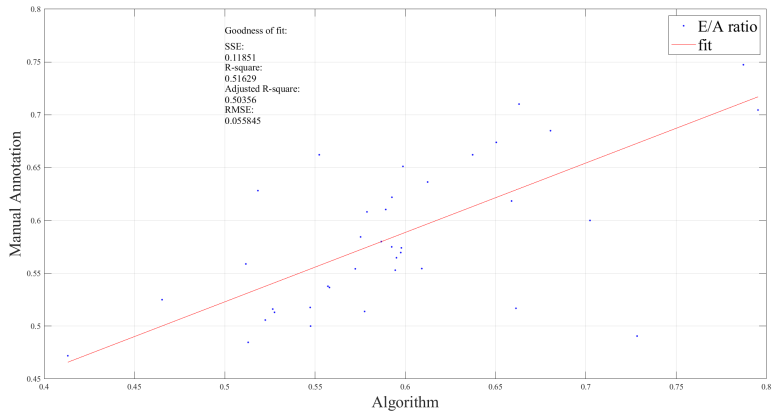


(a)

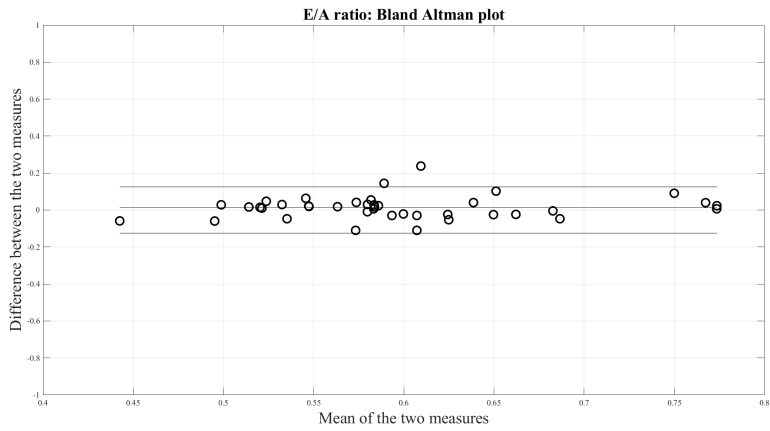


(b)

Figure 5.16: Bland-Altman analysis regarding the MPI index.

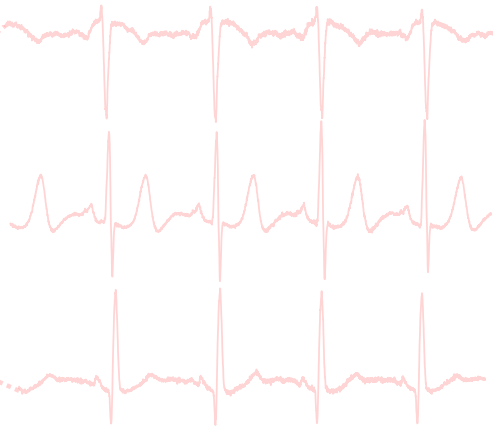
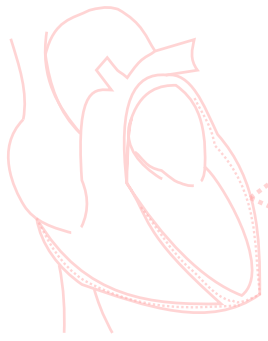


(a)



(b)

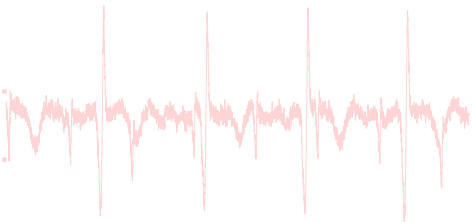
Figure 5.17: Bland-Altman analysis regarding the E/A ratio.



Chapter 6

Non-invasive fECG extraction

This chapter focuses on the signal processing techniques for extracting the fetal ECG. Among the different techniques proposed in the scientific literature, we systematically analyzed the single- and multi-reference implementations of the adaptive filters. Moreover, different wavelet-based post-processing approaches for the denoising of the fECG were evaluated. Last, a germinal work on the fetal ECG quality assessment on raw recordings is presented.



6.1 Rationale

Several techniques for fECG extraction from non-invasive recordings have been investigated over the past decades. [173] Even though the superior performance of blind source separation techniques compared to adaptive filters was demonstrated for this specific problem [229], the latter can overcome the intrinsic limitations of the former, since the latter requires a large number of channels (greater than eight, overall [139]). Then, considering that the reduction in the number of electrodes to be applied on the maternal body is one of the constraints of this specific application, required in particular for unobtrusive wearable systems, adaptive filters can still be considered valuable techniques. Moreover, they can be naturally implemented in real-time, which is not the case of several excellent blind source separation methods, with some exceptions (e.g. [46, 151]).

The dark side of adaptive filtering with a reduced number of leads (in principle one thoracic and one abdominal) is the strong dependency of the output quality from the electrode placement, since a reference mECG lead, morphologically similar to the mECG projection contaminating the fECG in the abdominal leads, is required. This problem could be solved by using multiple non-coplanar thoracic leads, to be able to roughly reconstruct the mECG morphology in any abdominal lead. The multi-reference approach was investigated by using different adaptive filtering methods [161] but an in-depth methodological analysis is still missing to answer the following important questions: is it worth using multiple mECG reference leads rather than a single one, when dealing with real non-invasive fECG recordings? Or, alternatively, to what extent a single-reference adaptive filter can provide an adequate mECG attenuation, at least on abdominal leads parallel to the reference one? When only the fHR is pursued, is that possible to adopt the single-reference approach? The answer to these questions is relevant for the conscious selection of the right technique for a given problem.

To answer such questions, in the first study presented in this chapter, we analyzed the performance of a prototypical multi-reference (MR) adaptive filter, the QR-decomposition with back-substitution recursive least-squares (QRD-RLS), chosen for its numerical stability and good performance. It was compared

to its single-reference (SR) variant, by cancelling the mECG on abdominal leads differently oriented in space. The assessment was performed on a large dataset composed of real recordings and synthetic signals generated by the FECGSYN toolbox. [12, 21] These datasets enabled an in-depth analysis of the results, by subverting some common-sense beliefs on SR adaptive filters in this specific application.

The output of the best performing MR QRD-RLS algorithm seems to suffer from residual noise, so that, in this chapter, the second study involves different WD approaches for the enhancement of fECG traces extracted from non-invasive recordings. To this aim, the result of the application of the QRD-RLS adaptive filter is used as the benchmark.

All processed signals were denoised using a decomposition with the stationary wavelet transform (SWT) and the stationary wavelet packet transform (SWPT), with different deepness of the decomposition. The impact of three different thresholds taken from the scientific literature was assessed, either level-independent [54, 55] or level-dependent [76]. In order to test such thresholds also in case of SWPT, the level-dependency definition of [76] was adapted to the different definitions of the sub-bands.

Nowadays, the challenge is also to accomplish the requirements of the wearable and unobtrusive monitoring systems. One of the main constraints is the low-power feature. In order to save power in a home-monitoring system, enabling to process less channels as possible would be an huge step forward this requirement. The ability to recognize the channels that are more informative, in terms of fetal ECG components, would be a great advantage in the development of a fetal wearable monitoring system.

The third work presented in this chapter is a preliminary study on the classification of the quality assessment of the raw abdominal channels, in order to select the recordings that are characterized by the most-informative components.

6.2 Background

Among the different methods proposed in the scientific literature, adaptive filters have been proposed by several authors exploiting different algorithms [22, 99, 129, 159, 161, 181, 224]. Originally, the approach was introduced in [224], where the adaptive filter received four chest ECG inputs to cancel the maternal component from the single abdominal lead.

More recently, an adaptive filtering approach was proposed in the 2013 Physionet/Computing in Cardiology Challenge [187], where the dataset included only four abdominal channels per record.

In [163], the authors cancelled the mECG from four-abdominal-lead recordings by using an adaptive filter that received as references three out of four channels. The filter output was then subtracted from the channel and the filter coefficients were optimized in order to minimize the sum of the squares of this difference. The method adopted to compute the filter coefficients was a Wiener filter-like method.

Behar et al. [22] compared an echo state neural network-based filtering approach to the least mean square (LMS), the recursive least square (RLS) adaptive filter and template subtraction techniques. The former performed slightly better than the others but without statistical significance.

Non-invasive fECG extraction was also investigated using combined methods, for example based on multi-stage adaptive filters [159] or on adaptive filters and wavelet transform [118].

6.3 Materials and Methods

6.3.1 MEGC cancellation by RLS adaptive filter

Generally speaking, an adaptive filter is a self-modifying digital filter that adjusts its coefficients in order to minimize an error function, which is the distance between the reference signal and the output of the adaptive filter [177].

The adaptive filter can be used in different configurations: one of them is the adaptive noise canceler, whose block diagram is presented in figure 6.1, adapted

to the non-invasive fECG extraction problem. Principally, its aim is to extract a clean version of the signal of interest $s(k)$, that is characterized by an additive noise component $n(k)$. The reference signal has to be strongly correlated to $n(k)$ but not to $s(k)$. The adaptive filter adjusts its coefficients in order to obtain an output $y(k)$ that approximates $n(k)$, forcing the error signal $e(k)$ to resemble $s(k)$. Adaptation of the filter coefficients follows a minimization process of a particular cost function. Referring to figure 6.1, where $d(k)$ is the recorded abdominal signal, $x(k)$ is the reference maternal lead, $y(k)$ is the maternal component on abdominal signal reconstructed by the filter, and $e(k)$ is the extracted fECG:

$$d(k) = s(k) + n(k) \quad (6.1)$$

$$x(k) \approx n(k) \quad (6.2)$$

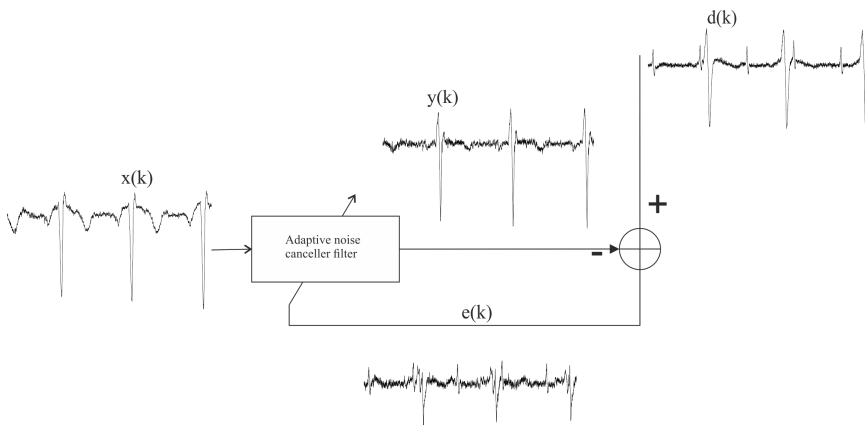


Figure 6.1: Single-reference adaptive filter used as adaptive noise canceller, applied to the non-invasive fECG extraction problem to remove the mECG contribution from the abdominal signals.

$$y(k) = \mathbf{w}^T \mathbf{x}(k) \quad (6.3)$$

$$e(k) \approx s(k) \quad (6.4)$$

From the equations above, we can better understand the use of the adaptive noise canceler applied on the fECG extraction problem. The $d(k)$ represents the combination of the noise and the signal of interest; the maternal lead $x(k)$ approximates the noise, while $y(k)$ is the filter output that is optimized to mimic the maternal component presented in the abdominal lead thanks to the use of reference signal $x(k)$; finally, $e(k)$ is our signal of interests. Compared to other methods, the RLS adaptive filters pay their faster convergence with a higher computational complexity. Moreover, their direct matrix inversion operation may cause numeric stability problems. To mitigate this issue, QRD-RLS filters have been introduced [33], which exhibit both fast convergence and numerical stability. For this reason, the QRD-RLS adaptive filter was chosen as prototypical adaptive filter for this study.

Adaptation of the filter coefficients follows a minimization procedure of a particular objective or cost function. The classical linear Wiener Filter minimises the Mean-Square error (MSE):

$$\xi(k) = E[e^2(k)] = E[|d(k) - y(k)|^2] \quad (6.5)$$

Writing the output signal $y(k)$ as given in Eq. 6.3:

$$\begin{aligned} \xi(k) &= E[|d(k) - \mathbf{w}^T \mathbf{x}(k)|^2] \\ &= E[d^2(k)] - 2\mathbf{w}^T E[d(k)\mathbf{x}(k)] + \mathbf{w}^T E[\mathbf{x}(k)\mathbf{x}^T(k)]\mathbf{w} \\ &= E[d^2(k)] - 2\mathbf{w}^T \mathbf{p} + \mathbf{w}^T \mathbf{R} \mathbf{w} \end{aligned} \quad (6.6)$$

where \mathbf{R} and \mathbf{p} are the input-signal correlation matrix and the cross-correlation vector between the reference signal and the input signal, respectively, and are

defined as:

$$\mathbf{R} = E[\mathbf{x}(k)\mathbf{x}^T(k)] \quad (6.7)$$

$$\mathbf{p} = E[d(k)\mathbf{x}^T(k)]. \quad (6.8)$$

Minimizing the MSE cost function means equating the gradient vector of ξ respect to the adaptive filter coefficient w to zero:

$$\nabla_w \xi(k) = -2\mathbf{p} + 2\mathbf{R}w \quad (6.9)$$

obtaining the so-called Wiener solution w_o that minimizes the MSE cost function:

$$w_o = \mathbf{R}^{-1}\mathbf{p} \quad (6.10)$$

To be able to solve the Wiener solution, R must be non-singular. If the filter length is greater than that required to reduce the error to zero, $R(n)$ will become singular and the RLS filter not well-behaved.

The RLS filter family uses the weighted least-squares (WLS) objective function, which is defined as follows:

$$\xi_D(k) = \sum_{i=0}^k \lambda^{k-1} [d(i) - \mathbf{w}^T \mathbf{x}(i)]^2 = \mathbf{e}^T(k)\mathbf{e}(k) \quad (6.11)$$

The introduction of the forgetting factor λ , which is in the range from 0 to 1, allows to emphasize the most recent error samples in the composition of the cost function, giving to the objective function the ability of modelling non stationary processes.

The RLS re-defines the input-signal correlation matrix R and the cross-correlation vector p introducing the forgetting factor λ :

$$\mathbf{R}(k) = \mathbf{x}(k)\mathbf{x}^T(k) + \lambda\mathbf{R}(k-1) \quad (6.12)$$

$$\mathbf{p}(k) = \mathbf{x}(k)d(k) + \lambda\mathbf{p}(k-1) \quad (6.13)$$

Consequently, the optimum solution takes the form:

$$\mathbf{w}(k) = \mathbf{w}(k-1) + e(k)\mathbf{R}^{-1}(k)\mathbf{x}(k) \quad (6.14)$$

The computation of the inverse matrix of R can be reduced significantly by using the matrix inversion lemma [51]:

$$[\mathbf{A} + \mathbf{BCD}]^{-1} = \mathbf{A}^{-1} - \mathbf{A}^{-1}\mathbf{B}[\mathbf{DA}^{-1}\mathbf{B} + \mathbf{C}^{-1}]^{-1}\mathbf{DA}^{-1} \quad (6.15)$$

obtaining:

$$\mathbf{R}^{-1}(k) = \frac{1}{\lambda} [\mathbf{R}^{-1}(k-1) - \boldsymbol{\kappa}(k)\mathbf{k}^T(k)] \quad (6.16)$$

where:

$$\boldsymbol{\kappa}(k) = \mathbf{R}^{-1}(k)\mathbf{x}(k) \quad (6.17)$$

$$\mathbf{k}(k) = \mathbf{R}^{-1}(k-1)\mathbf{x}(k) \quad (6.18)$$

At each step, the RLS algorithm estimates R and P based on all past data and updates the weight vector using the matrix inversion lemma [51].

The RLS filter does not attempt to solve the wiener solution at each step, that would require the calculation of repeated inverted R matrix, but updates $R^{-1}(k)$ using $R^{-1}(k-1)$, the inverted R matrix of the previous step . The only invertible matrix that is required to be calculated is $R^{-1}(0)$.

Although, the conventional RLS algorithm is fast converging, presents low misadjustment, and is suitable for time-varying environments, its vulnerability is the lack of numerical stability. In fact, the computation of the inverse matrix of R can lead to an ill-conditioned problem.

The convergence rate, the misalignment, and the numerical stability of adaptive algorithms depend on the condition number of the input signal covariance matrix. The higher this condition number, the slower the convergence rate and/or the less the algorithm stability.

QR decomposition

An alternative RLS implementation is based on the QR decomposition, which works on the triangularization of the input data matrix. The QR decomposition is numerically stable and solves the instability problem of the RLS implementation. The matrix $\mathbf{X}(k)$ is $(k+1) \times (N+1)$, where N is the number of filter coefficients, means that its order increases as the iterations progress. The QR-decomposition process applies an orthogonal matrix $\mathbf{Q}(k)$ of order $(k+1) \times (k+1)$ to transform $\mathbf{X}(k)$ into a triangular matrix $\mathbf{U}(k)$ of order $(N+1) \times (N+1)$ such that:

$$\mathbf{Q}(k)\mathbf{X}(k) = \begin{bmatrix} \mathbf{O} \\ \mathbf{U}(k) \end{bmatrix} \quad (6.19)$$

where \mathbf{O} is a null matrix of order $(k-N) \times (k+1)$. Matrix $\mathbf{Q}(k)$ represents the overall triangularization process and may be implemented in different ways as, for instance, the numerically well-conditioned Givens rotations or the Householder transformation [15].

The rotated error $\mathbf{e}_q(k)$ is then expressed as follows:

$$\mathbf{e}_q(k) = \mathbf{Q}(k)\mathbf{e}(k) = \begin{bmatrix} \mathbf{e}_{q1}(k) \\ \mathbf{e}_{q2}(k) \end{bmatrix} = \begin{bmatrix} \mathbf{d}_{q1}(k) \\ \mathbf{d}_{q2}(k) \end{bmatrix} - \begin{bmatrix} \mathbf{O} \\ \mathbf{U}(k) \end{bmatrix} \mathbf{w}(k) \quad (6.20)$$

Due to the property of $\mathbf{Q}(k)$, minimizing $\|\mathbf{e}_q(k)\|^2$ or the cost function $\xi_D(k)$ is equivalent. Therefore, Eq. 6.11 is minimized by choosing the $\mathbf{w}(k)$ in Eq. 6.20 such that $\mathbf{d}_{q2}(k) - \mathbf{U}(k)\mathbf{w}(k) = 0$. [15]

Single and multi-reference QRD-RLS adaptive filter

The theory presented so far was conceived for the single-reference implementation of the QRD-RLS adaptive filter. In a multi-reference implementation, there are multiple reference signals concurring to the definition of the noise (figure 6.2). By calling M the number of channels, that in our case is equal to three as the number of non-coplanar bipolar thoracic leads (x_1 , x_2 and x_3 in figure 6.2),

N_1, N_2, \dots, N_M is the number of taps for each of the M filters. The approach is to shift in a sample from each channel at a time and progress in a recursive manner from the first to the last channel. The filtering routines implemented in this work were provided in [15] and adapted to the problem.

Adaptive filters require to properly tune their parameters to achieve the best compromise between performance and computational cost [22]. In the RLS implementation, there are two important parameters: the forgetting factor λ and the number of taps N . In both implementations, λ was set to 0.999 and N was chosen equal to 20 (for each of the three channels, in the MR implementation). Both these parameters were optimized in a training phase on the real dataset. Remarkably, other studies obtained the same values with similar procedures [22].

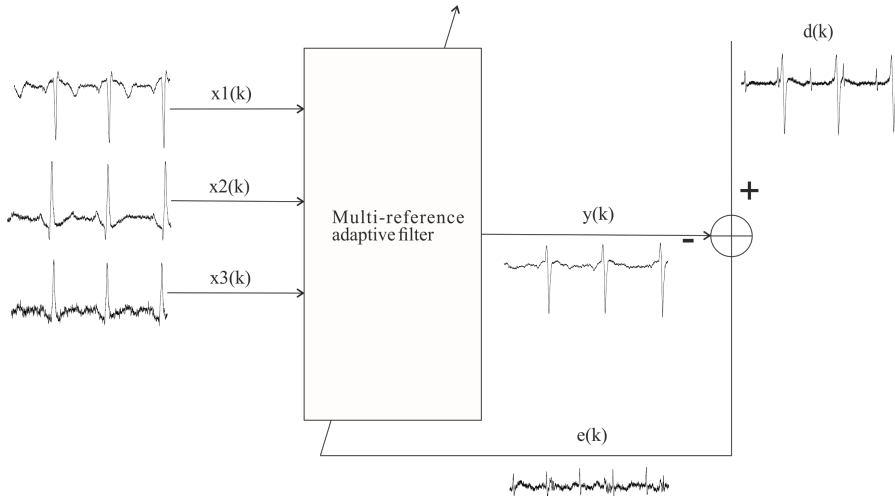


Figure 6.2: Block diagram of the multi-reference QRD-RLS adaptive filter used as adaptive noise canceller, applied to the non-invasive fECG extraction problem to remove the mECG contribution from the abdominal signals.

Signal preprocessing

Baseline wandering, especially when no high-pass filtering is present in the analog signal acquisition chain, as for our real dataset, cannot be tackled by the adaptive filter. In fact, several factors contribute to its generation, from maternal breathing to fetal and cable movements, which have different reflections on different leads, even more on the abdominal ones. Then, a simple preprocessing step is usually recommended before fECG extraction. As already proved in [22], the cut-off frequency of the high pass filter should be higher than the one imposed by the current guidelines, which is 0.67 Hz [108], mainly to compensate such a stronger baseline wandering. In order to preserve the low-frequency components of the ECG, mainly related to P and T and to the ST segments, the signal was high-pass filtered only at 1 Hz, by a bidirectional implementation of a FIR filter of 1124-th order.

6.3.2 Wavelet denoising

WD is a signal processing technique based on the so-called time-scale representation provided by the WT [125, 138]. It is largely used in biomedical signal processing, among the non-linear denoising techniques. [191] Hereafter, a brief introduction to the basic principles of WT and WD is provided.

WT fundamentals

WT is largely used in biomedical signal processing thanks to its good resolution in both time and frequency domains. This feature is particularly useful when dealing with non-stationary signals like the biomedical ones [191]. Moreover, it allows noise removal also when noisy interferences share the same spectral bands of the signal of interest.

In general, WT gives a representation of the signal in a time-frequency domain through a set of coefficients, obtained by means of time-shifted and scaled versions of a specific function or basis ψ , called *mother wavelet*. Mathemati-

cally [110, 125, 138]:

$$WT_f(a, b) = \langle \psi_{(a, b)}, f(t) \rangle = \frac{1}{\sqrt{a}} \int_R \psi^* \left(\frac{t-b}{a} \right) f(t) dt \quad (6.21)$$

where $\psi_{a,b} = \frac{1}{\sqrt{a}} \phi\left(\frac{t-b}{a}\right)$ indicates the shifted and scaled version of ψ , thus the family of wavelets derived by ψ , while a, b represent the scale and the time-shift parameters, respectively. The scale parameter a is associated to a dilatation or contraction of the mother wavelet ψ : the higher its value, the more the mother wavelet is dilated, so lower frequencies representations are involved. On the other hand, the lower the value of a , the more the mother wavelet is stretched and thus the higher frequencies are analysed. [191]

When $a \in R^+$ and $b \in R$, without limitations, we obtain the continuous wavelet transform (CWT), otherwise, in case of discretization of these parameters, we have the discrete wavelet transform (DWT) [138]. The most common discretization of the parameters is the dyadic one, where $a = 2^j$, $b = k \cdot 2^j$, with $j, k \in Z$. DWT decomposition can be implemented by filter banks, including high-pass and low-pass filters whose definition is strictly associated to the mother wavelet and the scaling function [138]. From this perspective, firstly the signal is given as input to the high-pass and low-pass filters and, as such, its frequency band is split in a half; the outputs of this filtering step are known as detail and approximation at the first level, and are associated to the higher and lower half-band respectively. Then the same process is iteratively repeated on the output of the low-pass filter of the previous filtering step until the lowest frequency components, i.e. the approximation of the last level, cover the range between 0 and $\frac{f_n}{2^l}$, where f_n denotes the folding frequency and l the decomposition level.

The most widely used WT type for fECG filtering is the DWT, because it is characterized by a smaller distortion of the QRS complex extremes [130]. Among the different implementations of the DWT, the stationary wavelet transform (SWT) was chosen in this work, since it is characterised by the translation-invariance property [43, 138, 140, 155]. In the light of the results achieved for neural spikes in [37], this property let the denoising results be independent from the QRS occurrence over time.

While only the approximation coefficients are given as input for the subsequent filtering steps in the WT, in the wavelet packet decomposition both detail and approximation are decomposed at each level [138], giving rise to a complete binary tree (see figure 6.3). As such, a finer time-frequency analysis is obtained, since also high-frequency sub-bands are split.

For the same reasons described for the SWT, in this work we used the translation-invariant wavelet packet transform (SWPT) [154, 201].

WD: principles and applications

WD is essentially based on three main steps [138]: in the first one (analysis) the signal is decomposed in a set of wavelet coefficients; then, detail coefficients are compared to threshold (thresholding phase) and those that exceed the threshold are used along with the approximation for the time-domain reconstruction (synthesis).

At each step, different choices can influence the denoising result. For the analysis (and so the synthesis), the mother wavelet and the decomposition level must be chosen before the decomposition is performed. The choice of the mother wavelet really affects the wavelet post-processing output. During a preliminary investigation with different mother wavelets, and also as shown the results in [6], even though Daubechies7 is similar in shape to heart beat wave, the Haar mother wavelet achieved better results (data not shown), so it was selected for this work. About the decomposition level, we performed both the 6-level and the 7-level decompositions on the basis of the frequency contributions of major interest for fECG QRS complexes (8-20 Hz) [41]. In this way, by choosing a 7-level decomposition, we performed WD from 1024 Hz until 8 Hz (because details at level 7, cD7, spread from 8 Hz to 16 Hz), whereas with a 6-level decomposition the limit is 16 Hz (because the last detail, cD6, spans over the 16-32 Hz band).

After the time-scale representation had been obtained, each detail coefficient was compared to a threshold, chosen to be proportional to the amount of

noise, which in turn can be estimated at each level as [54, 55]:

$$\sigma_j = 1.4826 \text{median}(\|cD_j - \hat{cD}_j\|) \quad (6.22)$$

Different thresholding approaches can be implemented, but the most typical ones are the so-called hard-thresholding and soft-thresholding [54, 55], respec-

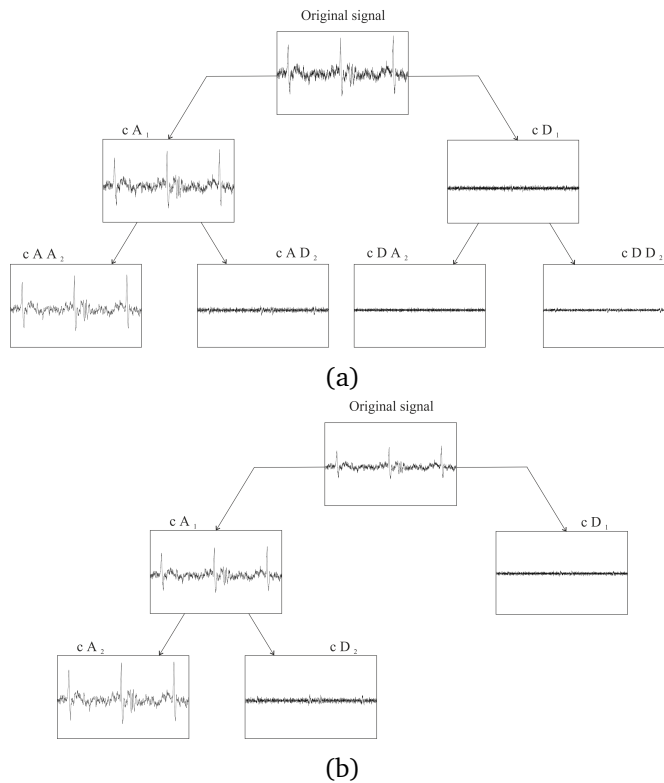


Figure 6.3: Example of SWT and SWPT 2-level decomposition of a real fECG signal. a) in the SWT decomposition, after the first step, only approximations are split. b) in the SWPT, both approximations and details are decomposed.

tively defined as:

$$\overline{cD_{j,k}} = \begin{cases} \text{sign}(cD_{j,k}) & |cD_{j,k}| \geq 0_j \\ 0 & \text{otherwise} \end{cases} \quad (6.23)$$

$$\overline{cD_{j,k}} = \begin{cases} cD_{j,k} & |cD_{j,k}| \geq 0_j \\ 0 & \text{otherwise} \end{cases} \quad (6.24)$$

where $cD_{j,k}$ is the k -th detail coefficient at level j and 0_j is the threshold value calculated for the same level.

In this work, in order to avoid the shrinkage effect due to subtraction of 0_j in the soft-thresholding, Eq. 6.24, we choose the hard-thresholding and tested three different thresholds from the literature.

At first, the Universal, Eq. 6.25, and the Minimax, Eq. 6.26, thresholds [54, 55], were selected because of their widespread adoption.

$$0_j = \sigma_j \sqrt{2 \ln(N)} \quad (6.25)$$

$$0_j = \sigma_j (0.3936 + 0.1829 \log_2(N)) \quad (6.26)$$

Both thresholds depend on the signal length N . Moreover, since at higher frequencies we assumed the predominant presence of noise whereas at lower frequencies we expected a more significant signal content, we also tested another threshold proposed in [76], defined in Eq. 6.27.

$$0_j = \begin{cases} \sigma_j \sqrt{2 \ln(N)} & j = 1 \\ \sigma_j \sqrt{2 \ln(N)} / \ln(j+1) & 1 < j < L \\ \sigma_j \sqrt{2 \ln(N)} / \sqrt{j} & j = L \end{cases} \quad (6.27)$$

In each of these cases, σ_j was evaluated on a part of the signal presenting only noise. If on simulated abdominal fECG signals, it is simply possible to

consider as noise each interval between two fetal QRSs, since the mECG is not present and fetal P and T waves are of very low amplitude, on real abdominal signals the possible presence of residual maternal fECG components after the fECG extraction methods have been applied imposes a more careful approach. In this case, a part of the signal that can be considered as only noise could be identified between the beginning of the P waves and the end of the previous T waves, delineated in a synchronised reference mECG signal by using the algorithm presented in [131]. Such signal segments were excluded in presence of a fetal QRS in that interval.

WD with wavelet packet decomposition Even though the application of the different thresholds is straightforward on the DWT, the transposition to the SWPT is direct only for the Minimax and the Universal thresholds, by simply evaluating σ_j at each detail node.

However, for the other threshold proposed in [76], since the scaling factor is defined as level-dependent, a different approach was chosen. Specifically, besides the same evaluation for σ_j , we tested different adaptation approaches.

Statistical analysis performed on real dataset, in order to identify the best SWPT adaptation for the Han et al. threshold [76], did not reveal any significant difference among the three proposed approaches. Therefore, since on the basis of the achieved results (data not shown) the linear interpolation adaptation of the scaling factor seemed a better trade-off, it was chosen for the analysis. In fact, considering the cubic interpolation, it showed an equivalent behaviour, thus the linear adaptation was preferred because of its lower complexity.

6.3.3 Signal Quality Assessment

Features

Different features have been introduced and used in literature, as illustrated in section 3.1.6.

In this study, the features have been computed in the raw multi-channel recordings.

Among the features already presented in section 3.1.6, several features have been implemented for this purpose, shown in table 6.1. All features were computed over 10-second long segments.

The maternal R peaks have been detected using the P&T algorithm [149], while for the fetal ones the *jqrs* algorithm [23] has been used. In order to be able to detect the fetal QRS complexes, the algorithm takes as input the raw channel where the maternal ECG has been blanked by subtracting averaged maternal beat from the detected maternal beat windows. Only the features related directly (App_f , SNR, SIR, see table 6.1) and indirectly (number of R-peaks, mean QRS area, median QRS area, std QRS area, rSQI, cSQI, xSQI, mean QRS area, median QRS area, std QRS area, see table 6.1) to the fetal beats have been computed on the above-described signal.

Index	Explanation
stdSQI	it is the standard deviation of the signal, it measures the variation of the amplitude.
sSQI	it is the skewness of the signal, it represents the dataset symmetry. If the symmetry is perfect, the skewness is 0. We expect the ECG to be highly skewed due to the QRS complex. Given the nature of the noise, the distribution is approximately symmetric, yielding a low skewness value. Therefore, skewness is less robust to noise than kurtosis. [232]
kSQI	it is the forth moment of signal or kurtosis. For a standard, noise-free and normal sinus ECG, the value is less than 5 [81]. If power-line frequency interference, baseline drift or Gaussian distribution of random noise is noted, the values is less than 5 [39]. If EMG interference is present, the value is around 5 [81]. Low kSQI usually indicates low frequency noise such as baseline wander, Gaussian noise and high frequency sinusoidal noise (power-line interference). [232]
pSQI	it represents the relative power in the <i>fqrs</i> complex.
basSQI	it is the relative power of baseline.
pband1	bandpower [0.05,0.5]
pband2	bandpower [0.5,10]
pband3	bandpower [10,20]
pband4	bandpower [20,48]
pband5	bandpower [48,52]
pband6	bandpower [52,100]
seSQI	it is a measure of its spectral power distribution.
std baseline	it is the standard deviation of the extracted baseline.
App_f	Amplitude peak to peak of the fetal R-peaks, detected using the <i>jqrs</i> peak detector [23] on the raw signal where the maternal beat-windows were removed. It has been computed on the mean fetal beat.
App_m	Amplitude peak to peak of the maternal R-peaks, detected using the P&T algorithm on the raw channels. It has been computed on the mean maternal beat.
SIR	The signal-to-interference ratio considering the fECG the signal of interest, and the mECG the interference. It exploits the fetal and maternal mean beats.
SNR	The signal-to-noise ratio of the fECG, computed on the raw channel without the maternal ECG components.
number of R-peaks	
mean HR	
median RR interval	
std RR interval	
rSQI	it represents percentage of intervals inside a confidence interval, assessing regularity in term of HR.
cSQI	it computes the median correlation coefficient between a template beat and each individual beat on the signal.

xSQI	it attempts to describe how different a QRS complex is from its surrounding signal.
mean QRS area	
median QRS area	
std QRS area	
Complexity	it computes the ratio of the mobility of the first derivative of the signals to the mobility of the signal itself. The mobility is defined as the square root of the ratio between the variances of the first derivative and the amplitude. The ratio will be dependent on the curve shape only. It is dimensionless. The minimum value is the unity, the parameter will quantify any deviation from the sine shape as increase from unity. [84]
HA	it is the highest amplitude in the recording.
LA	it is the lowest amplitude in the recording.
ss	it represents the steepest slope in the recording.

Table 6.1: Computed signal quality features.

Classification problem

The SVM [215] was used for the signal quality assessment classification. Therefore, the classification problem has a binary output: 0 for low quality raw fetal ECG recordings and 1 for good quality acquisitions. The use of the SVM was introduced in this work because of its capability to solve non-linearly separable classification problems by the adoption of non-linear kernels. It achieved very higher performance compared to other classifiers (data not shown).

The SVM was applied using a Gaussian radial basis function kernel, $\nu = 0.5$, and box constraint set to 1.

Features Selection

Feature selection reduces the dimensionality of data by selecting only a subset of optimal features that can model the real output. The main benefits of feature selection are to improve prediction performance, provide faster and more cost-effective predictors, and provide a better understanding of the data generation process [74]. Using too many features can degrade prediction performance even when all features are relevant and contain information about the response variable.

In this work, the features were selected by using the sequential features selection, which sequentially identifies the best features using a custom criterion until there is no more improvement.

6.3.4 Adopted Dataset

Different datasets have been used for the three studies. In this section, a detailed description of these datasets is given.

Testing Datasets for the SR and MR adaptive filters study

In order to perform the analyses required for the comparison of the SR and MR QRD-RLS adaptive filters, custom datasets were adopted.

Real dataset The real dataset is composed of biopotentials acquired from healthy pregnant women. Along with the electrophysiological signals, a simultaneous cardiac pulsed-wave Doppler (PWD) trace was recorded. In the context of this work, it played the main role of providing the ground truth for the fetal heart activity, from a mechanical perspective, which was important to confirm the presence of fetal QRS complexes. PWD and biopotentials are acquired as already explained in chapter 4.

Figure 6.4 shows the positioning of the electrodes on the maternal body exploited in this study. The chosen configuration includes six electrodes for three bipolar channels, capturing three non-coplanar maternal leads on her chest, and three abdominal electrodes, required to digitally obtain three abdominal bipolar leads and a unipolar one. A ground electrode was placed on the right hip. Figure 6.5 shows a sample trace acquired with this setup.

Figure 6.6 shows an example of simultaneous recording of PWD and electrophysiological signals.

The dataset included 28 multi-channel signals from 20 healthy pregnant women, for a total of 112 abdominal channels leading to as much non-invasive fECG signals.

Synthetic dataset The FECGSYN tool [12, 21] is a reference open-source platform for non-invasive fetal electrocardiography research. It has already been illustrated in section 3.1.2.

In this work, fECG mixtures were generated at 2048 Hz, with a duration of 10 s. Motion artifacts, electrode movements and baseline wandering were

realistically added to the clean signals. The position of the electrodes was simulated as shown in figure 6.7, which was the reference positioning also for the real recordings, while in figure 6.8 there is an example of synthetic signals, generated specifically for this purpose. Cardiac and noise signals were calibrated with respect to the maternal signal, choosing the SNR of the fECG relative to the mECG (SNR_{fm}), in this work set at -18 dB, and the SNR of the mECG relative to noise (SNR_{mn}). Five SNR_{mn} were reproduced (3, 5, 9, 12 and 15 dB). The maternal and fetal HR were assumed to be fixed, at respectively 90 bpm and 150 bpm. Twenty slightly-different fetal heart positions were simulated for each SNR_{mn} . One hundred virtual subjects were created.

Channels combination Considering the synthetic data, each trace includes four abdominal signals, which are the horizontal (1-2, figure 6.7), vertical (1-3, figure 6.7) and oblique (1-4, figure 6.7) leads and a unipolar channel (4, see figure 6.7), for a total of four hundreds abdominal synthetic signals. For each of them, three no-coplanar thoracic lead (5-6, 5-7, 7-8, figure 6.7) were also created. For the specific application, the first thoracic lead (1m in figure 6.4 for the real dataset and 5-6 in figure 6.7 for the synthetic one), which is perpendicular to the sagittal plane, were chosen to be the input reference for

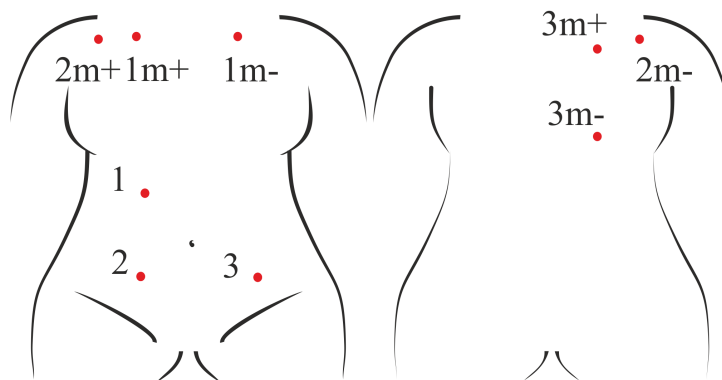


Figure 6.4: Electrodes positioning: the m channels are the bipolar maternal leads, while on the abdomen there are the unipolar ones.

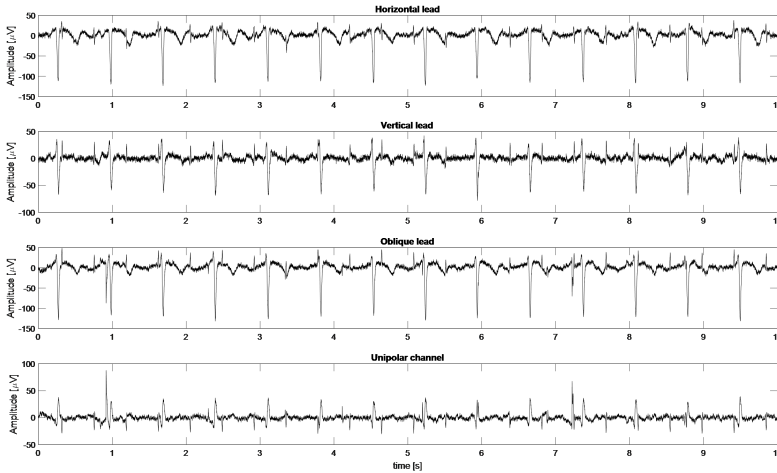


Figure 6.5: A sample signal from the real dataset.

the SR technique, whereas all the three thoracic leads (1m, 2m, 3m in figure 6.4 for the real dataset and 5-6,5-7 and 7-8, in figure 6.7 for the synthetic one) were used for the MR version.

Testing datasets for the WD post-processing study

In the next two paragraphs the real and the synthetic datasets used in this study are described. Moreover, figure 6.9 shows some example traces for both datasets.

Real dataset The biopotentials were recorded as already described in chapter 4. Regarding the electrode configuration, it includes six electrodes for three bipolar channels, capturing three non-coplanar maternal leads on her chest, and twenty-four abdominal electrodes on the maternal abdomen. Only four unipolar recordings are then used to digitally obtain two abdominal bipolar leads.

All the leads were preprocessed using a high-pass equiripple FIR filter, with

cut-off frequency of 1 Hz, and then the mECG was removed using the QRD-RLS adaptive filter, as previously described.

Furthermore, the processed signals are still characterized by some low-frequency components, which come from the maternal ECG, that cannot be tackled by the adaptive filter. For this reason, prior to the application of the WD, a method for the baseline extraction, exploiting a single stage of a moving average window (length set to 512 samples long), was used in order to remove the drift due to these low-frequency components from the processed fECG signals. This method was selected because it exhibits the best performance results for this purpose.

The dataset included 21 2-channels fECG signals, extracted from non-invasive recordings from 21 healthy pregnant women.

Synthetic dataset In this study, fECG mixtures were generated at 2048 Hz, compatible with the real dataset, with a duration of 10 s. The electrodes were

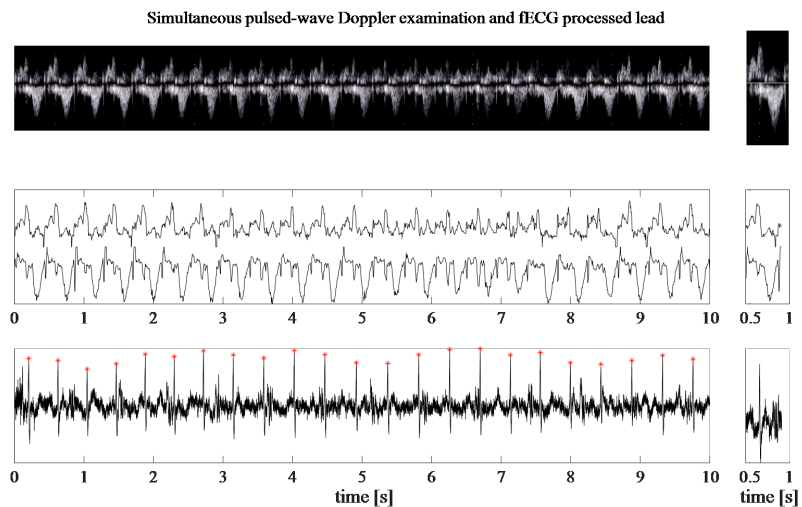


Figure 6.6: A sample recording from the real dataset.

placed in a custom position, and a single position was also considered for the fetal heart throughout the dataset. Even though the mECG is not used in the processing, in order to simulate the synthetic data, the settings have to consider the maternal component, so that the SNR_{fm} is set at -18 dB. Regarding the SNR_{mn} , forty linearly spaced values between 3 dB and 15 dB were reproduced. The maternal and fetal heart rate were assumed to be fixed, at respectively 90 bpm and 150 bpm. Forty virtual subjects were created, each one including two unipolar abdominal signals, digitally combined to obtain a horizontal lead on the abdomen. Even though three realistic noise sources (i.e. muscular artefacts, baseline wander and electrode movements) can be added with the simulator, they are not representative of an extracted fECG trace. For this reason, white and pink noises were added to the traces, with amplitudes chosen according to the SNR previously used for the toolbox settings. An example of the abdominal

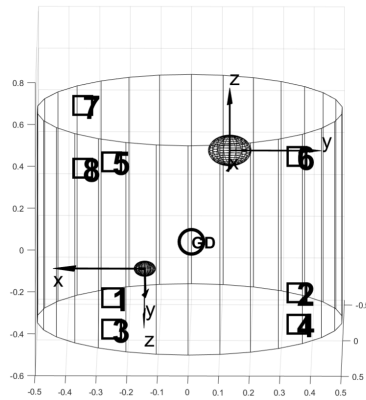


Figure 6.7: Graphical representation illustrating the locations of the maternal heart (upper circle) and the fetal heart (lower circle). Squared boxes, located on the maternal abdomen, indicate electrode positions and are numbered for the corresponding output channel. The referenced electrode is labelled as GD (middle circle).

lead for three synthetic subjects is shown in figure 6.9b.

Testing dataset for the Signal Quality Assessment

A total of 174 real fetal ECG recordings, composed of 24 abdominal channels, acquired from 55 pregnant women, have been used for this analysis. The dataset was acquired as described in chapter 4, with different recording electrode positions. The lengths are variables, but a total of 527 minutes of recordings has been used in this work.

Data Labelling Because the aim is to identify the raw channels that will lead to a good quality processed fetal ECG, the labels were attributed using the processed channels. Each raw signal was first processed by the algorithm used in [61], and then the SNR was computed on the mean beat extracted from the algorithm. Depending on the SNR value, a binary labelling was applied to

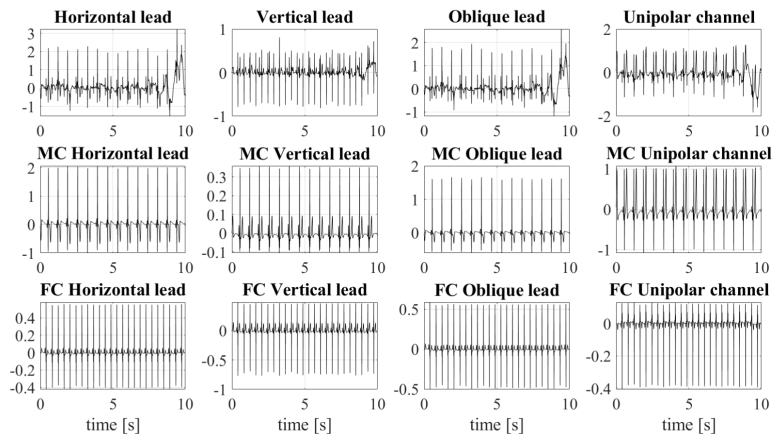
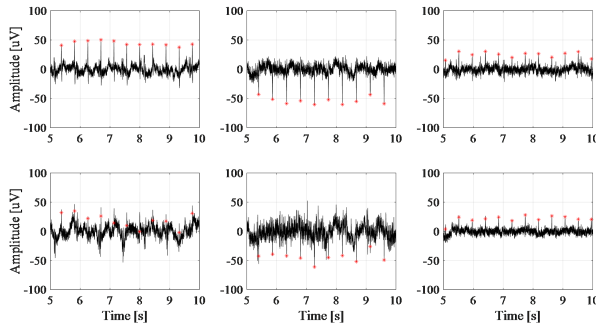


Figure 6.8: The first row represents the simulated signals, respectively the horizontal, vertical, oblique and unipolar channels, while the others, labelled as MC and FC, represent the associated mECG and fECG components.

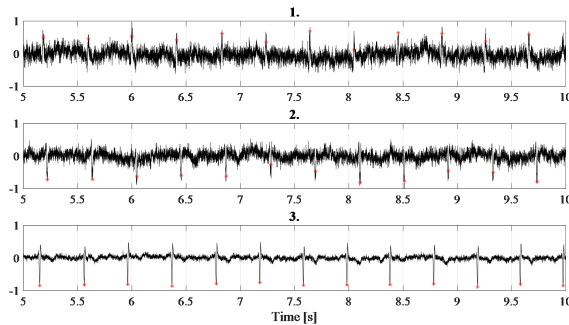
the equivalent unprocessed channel, so that the signals characterized by a SNR higher than 15 dB were labelled as 1, otherwise 0.

6.4 Comparative analysis methods

In principle, the availability of three non-coplanar leads for the mECG should enable the projection of the maternal heart vector in any lead direction. Obviously, by providing more information on the maternal heart vector than a single



(a) Real dataset: six traces recorded from three different subjects.



(b) Synthetic traces with different SNR: a1. 3.3 dB, a2. 6.38 dB, a3. 15 dB.

Figure 6.9: Example of the two datasets.

projection on a given direction, the MR QRD-RLS filter should outperform its SR counterpart. However, a proper selection of the abdominal lead parallel to the maternal chest lead used as reference could be thought to produce acceptable results, at least when only the fHR computation is pursued. Since the reduction of the number of processing leads is important in the context of several applications, especially for wearable monitoring systems, this assumption should be carefully verified.

Because we focus on the evaluation of the maternal component removal, in order to perform such an analysis, the following metrics were adopted:

- The signal-to-interference ratio (SIR), more appropriate the SNR when the noise is a well-defined interference superimposed to the signal of interest
- The mECG attenuation after adaptive filtering, to be able to better quantify how much the maternal ECG was removed from the abdominal leads
- Fetal QRS peak detection accuracy, since fHR is the simplest parameter that can be extracted from fECG.

The SIR is commonly used to analyze the power in both the enhanced and the rejected signal sources, for example when blind source separation algorithms are benchmarked [99]. Since in this case the signal of interest was the fECG whereas the interference was the mECG, the SIR was computed as:

$$SIR_{dB} = 20 \cdot \log_{10} \left(\frac{App_f}{App_m} \right) \quad (6.28)$$

where App_m is the peak-to-peak amplitude of the maternal average QRS complex, and App_f is the peak-to-peak amplitude of the average fetal QRS complex. Since the adaptive filter with thoracic references aims at removing from the abdominal leads primarily the maternal ECG interference, the SIR parameter effectively quantifies this cancellation process more than other performance metrics. In Eq. 6.28, the peak-to-peak amplitudes were computed

on the average QRS complex for both the fECG and mECG, because the local variability due to noise and small movements influence this computation. The fetal QRS complexes were annotated with the help of the simultaneous PWD signal, whereas the maternal QRS detection was performed by using the Pan-Tompkins algorithm [149] on the horizontal chest lead.

In order to have a significant SIR, QRS averaging was performed only between complexes exhibiting a maximum of the cross-correlation, based on the Pearson's correlation coefficient, above a given threshold, empirically chosen to be equal to 0.6 to take into account the presence of the noise.

The window length for the fetal QRS complex template was set to 40 ms, as shown in [203], whereas the window length for the maternal QRS complex was set to 100 ms [197]. If less than four QRS complexes were recognized as similar on the output signal, based on their cross-correlation values, that signal (either fECG or mECG) could be treated as non-deterministic. In such an event, in Eq. 6.28, the App peak-to-peak amplitude of the signal is substituted by four times its standard deviation, thus treating the signal as non-deterministic. Regarding the mECG, this situation is caused by its adequate suppression, whereas, for the fECG, it is due to the fact that fECG was not detectable on that lead.

Because of its definition, SIR is influenced by the amplitude of the signal and the interference. The fECG amplitude depends on the fetal presentation, the development stage and the composition of the fetomaternal compartment tissues. For these reasons, the SIR was computed also on the raw signal, in order to evaluate the performance of the SR and MR techniques by comparing the SIR values before and after the adaptive filter application. Remarkably, a high SIR implies a good mECG cancellation from the abdominal recordings, whereas a low SIR represents a trace where the mECG power is still high, meaning that the maternal amplitudes are still significant in the processed signal with respect to the fECG. To enable the quantification of the mECG removal, regardless of the fECG amplitude, the attenuation of the mECG was also computed, as:

$$Attenuation = -20 \cdot \log_{10} \left(\frac{App_{out}}{App_{in}} \right) \quad (6.29)$$

where App_{out} is the peak-to-peak amplitude of the average maternal QRS complex in the processed abdominal signal, and App_{in} is the peak-to-peak

amplitude of the average maternal QRS complexes in the original (unprocessed) abdominal lead. Moreover, the SIR is intrinsically influenced by both the fetal and the maternal QRS amplitudes. To decouple these aspects, both the fetal and maternal QRS amplitude (in the original abdominal leads and in their SR and MR processed leads) were evaluated and reported.

Finally, the j_{QRS} fetal QRS detector [23] was used on all the processed abdominal leads to obtain the fHR. The algorithm consists of a window-based peak energy detector, based on an adaptive thresholding as well as forward and backward search. It was chosen among the fetal QRS detectors available in the scientific literature because, in the training phase, it performed better than others on fECG traces with very low SNR. The accuracy (Acc) of the peak detector over all the signals was computed as:

$$Acc = \frac{TP + TN}{TP + TN + FP + FN} \cdot 100 \quad (6.30)$$

where TP is the number of true positive detections, TN is the number of true negatives, FP is the number of false positives and FN that of false negatives.

In order to represent the computed metrics providing some hints on the actual shape of their distribution, the box-and-whiskers plot was chosen.

Furthermore, statistical analysis was performed to investigate the significance of the differences observed between the SR and MR results in terms of SIR, mECG attenuation and fetal QRS detector accuracy. The significance was investigated by considering the different abdominal leads separately. First, the normality of the distributions was checked by using the Lilliefors test. The negative result of this test imposed the adoption of a non-parametric statistical test to study the significance of the results. In particular, the Wilcoxon signed rank test was chosen.

The results of the different WD approaches described above were systematically analysed by exploiting the following metrics:

- SNR
- Fetal QRS detection accuracy (Acc)

- Fetal QRS detection true positive rate (TPR, or Sensitivity)

Regarding the synthetic dataset, it was possible to compute also these following parameters:

- Root mean square error (RMSE)
- Pearson's correlation coefficient (ρ)
- Spearman's correlation coefficient (r_s)
- The mean value of correlation coefficient between each QRS complex of a signal and the associated average QRS template (cSQI).

The SNR is widely used to evaluate the quality of the trace, in terms of the power in both the signal of interests and the noise sources. The SNR was computed as:

$$SNR_{dB} = 20 \cdot \log_{10} \left(\frac{App_f}{4\sigma} \right) \quad (6.31)$$

where App_f is the peak-to-peak amplitude of the fECG and σ is the standard deviation of the noise for that signal. The peak-to-peak amplitude was computed on the average QRS complex for a given signal, because the local variability due to noise and small movements strongly affects this index. QRS averaging involved only those complexes exhibiting a maximum of the cross-correlation among them, based on the Pearson's correlation coefficient, above a given threshold, empirically chosen to be equal to 0.6 to take into account the presence of the noise and residual mECG. The window length for the fetal QRS complex template was set to 40 ms, as in [203].

The fetal QRS complexes were annotated with the help of the simultaneous PWD signal. The jqrs fetal QRS peak detector [23] was used on all the processed abdominal leads to obtain the fetal heart rate. The accuracy of the peak detector over all the signals was computed as in Eq. 6.30, while the TPR:

$$TPR = \frac{TP}{TP + FN} \cdot 100 \quad (6.32)$$

All these quality indices are important on real recordings, since the ground truth is not available, i.e. the actual fECG waveform morphology is unknown. In order to assess the performance by exploiting more precise indices able to quantify the distortion introduced by the WD methods, the adoption of simulated data was then required. On them, the RMSE, the Pearson's and the Spearman's correlation coefficients and the cSQI were evaluated between each post-processed simulated signal and the corresponding noiseless fECG signal. Considering an interval of 300 ms around each fetal R wave, 120 ms before and 180 ms after, Pearson's and Spearman's correlation coefficients and RMSE values for each beat of the specific signal were estimated. Then, their median values for each denoised signal were used as measures of the morphological preservation.

Moreover, regarding the average correlation coefficient cSQI, it was already used in [147] to classify as distorted those signals in which cSQI was lower than a pre-defined threshold, and well-preserved those presenting a value of cSQI higher than that. Another work [120] assessed the morphology consistency of any two ECG beats (with P, T and QRS) within a fixed time frame by using the correlation matrix constructed as the correlation coefficient between the i -th and the j -th beat. The latest review on the signal quality assessment for ECG [176] showed as the median correlation cSQI is also used to cluster the beat shape, and proved that the correlations to averaged beat, intra-lead and inter-lead, are commonly used as signal quality estimators for ECG recordings.

In this work, we used the intra-lead correlation, the cSQI, as a morphology conformity measure for the synthetic fECG, by using a window including 120 ms before and 180 ms after the fetal R peak, as in [203].

Finally, a statistical analysis was performed to investigate:

- i the significance of the differences in metrics between before and after wavelet-based post-processing conditions, respectively for decomposition levels equal to 6 and 7,
- ii the threshold being equal, the significance between SWT and SWPT implementation, respectively for decomposition levels equal to 6 and 7,
- iii the difference between SWT and SWPT but considering all the possible

thresholds, respectively for decomposition levels equal to 6 and 7,

- iv the best WD approach for each decomposition level,
- v the final comparison trying to identify the best decomposition level, both considering SWP and SWPT implementations as separated and merged distributions.

First, the normality of the distributions was checked by using the Lilliefors test. If a result did not satisfy the assumption of normal distribution, a non-parametric statistical test was adopted. In particular, we used the Kruskal–Wallis test for comparisons involving more than two distributions, and the Wilcoxon test was selected when comparing only two distributions. When the results of the Lilliefors test did not reject the assumption of non-normal distribution, we adopted the one-way ANOVA, instead of the Kruskal-Wallis test, and the Student's t-test, instead of Wilcoxon test.

In all the statistical tests, we considered 'statistical significance' to be $p < 0.05$.

Regarding the signal quality assessment, to maximize contrast and create a balanced database [232], a 40-fold cross-validation method was used 10 times to reduce the generalization error in the training set.

6.5 Results

Regarding the SR and MR adaptive filters study, in the following figure 6.10, figure 6.11, figure 6.12, and table 6.2, the results were grouped for the original (raw, OR) abdominal channels (i.e. the unfiltered ones), SR and MR processed leads, respectively for the horizontal (hor), vertical (ver), oblique (obl) and unipolar (unip) abdominal leads. In the following figures, the distributions of the results were shown as a boxplot, in order to have a visual idea of the results, while the tables showed the median and the standard deviation values of all the distribution.

At first, we will focus on the comparison between the SR and MR methods, then we focus on the comparison of the different leads.

Figure 6.10 represents the overall results for the real dataset. It can be observed that the SIR values always revealed an improvement with respect to the raw signal, regardless of the channel and the chosen approach, but the MR adaptive filter significantly outperforms the SR one ($p < 0.0009$). Remarkably, this significantly poor performance of the SR implementation was confirmed also when the horizontal abdominal lead was considered, even though the reference and processed leads are parallel. Similar results for the SIR are shown in figure 6.11 for the synthetic dataset ($p < 0.0002$). By evaluating the mECG attenuation, it was possible to see how the MR approach significantly outperforms the SR implementation again ($p < 0.0001$), whichever the lead.

Figure 6.10 and figure 6.11 also present the fetal and maternal QRS amplitude, respectively for the real and the synthetic datasets. It is clearly noticeable a reduction in the values of these two parameters after the adaptive filtering. Since the reference signals were not correlated with the fECG, because they were acquired on the upper part of the chest, the fECG attenuation can only be ascribed to both the frequency behavior of the filter and to a rough estimation of the fetal QRS amplitude on the original abdominal leads due to the larger maternal contributions. Moreover, the results on the fetal QRS amplitude reveal how the adoption of a differential measurement in real recordings helped increasing the fECG amplitude compared to a unipolar lead (figure 6.10). In fact, the OR fetal amplitudes' median values of horizontal and oblique leads are statistically significantly higher than the one related to the unipolar channel ($p = 0.004$, $p = 0.001$ respectively). This was also observed in [128], along with a reduction of the common-mode interference. The opposite behavior achieved on the synthetic dataset (figure 6.11) could lead to wrong conclusions. In fact, on synthetic signals, the differential measurements generate reduced signals of both the fetal and the maternal ECG. This can be seen in figure 6.14, where there is an example of the output synthetic signals.

Moreover, by looking at the SIR on the raw (OR) synthetic signals, it is clearly visible the lower values of the bipolar leads compared to the unipolar channel. Furthermore, both the fECG and the mECG are overall significantly smaller on the vertical lead; this is also visible in figure 6.8. Moreover, it also

happened that the maternal amplitude was lower than the fECG amplitude, even though for the generation of the unipolar channels (from which the differential measurements were taken) the SNR_{fm} was set at -18 dB, in order to decrease this effect. In the real dataset, this never happens, thus suggesting being careful in using such a synthetic dataset for the performance analysis of a fECG extraction algorithm.

Finally, on the real dataset, the accuracy of the fetal QRS detection (figure 6.12, left) is significantly higher for the MR version of the adaptive filter with respect to the SR one ($p < 0.004$). Moreover, the accuracy of the fetal QRS detection performed on the SR output reveals how this approach is not always trustable, and strongly depends on the fECG amplitude. However, the difference between the two techniques (MR and SR) vanishes on the synthetic dataset (figure 6.12, right, $p < 0.8$), because of the easiest detectability of the synthetic fetal QRS on such signals, which is far from a real scenario.

To summarize the previous findings, the results of the statistical analysis

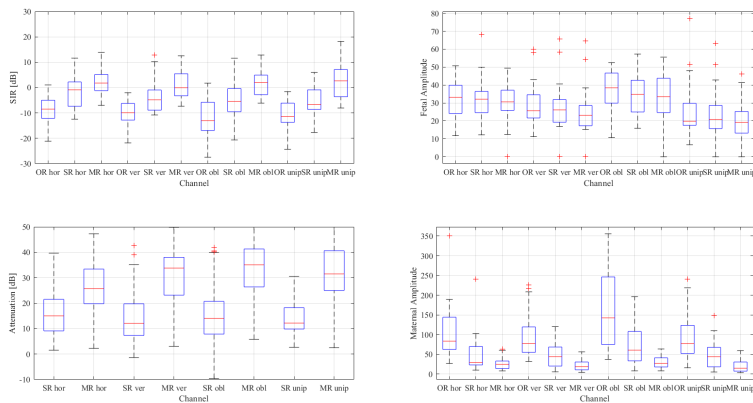


Figure 6.10: Results on the real dataset. OR: original raw abdominal lead, SR: single-reference method, MR: multi-reference method, hor: horizontal lead, ver: vertical lead, obl: oblique lead, unip: unipolar channel.

by the Wilcoxon test aimed at comparing the MR and SR adaptive filters in terms of SIR, maternal attenuation and fetal QRS detection results on the

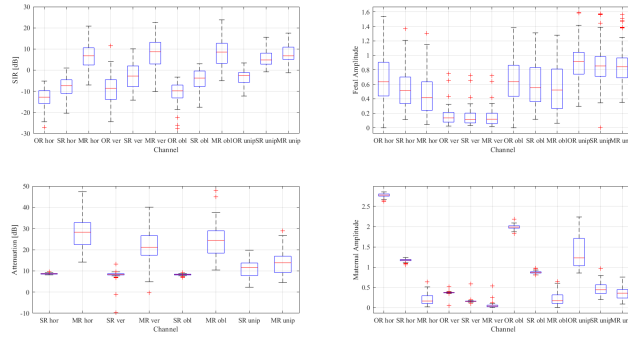


Figure 6.11: Results on the synthetic dataset. OR: original raw abdominal lead, SR: single-reference method, MR: multi-reference method, hor: horizontal lead, ver: vertical lead, obl: oblique lead, unip: unipolar channel.

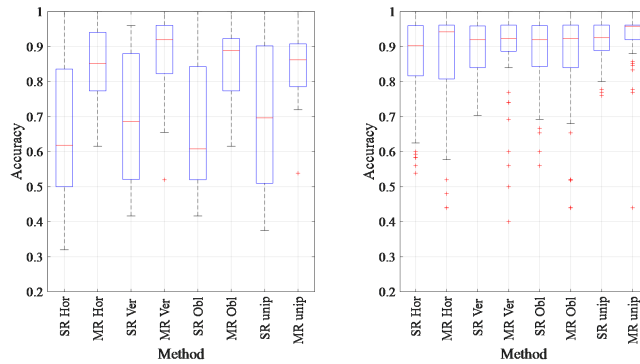


Figure 6.12: Accuracy of the fetal QRS detector applied on the output signals from SR and MR QRD-RSL algorithms, for real (left) and synthetic (right) datasets.

Table 6.2: Real and Synthetic dataset results: median values (first quartile third quartile)

Real dataset results	SIR [dB]	Fetal Amp [uV]	matAmp [uV]	matAtt [dB]	QRSdetAcc
OR hor	-8.5(-12.09 -4.97)	33.17(24.18 39.89)	83.37(62.20 144.04)		
SR hor	-0.87(-7.39 2.23)	32.14(24.61 36.42)	28.97(23.00 69.61)	15.02(9.11 21.50)	0.62(0.50 0.84)
MR hor	1.79(-1.20 5.17)	30.61(25.83 37.10)	24.75(13.71 32.91)	25.75(19.80 33.41)	0.85(0.77 0.94)
OR ver	-9.92(-12.79 -6.26)	25.7(21.64 34.56)	77.6(54.84 119.37)		
SR ver	-4.85(-8.91 -0.93)	26.13(19.26 31.89)	44.17(20.26 68.48)	12.08(7.32 19.76)	0.69(0.52 0.88)
MR ver	-0.06(-3.26 5.46)	23.14(17.33 28.57)	18.55(10.59 30.33)	33.79(23.17 38.06)	0.92(0.82 0.96)
OR obl	-13.05(-16.88 -5.76)	38.45(29.91 46.66)	142.47(74.90 246.37)		
SR obl	-5.48(-9.50 -0.39)	34.81(24.95 42.67)	60.68(33.25 107.82)	13.99(7.88 20.71)	0.61(0.52 0.84)
MR obl	2.03(-2.78 4.92)	33.46(24.63 43.78)	27.38(17.92 40.94)	35.09(26.38 41.31)	0.89(0.77 0.92)
OR unip	-11.4(-13.72 -6.11)	19.84(17.48 29.82)	76.86(51.94 123.54)		
SR unip	-6.72(-8.60 -0.89)	20.71(15.74 28.58)	43.95(18.24 67.64)	12.16(9.86 18.20)	0.7(0.51 0.90)
MR unip	2.63(-3.63 7.11)	19.11(13.19 25.23)	14.52(7.10 30.39)	31.5(24.98 40.63)	0.86(0.79 0.91)
Synthetic dataset results	SIR [dB]	Fetal Amp [mV]	matAmp [mV]	matAtt [dB]	QRSdetAcc
OR hor	-12.8(-9.71 -15.84)	0.63(0.44 0.90)	2.78(2.75 2.81)		
SR hor	-7.32(-11.03 -4.59)	0.51(0.33 0.70)	1.18(1.16 1.19)	8.57(8.46 8.78)	0.9(0.82 0.96)
MR hor	6.8(2.42 10.53)	0.42(0.24 0.63)	0.17(0.10 0.30)	28.25(22.41 32.79)	0.94(0.81 0.96)
OR ver	-8.61(-13.90 -4.50)	0.14(0.08 0.21)	0.37(0.37 0.38)		
SR ver	-2.8(-7.83 1.98)	0.11(0.07 0.20)	0.16(0.15 0.17)	8.35(8.08 8.67)	0.92(0.84 0.96)
MR ver	8.73(2.93 13.19)	0.12(0.06 0.20)	0.04(0.03 0.06)	21.1(17.43 26.59)	0.92(0.89 0.96)
OR obl	-9.83(-13.15 -7.05)	0.64(0.43 0.86)	1.99(1.96 2.02)		
SR obl	-3.75(-7.76 -0.44)	0.55(0.36 0.83)	0.87(0.86 0.89)	8.23(8.06 8.50)	0.92(0.84 0.96)
MR obl	8.53(3.27 12.69)	0.52(0.26 0.81)	0.18(0.11 0.32)	24.36(18.39 28.90)	0.92(0.84 0.96)
OR unip	-2.57(-5.83 -1.15)	0.92(0.74 1.04)	1.23(1.04 1.71)		
SR unip	4.81(2.80 8.05)	0.85(0.71 0.98)	0.45(0.35 0.57)	11.58(7.77 13.72)	0.93(0.89 0.96)
MR unip	6.79(5.05 10.87)	0.84(0.69 0.96)	0.36(0.24 0.45)	13.79(9.20 16.91)	0.96(0.92 0.96)

Table 6.3: Wilcoxon signed rank test results on the real dataset (significance threshold at $p < 0.05$, significant differences marked with *).

	SIR results	Maternal Att	Peak detector Acc
SR hor vs MR hor	0.0009 *	0.0001 *	0.0043 *
SR ver vs MR ver	0.0003 *	0.0000 *	0.0009 *
SR obl vs MR obl	0.0008 *	0.0000 *	0.0000 *
SR unip vs MR unip	0.0006 *	0.0000 *	0.0001 *
SR vs MR	0.0000 *	0.0000 *	0.0000 *

Table 6.4: Wilcoxon signed rank test results on the synthetic dataset (significance threshold at $p < 0.05$, significant differences marked with *).

	SIR results	Maternal Att	Peak detector Acc
SR hor vs MR hor	0.0000 *	0.0000 *	0.4514
SR ver vs MR ver	0.0000 *	0.0000 *	0.2055
SR obl vs MR obl	0.0000 *	0.0000 *	0.4115
SR unip vs MR unip	0.0002 *	0.0001 *	0.8280
SR vs MR	0.0000 *	0.0000 *	0.5800

separate channels for real and synthetic dataset are reported in table 6.3 and 6.4 respectively.

Finally, the achieved results enable the analysis of the behavior of the SR implementation over the different leads. Widrow et al. [224] asserted that the maternal attenuation strongly depends on the electrodes placement. In our dataset, the horizontal lead was parallel to the maternal lead taken as reference for the SR implementation. It is important to underline that the SIR on the raw traces was similar across the different leads, only the oblique one presenting a lower value, caused by the stronger mECG contribution to that lead (see figure 6.10), even though the fetal QRS amplitude was also higher. However, on the synthetic traces, the performance of the SR method on the horizontal abdominal lead are not significantly better than those achieved on the other leads; in particular, the results on the oblique lead outperform the

others. Again, this result should warn about the adoption of simulated signals for this kind of evaluation.

In general, in terms of output signal quality, even though the MR adaptive filter output was better than the SR one, it seemed to suffer from residual noise, not only power-line interference, thus deserving a post-processing stage that, however, was beyond the scope of this work. An example of the output signals without any post-processing is presented in figure 6.13.

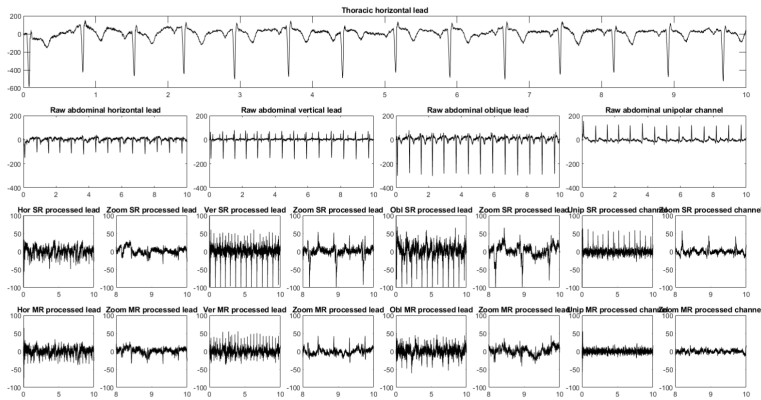


Figure 6.13: Real dataset: raw thoracic lead and raw processed abdominal leads at different zoom levels for a single subject. In detail: (i) on the first row, the thoracic horizontal maternal lead, used as reference in the SR implementation, is shown; (ii) in the second row, there are the four raw leads, so in order: horizontal, vertical, oblique lead and the unipolar channel; (iii) in the third row, the respective processed, by the SR method, signals, each one with its respective zoom, are plotted: (iv) in the last row, the processed signals by the MR technique and their zoom are displayed.

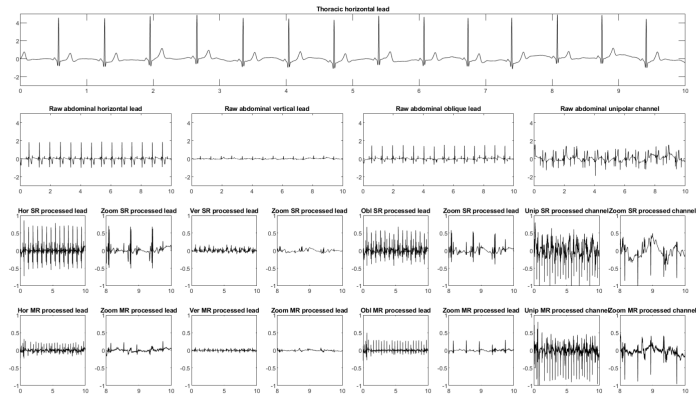


Figure 6.14: Synthetic dataset: raw thoracic lead and raw processed abdominal leads at different zoom levels for a single subject. In detail: (i) on the first row, the thoracic horizontal maternal lead, used as reference in the SR implementation, is shown; (ii) in the second row, there are the four raw leads, so in order: horizontal, vertical, oblique lead and the unipolar channel; (iii) in the third row, the respective processed, by the SR method, signals, each one with its respective zoom, are plotted; (iv) in the last row, the processed signals by the MR technique and their zoom are displayed.

Figure 6.15 and figure 6.16 show the preliminary results of the assessment of the WD approach as post-processing for both real and synthetic dataset.

The (i) analysis compared raw and post-processed data, for both SWT and SWPT. Considering the real and the synthetic data, regarding both level 6 and level 7, the preliminary results show that the WD applied on the post-processing of the extracted fECG signals achieved better performance compared to the input of the WD ($p < 0.05$, except for the Accuracy for the SWP using the Han threshold for level 7, Accuracy values for all the decompositions considering level 6, and the SNR values for the SWPT using the Universal threshold for both the levels). Despite the fetal QRS detector accuracy did not exhibit a significant improvement for the post-processed signals, WD methods enhanced the TPR outcomes, either for real and simulated data. This could be due to high Acc values reached with noisy signals and a considerable false positive rate that affects WD outputs. Focusing on the QRS detection results, their values are high also on the raw data, which explain the non-significant improvement led by the denoising.

Post-processing revealed its effectiveness in terms of cSQI, regarding the synthetic data, and of SNR for both datasets, except for the Universal threshold, probably due to the more aggressive values of its scaling factor. It is worth remarking that, while high SNR values reveal an effective noise reduction, high values of the cSQI suggest that the morphology was highly preserved by the denoising process. However, the latter has a powerful meaning if it is accompanied by high correlation coefficients, which could be computed only on simulated data.

The superior performance of the SWT decomposition compared to the SWPT one has been demonstrated through different observations. At first, considering the (ii) analysis and inspecting the three thresholds separately, regarding the synthetic data, the SWT demonstrated to have a better morphological preservation (in terms of cSQI, rho, RMSE, Spearman's correlation coefficient), whereas, in the real signals, the signal quality superiority of the SWT on the SWPT was proved essentially in terms of SNR. Moreover, as regards the (iii)

analysis, it can be asserted that the SWT denoising achieved better performance than SWPT, despite the statistical tests underlined it essentially only in terms of SNR and Acc with level 7.

With the (iv) analysis, it was pointed out that Han et al. threshold with SWT seemed the best choice in 7-level decomposition in terms of Pearson's correlation coefficient, regarding the simulated data, and, for the real traces, in terms of SNR enhancement for both levels.

Considering both simulated and real traces, the (v) comparison showed a better Acc performance of the 6-level decomposition, while the 7-level decomposition achieved respectively better performance considering the SNR results.

Even though the quantitative parameters used in the real data do not allow to assert a superior morphological preservation, by visual inspection, as it can be seen from figure 6.17, the SWT seems to reach a better performance in terms of waveform distortion compared to the SWPT. Moreover, also peculiar difference can be appreciated among the three threshold-based approaches, which underlined how the WD can lead to a very powerful enhancement of the fetal beats or, conversely, to a more shrinkage effect of the beats. The figure confirmed the Universal threshold as the worst performing one: in fact, in some cases, as can be seen in figure 6.17, it leads to a complete cancellation of the fetal beat. On the other hand, it is reported that Han et.al. threshold with SWT can be considered the best approach, as already statistically demonstrated, despite also the Minimax one achieves good denoising outcomes.

Finally, figure 6.18 represents the confusion matrix for the results of the cross-validation of the signal quality assessment.

The mean Accuracy reaches a very high value, 93.2%, with a number of TP = 60850, TN = 2495, FP = 420, FN = 4203. The Sensitivity is 93.5%, while the Specificity is 85.6%.

The result shows how it is possible to know, a-priori, computing the features on the unprocessed fetal ECG abdominal traces, which are the channels that are characterized by the most-informative components.

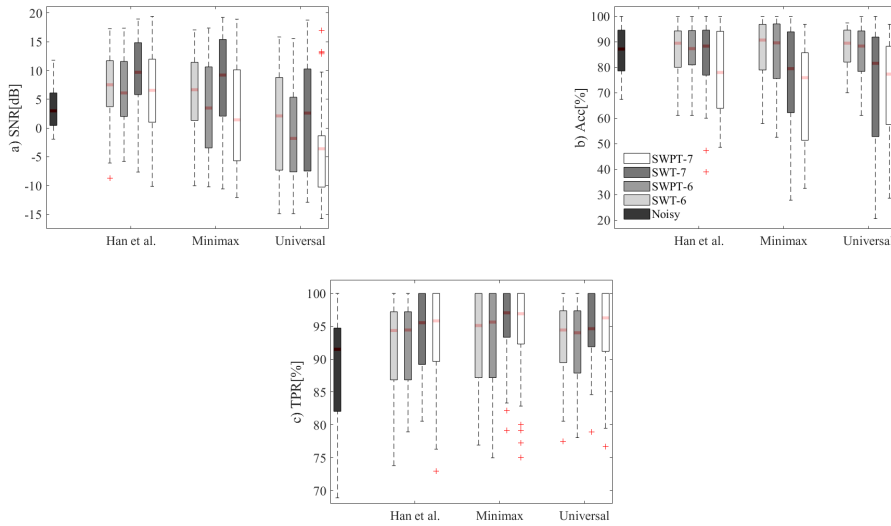


Figure 6.15: SNR, Accuracy and TPR results for real data.

6.6 Conclusion

Regarding the first study, the comparative analysis confirmed the superiority of the MR implementation compared to the SR one ($p < 0.0001$) and the strong dependency of the latter from the electrode placement. Our quantitative results in terms of mECG attenuation and SIR values demonstrated how, by using multiple mECG reference leads rather than a single one, even when dealing with a reference lead that is parallel to the abdominal one, it is always possible to achieve superior performance. Moreover, the accuracy of a fetal QRS detector applied on the output of the SR adaptive filter is poor on real recordings (68% on average, $\sigma = 0.0097$). This means that SR approaches should be avoided in any case when trying to solve the non-invasive fECG extraction problem, even when simply the heart rate is pursued and even when a reference channel parallel to the abdominal one is available. Overall, we can conclude that it is completely worth using multiple mECG reference leads rather than a single one,

when dealing with real non-invasive fECG recordings. It is also important to stress that the synthetic dataset in some cases led to results in contrast with the experimental evidence, then suggesting caution in using such synthetic signals or, at least, in discussing the results achieved by the algorithms over them.

Secondarily, the results of the study highlight a better performance of differential measurements, enhancing the fECG amplitude, although they can also amplify the maternal interference, depending on the chosen abdominal lead.

The second study analysed different wavelet-based post-processing methods for the denoising of non-invasive fECG traces extracted by the previous method. Considering the strong influence on the denoising quality by the threshold definition, three thresholds from the literature were also tested. All the signals were decomposed with the SWT and the SWPT by using the Haar mother wavelet. In both cases, 6-level and 7-level decompositions were tested, in order to suggest an ad-hoc denoising procedure focusing on the fECG spectral bands of major interest.

The results reveal how the adoption of a WD method allows achieving better performances, suggesting that the proposed approach can be a step forward the achievement of a better morphological identification and preservation of the fetal ECG. However, the higher complexity of the SWPT should be compensated by a significantly better performance, which was not verified in the proposed preliminary assessment.

The last study is a preliminary work towards the automatic recognition of the most-informative recorded traces, when a set of multichannels recordings is available.

This is important considering that the reduction in the number of electrodes to be applied on the maternal body is one of the constraints of a wearable monitoring application.

Additionally, this study can be used to investigate the most-informative electrodes positions on the maternal abdomen, regardless also the fetus presentation.

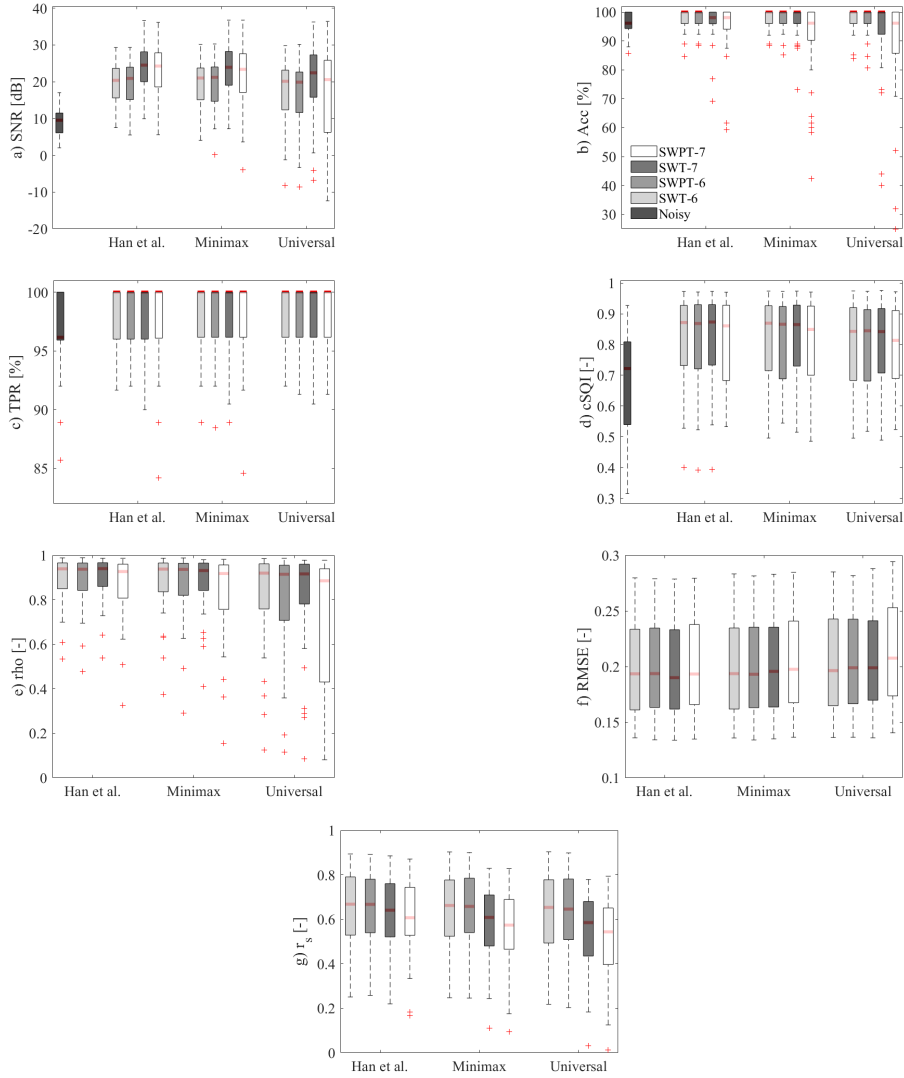


Figure 6.16: SNR, Accuracy, TPR, cSQI, Pearson's correlation coefficient, RMSE and Spearman's correlation coefficient results for synthetic data.

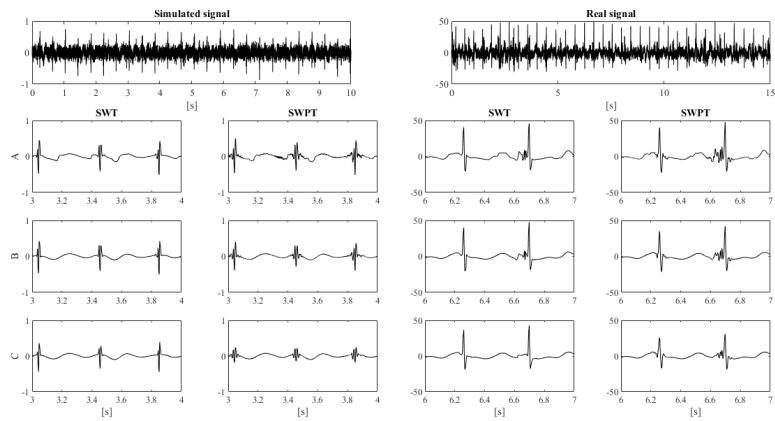


Figure 6.17: Example of SWT and SWPT denoising results with 7-level decomposition, with the three different thresholds. A: Han et al. threshold, B: Minimax and C: Universal. On the right, results obtained on a real fECG signal are reported, while on the left side results on a simulated signal are represented. Zoom on one-second of each denoised signal is reported in order to appreciate fetal peaks morphology after wavelet denoising.

Confusion Matrix

Output Class	0	60850 89.5%	4203 6.2%	93.5% 6.5%
	1	420 0.6%	2495 3.7%	85.6% 14.4%
		99.3% 0.7%	37.2% 62.8%	93.2% 6.8%
		0	1	Target Class

Figure 6.18: Confusion matrix relative to the signal quality assessment of the unprocessed fetal ECG traces.

Chapter 7

Conclusion

This PhD project was based on the development and the analysis of a novel multimodal open-access dataset for non-invasive fetal electrocardiography (ECG) and Doppler studies, and to the best of our knowledge is the first dataset of this kind. It is unique in terms of features and enables testing multiple signal processing techniques for fetal ECG extraction, also giving the possibility to study the relationship between fetal PWD and ECG.

We investigated the impact of different steps in the processing chain for the PWD envelope extraction, demonstrating that only two phases have a major effect. This study also revealed how the adoption of a supervised classifier trained with the samples representing the upper and lower envelopes of the PWD, with eight additional features based on the area under the curve of the envelopes and the brightness of the pixels enclosed in such areas, helps in achieving excellent detection results when the aim is to automatic identify the complete and measurable fetal cardiac cycles in the PWD trace. Moreover, a germinal work presented the implementation of a possible future valuable software that can be used in real-time by the cardiologist to compute several important clinical parameters.

Considering the fetal ECG extraction, the main constraints of an unobtrusive wearable monitoring systems are the reduction in the number of electrodes, to be applied on the maternal body, and the low-power feature. The comparison

between the single and multi-reference versions of adaptive filters, which can reduce the number of electrodes needed for this application, revealed that the single-reference approaches should be avoided in any case, even when simply the heart rate is pursued and even when a reference channel parallel to the abdominal one is available. The output of the best performing adaptive algorithm still suffers from residual noise, so that an ad-hoc denoising stage is required. The adoption of a wavelet-denoising method suggested that this approach can be a step forward the preservation of the fetal ECG morphology. Regarding the low-power characteristics, using features computed on the raw fetal ECG abdominal traces, it was possible to see which were the channels that were characterized by the most-informative components, thus allowing the processing on a reduced number of channels.

The main limitation of this work is represented by the presence of signals only from healthy fetuses, depending on the experimental protocol approved by the Ethical Committee. A more comprehensive study, including a larger population with different heart conditions, at different gestational ages, could demonstrate the generalizability of the results among the different presented techniques.

Considering the topics of this thesis, the natural future works are represented by the possibility of applying multi-modality approaches for the analysis of the fetal cardiological health status. In fact, the data fusion could represent the future for the monitoring of the fetal cardiological activity and for the study of the physiological mechanisms behind fetal cardiological functions, thanks to a hitherto unavailable dataset.

Bibliography

- [1] ACOG Practice Bulletin No. 106: Intrapartum fetal heart rate monitoring: nomenclature, interpretation, and general management principles. *Obstetrics and gynecology*, 114(1):192–202, jul 2009. (Cited on pages 1, 16, 17, and 18.)
- [2] A A Damen and J van der Kam. The use of the singular value decomposition in electrocardiography. *Medical & biological engineering & computing*, 20:473–482, 1982. (Cited on page 36.)
- [3] S Abboud, G Barkai, S Mashiach, and D Sadeh. Quantification of the fetal electrocardiogram using averaging technique. *Computers in biology and medicine*, 20(3):147–155, 1990. (Cited on page 42.)
- [4] M Ahmadi, M Ayat, K Assaleh, and H Al-Nashash. Fetal ECG Signal Enhancement using Polynomial Classifiers and Wavelet Denoising. In *2008 Cairo International Biomedical Engineering Conference*, pages 1–4, 2008. (Cited on page 37.)
- [5] M.M.S. Algunaidi, M.A.M. Ali, and Md. Fokhrul Islam. Evaluation of an improved algorithm for fetal qrs detection. *International Journal of Physical Sciences*, 6:213–220, 01 2011. (Cited on page 63.)
- [6] S Almagro, M M Elena, M J Bastiaans, and J M Quero. A new mother wavelet for fetal electrocardiography, to achieve optimal denoising and compressing results. In *2006 Computers in Cardiology*, pages 157–160, 2006. (Cited on pages 36 and 125.)

- [7] Rute Almeida, Hernani Goncalves, Joao Bernardes, and Ana Paula Rocha. Fetal QRS detection and heart rate estimation: a wavelet-based approach. *Physiological measurement*, 35(8):1723–1735, aug 2014. (Cited on page 36.)
- [8] D G Altman and J M Bland. Measurement in Medicine: The Analysis of Method Comparison Studies. *Journal of the Royal Statistical Society. Series D (The Statistician)*, 32(3):307–317, 1983. (Cited on page 59.)
- [9] Nandan S Anavekar and Jae K Oh. Doppler echocardiography: a contemporary review. *Journal of cardiology*, 54(3):347–358, dec 2009. (Cited on page 10.)
- [10] G Andelfinger, J C Fouron, S E Sonesson, and F Proulx. Reference values for time intervals between atrial and ventricular contractions of the fetal heart measured by two Doppler techniques. *The American journal of cardiology*, 88(12):1433–6, A8, dec 2001. (Cited on page 26.)
- [11] F Andreotti, F Gräßer, H Malberg, and S Zaunseder. Non-invasive Fetal ECG Signal Quality Assessment for Multichannel Heart Rate Estimation. *IEEE Transactions on Biomedical Engineering*, 64(12):2793–2802, 2017. (Cited on page 40.)
- [12] Fernando Andreotti, Joachim Behar, Sebastian Zaunseder, Julien Oster, and Gari D Clifford. An open-source framework for stress-testing non-invasive foetal ECG extraction algorithms. *Physiological measurement*, 37(5):627–648, may 2016. (Cited on pages 32, 33, 34, 115, and 131.)
- [13] Fernando Andreotti, Maik Riedl, Tilo Himmelsbach, Daniel Wedekind, Niels Wessel, Holger Stepan, Claudia Schmieder, Alexander Jank, Hagen Malberg, and Sebastian Zaunseder. Robust fetal ECG extraction and detection from abdominal leads. *Physiological measurement*, 35(8):1551–1567, aug 2014. (Cited on pages 40 and 63.)
- [14] Manpreet Aneja, Birmohan Singh, and Seema. *Comparison of different approaches for removal of Baseline wander from ECG signal*, volume 5. jan 2011. (Cited on page 35.)

- [15] Jose Antonio Apolinario JR. *QRD-RLS Adaptive Filtering*. Springer, 2009. (Cited on pages 121 and 122.)
- [16] W.F. Armstrong and T. Ryan. *Feigenbaum's Echocardiography*. Wolters Kluwer, 2018. (Cited on pages 19 and 20.)
- [17] Bhawna Arya, Rathinaswamy Govindan, Anita Krishnan, Adre Duplessis, and Mary T Donofrio. Feasibility of noninvasive fetal electrocardiographic monitoring in a clinical setting. *Pediatric cardiology*, 36(5):1042–1049, jun 2015. (Cited on page 42.)
- [18] Diogo Ayres-de Campos, Catherine Y Spong, and Edwin Chandrharan. FIGO consensus guidelines on intrapartum fetal monitoring: Cardiotocography. *International journal of gynaecology and obstetrics: the official organ of the International Federation of Gynaecology and Obstetrics*, 131(1):13–24, oct 2015. (Cited on pages 10 and 16.)
- [19] AG Batista, S. Najdi, D. M. Godinho, F. Serrano, M.D. Ortigueira, and R.T. Rato. A multichannel time-frequency and multi-wavelet toolbox for uterine electromyography processing and visualisation. *Computers in Biology and Medicine*, 76:178–191, 2016. (Cited on page 18.)
- [20] J Behar, J Oster, Q Li, and G D Clifford. A single channel ECG quality metric. In *2012 Computing in Cardiology*, pages 381–384, 2012. (Cited on page 38.)
- [21] Joachim Behar, Fernando Andreotti, Sebastian Zaunseder, Qiao Li, Julien Oster, and Gari D Clifford. *An ECG simulator for generating maternal-foetal activity mixtures on abdominal ECG recordings*, volume 35. jul 2014. (Cited on pages 32, 33, 115, and 131.)
- [22] Joachim Behar, Alistair Johnson, Gari D Clifford, and Julien Oster. A Comparison of Single Channel Fetal ECG Extraction Methods. *Annals of Biomedical Engineering*, 42(6):1340–1353, 2014. (Cited on pages 36, 116, 122, and 123.)

- [23] Joachim Behar, Julien Oster, and Gari D Clifford. Combining and benchmarking methods of foetal ECG extraction without maternal or scalp electrode data. *Physiological Measurement*, 35(8):1569–1589, jul 2014. (Cited on pages 129, 140, and 141.)
- [24] Joachim Behar, Julien Oster, Qiao Li, and Gari D Clifford. ECG signal quality during arrhythmia and its application to false alarm reduction. *IEEE transactions on bio-medical engineering*, 60(6):1660–1666, jun 2013. (Cited on page 39.)
- [25] Joachim Behar, Tingting Zhu, Julien Oster, Alisa Niksch, Douglas Y Mah, Terrence Chun, James Greenberg, Cassandre Tanner, Jessica Harrop, Reza Sameni, Jay Ward, Adam J Wolfberg, and Gari D Clifford. Evaluation of the fetal qt interval using non-invasive fetal ecg technology. *Physiol Meas.*, 37(9):1392–403, 2016. (Cited on page 10.)
- [26] P. Bergveld, A. J. Kolling, and J. H. J. Peuscher. Real-time fetal ecg recording. *IEEE Transactions on Biomedical Engineering*, BME-33(5):505–509, May 1986. (Cited on page 63.)
- [27] Manuel Blanco-Velasco, Binwei Weng, and Kenneth E Barner. ECG signal denoising and baseline wander correction based on the empirical mode decomposition. *Computers in Biology and Medicine*, 38(1):1–13, 2008. (Cited on page 35.)
- [28] Dirk Callaerts, Joos Vandewalle, Willy Sansen, Jozef D Janssens, Gaston Vantrappen, Herman P. van Geijn, and Frans J.A. Copray. Acquisition and processing of the antepartum fecg. 1994. (Cited on page 63.)
- [29] Gustau Camps-Valls, Manuel Martín, and Emilio Olivas. *Fetal ECG extraction using an FIR neural network*. feb 2001. (Cited on page 36.)
- [30] J Canny. A Computational Approach to Edge Detection. *IEEE Transactions on Pattern Analysis and Machine Intelligence*, PAMI-8(6):679–698, 1986. (Cited on page 81.)

- [31] J.-F Cardoso. Multidimensional independent component analysis. In *Proc. ICASSP*, volume 4, pages 1941 – 1944 vol.4, 1998. (Cited on page 36.)
- [32] Jean-François Cardoso. *Source Codes for Blind Source Separation and Independent Component Analysis*, 2005. (Cited on page 56.)
- [33] N Chaitra, G PraveenKumarY, and M Z Kurian. Design and Implementation of High Performance Adaptive FIR Filter Systems Using QRD-RLS Method. 2014. (Cited on page 118.)
- [34] Prashanth Chetlur Adithya, Ravi Sankar, Wilfrido Moreno, and Stuart Hart. Trends in fetal monitoring through phonocardiography: Challenges and future directions. *Biomedical Signal Processing and Control*, 33:289–305, 2017. (Cited on page 10.)
- [35] Ee Ling Chia, Ting Fei Ho, Mary Rauff, and William C L Yip. Cardiac time intervals of normal fetuses using noninvasive fetal electrocardiography. *Prenatal diagnosis*, 25(7):546–552, jul 2005. (Cited on page 42.)
- [36] W Chien, W Liu, and A Liu. Envelope Approximation on Doppler Ultrasound Spectrogram for Estimating Flow Speed in Carotid Artery. In *2016 International Computer Symposium (ICS)*, pages 415–418, 2016. (Cited on page 44.)
- [37] Luca Citi and Silvestro Micera. *Wavelet Denoising and Conditioning of Neural Recordings*, chapter 9, pages 173–182. John Wiley & Sons, Ltd, 2013. (Cited on page 124.)
- [38] G D Clifford, J Behar, Q Li, and I Rezek. Signal quality indices and data fusion for determining clinical acceptability of electrocardiograms. *Physiological measurement*, 33(9):1419–1433, sep 2012. (Cited on page 39.)
- [39] Gari Clifford. ECG Statistics, Noise, Artifacts, and Missing Data. *Advanced Methods and Tools for ECG Data Analysis*, 2006. (Cited on page 129.)

- [40] Gari Clifford, Reza Sameni, Jay Ward, Julian Robinson, and Adam J Wolfberg. Clinically accurate fetal ECG parameters acquired from maternal abdominal sensors. *American journal of obstetrics and gynecology*, 205(1):47.e1–5, jul 2011. (Cited on pages 10 and 63.)
- [41] Gari D Clifford, Ikaro Silva, Joachim Behar, and George B Moody. Non-invasive fetal ECG analysis. *Physiological measurement*, 35(8):1521, 2014. (Cited on page 125.)
- [42] Wayne Cohen, Sophia Ommani, Sarmina Hassan, Fadi Mirza, Molham Solomon, Raymond Brown, Barry S, John M Himsworth, and Barrie Hayes-Gill. Accuracy and reliability of fetal heart rate monitoring using maternal abdominal surface electrodes. *Acta Obstet Gynecol Scand.*, 91(11), 2012. (Cited on page 10.)
- [43] Ronald R Coifman and David L Donoho. Translation-invariant de-noising. In *Wavelets and statistics*, pages 125–150. Springer, 1995. (Cited on page 124.)
- [44] N Colley, D G Talbert, N G Abraham, W L Davies, P Fayers, and D P Southall. The fetal phonogram: a measure of fetal activity. *Lancet (London, England)*, 1(8487):931–935, apr 1986. (Cited on page 11.)
- [45] M. Cremer. Über die direkte ableitung der aktionströme des menschlichen herzens vom oesophagus und Über das elektrokardiogramm des fetus. *Münchener Medizinische Wochenschrift.*, 53:811–813, apr 1906. (Cited on page 30.)
- [46] Pani D., Barabino G., and L. Raffo. NInFEA: an embedded framework for the real-time evaluation of fetal ECG extraction algorithms, 2013. (Cited on page 114.)
- [47] C Daluwatte, L Johannesen, L Galeotti, J Vicente, D G Strauss, and C G Scully. Assessing ECG signal quality indices to discriminate ECGs with artefacts from pathologically different arrhythmic ECGs. *Physiological measurement*, 37(8):1370–1382, aug 2016. (Cited on page 39.)

- [48] M. De Felici. *Embriologia umana. Morfogenesi, processi molecolari, aspetti clinici*. Piccin-Nuova Libreria, 2009. (Cited on pages 6 and 7.)
- [49] Lieven De Lathauwer, Bart De Moor, and Joos Vandewalle. Fetal Electrocardiogram Extraction by Blind Source Subspace Separation. *IEEE transactions on bio-medical engineering*, 47:567–572, 2000. (Cited on page 36.)
- [50] B A S del Rio, T Lopetegi, and I Romero. Assessment of different methods to estimate electrocardiogram signal quality. In *2011 Computing in Cardiology*, pages 609–612, 2011. (Cited on page 38.)
- [51] Paulo Sergio Diniz. *Adaptive Filtering: Algorithms and Practical Implementation*. Kluwer Academic Publishers, Norwell, MA, USA, 2 edition, 2002. (Cited on page 120.)
- [52] Janet A. DiPietro, Marc H. Bornstein, Chun-Shin Hahn, Kathleen Costigan, and Aristide Achy-Brou. Fetal heart rate and variability: stability and prediction to developmental outcomes in early childhood. *Child Dev.*, 78(6):1788–1798, 2007. (Cited on page 17.)
- [53] Mary T. Donofrio, Anita J. Moon-Grady, Lisa K. Hornberger, Joshua A. Copel, Mark S. Sklansky, Alfred Abuhamad, Bettina F. Cuneo, James C. Huhta, Richard A. Jonas, Anita Krishnan, Stephanie Lacey, Wesley Lee, Erik C. Michelfelder, Gwen R. Rempel, Norman H. Silverman, Thomas L. Spray, Janette F. Strasburger, Wayne Tworetzky, and Jack Rychik. Diagnosis and treatment of fetal cardiac disease. *Circulation*, 129(21):2183–2242, 2014. (Cited on pages 1, 10, 16, 22, 32, 43, and 51.)
- [54] David L Donoho. De-noising by soft-thresholding. *IEEE transactions on information theory*, 41(3):613–627, 1995. (Cited on pages 115, 126, and 127.)
- [55] David L Donoho and Jain M Johnstone. Ideal spatial adaptation by wavelet shrinkage. *biometrika*, 81(3):425–455, 1994. (Cited on pages 115, 126, and 127.)

- [56] De Moor B.L.R. (ed.). Daisy: Database for the identification of systems. <http://homes.esat.kuleuven.be/~smc/daisy/>, Online; accessed 17 February 2019. (Cited on pages 32 and 34.)
- [57] I Edler and C H Hertz. The use of ultrasonic reflectoscope for the continuous recording of the movements of heart walls. *Clinical physiology and functional imaging*, 24(3):118–136, may 2004. (Cited on page 43.)
- [58] Manuela Ferrario, Maria G Signorini, and Giovanni Magenes. Complexity analysis of the fetal heart rate variability: early identification of severe intrauterine growth-restricted fetuses. *Medical & biological engineering & computing*, 47(9):911–919, sep 2009. (Cited on page 17.)
- [59] Anna Finnemore and Alan Groves. Physiology of the fetal and transitional circulation. *Seminars in fetal & neonatal medicine*, 20(4):210–216, aug 2015. (Cited on pages 7, 8, and 11.)
- [60] James D Foley, Andries van Dam, Steven K Feiner, and John F Hughes. *Computer Graphics: Principles and Practice (2Nd Ed.)*. Addison-Wesley Longman Publishing Co., Inc., Boston, MA, USA, 1990. (Cited on page 83.)
- [61] E Fotiadou, J O E H van Laar, S G Oei, and R Vullings. Enhancement of low-quality fetal electrocardiogram based on time-sequenced adaptive filtering. *Medical & biological engineering & computing*, 56(12):2313–2323, dec 2018. (Cited on pages 37 and 136.)
- [62] Ernest Frank. General Theory of Heart-Vector Projection. *Circulation Research*, 2(3):258–270, may 1954. (Cited on page 14.)
- [63] Akimune Fukushima, Kenji Nakai, Tomonobu Kanasugi, Miyuki Terata, and Toru Sugiyama. Assessment of fetal autonomic nervous system activity by fetal magnetocardiography: Comparison of normal pregnancy and intrauterine growth restriction. *Journal of pregnancy*, 2011:218162, 04 2011. (Cited on page 10.)

- [64] Catherine Gagnon, Jean-Luc Bigras, Jean-Claude Fouron, and Frederic Dallaire. Reference Values and Z Scores for Pulsed-Wave Doppler and M-Mode Measurements in Fetal Echocardiography. *Journal of the American Society of Echocardiography*, 29(5):448–460.e9, may 2016. (Cited on pages 22 and 43.)
- [65] Ping Gao, Ee-Chien Chang, and L Wyse. Blind separation of fetal ECG from single mixture using SVD and ICA. In *Fourth International Conference on Information, Communications and Signal Processing, 2003 and the Fourth Pacific Rim Conference on Multimedia. Proceedings of the 2003 Joint*, volume 3, pages 1418–1422 vol.3, 2003. (Cited on page 36.)
- [66] Gaetano D Gargiulo, Paolo Bifulco, Mario Cesarelli, Alistair L McEwan, Hossein Moeinzadeh, Aiden O’Loughlin, Ibrahim M Shugman, Jonathan C Tapson, and Aravinda Thiagalingam. On the Einthoven Triangle: A Critical Analysis of the Single Rotating Dipole Hypothesis. *Sensors (Basel, Switzerland)*, 18(7), jul 2018. (Cited on page 14.)
- [67] M E Godfrey, B Messing, S M Cohen, D V Valsky, and S Yagel. Functional assessment of the fetal heart: a review. *Ultrasound in obstetrics & gynecology : the official journal of the International Society of Ultrasound in Obstetrics and Gynecology*, 39(2):131–144, feb 2012. (Cited on page 25.)
- [68] Ary L. Goldberger, Luis A. N. Amaral, Leon Glass, Jeffrey M. Hausdorff, Plamen Ch. Ivanov, Roger G. Mark, Joseph E. Mietus, George B. Moody, Chung-Kang Peng, and H. Eugene Stanley. Physiobank, physiotoolkit, and physionet: Components of a new research resource for complex physiologic signals. *Circulation*, 101(23):e215–e220, 2000. (Cited on pages 32 and 34.)
- [69] R C Gonzalez and R E Woods. *Digital Image Processing*. jan 2006. (Cited on pages 77 and 81.)

- [70] Rafael C Gonzalez and Richard E Woods. *Digital Image Processing*. Addison-Wesley Longman Publishing Co., Inc., Boston, MA, USA, 2nd edition, 2001. (Cited on page 81.)
- [71] K R Greene, G S Dawes, H Lilja, and K G Rosen. Changes in the ST waveform of the fetal lamb electrocardiogram with hypoxemia. *American journal of obstetrics and gynecology*, 144(8):950–958, dec 1982. (Cited on page 30.)
- [72] Hayit Greenspan, Oron Shechner, Mickey Scheinowitz, and Micha S Feinberg. Doppler echocardiography flow-velocity image analysis for patients with atrial fibrillation. *Ultrasound in Medicine and Biology*, 31(8):1031–1040, aug 2005. (Cited on pages xiii, 44, 72, 73, 76, 77, 80, 81, 83, 96, 97, and 106.)
- [73] Rosalie Grivell, Zarko Alfirevic, Gillian Ml Gyte, and Declan Devane. *Antenatal cardiotocography for fetal assessment*, volume 9. John Wiley & Sons, Ltd., 2015. (Cited on page 10.)
- [74] Isabelle Guyon and André Elisseeff. An introduction to variable and feature selection. *J. Mach. Learn. Res.*, 3:1157–1182, March 2003. (Cited on page 130.)
- [75] John .E Hall and Arthur C. Guyton. *Guyton and Hall textbook of medical physiology*. Philadelphia, PA: Saunders Elsevier., 2006. (Cited on pages xi, 12, 13, 14, 15, 16, and 17.)
- [76] Min Han, Yuhua Liu, Jianhui Xi, and Wei Guo. Noise Smoothing for Nonlinear Time Series Using Wavelet Soft Threshold. *Signal Processing Letters, IEEE*, 14:62–65, 2007. (Cited on pages 115, 127, and 128.)
- [77] Weituo Hao, Yu Chen, and Yi Xin. ECG baseline wander correction by mean-median filter and discrete wavelet transform. *Annual International Conference of the IEEE Engineering in Medicine and Biology Society. IEEE Engineering in Medicine and Biology Society. Annual Conference*, 2011:2712–2715, 2011. (Cited on page 35.)

- [78] H Hassanpour and A Parsaei. Fetal ECG Extraction Using Wavelet Transform. In *2006 International Conference on Computational Intelligence for Modelling Control and Automation and International Conference on Intelligent Agents Web Technologies and International Commerce (CIMCA'06)*, page 179, 2006. (Cited on page 36.)
- [79] Risa Hayashi, Kenji Nakai, Akimune Fukushima, Manabu Itoh, and Toru Sugiyama. Development and significance of a fetal electrocardiogram recorded by signal-averaged high-amplification electrocardiography. *International heart journal*, 50(2):161–171, mar 2009. (Cited on page 42.)
- [80] Simon Haykin. *Neural Networks: A Comprehensive Foundation*. Prentice Hall PTR, Upper Saddle River, NJ, USA, 1st edition, 1994. (Cited on page 91.)
- [81] Taigang He, Gari Clifford, and Lionel Tarassenko. Application of independent component analysis in removing artefacts from the electrocardiogram. *Neural Computing & Applications*, 15(2):105–116, 2006. (Cited on page 129.)
- [82] E Hernandez-Andrade, J Lopez-Tenorio, H Figueroa-Diesel, J Sanin-Blair, E Carreras, L Cabero, and E Gratacos. A modified myocardial performance (Tei) index based on the use of valve clicks improves reproducibility of fetal left cardiac function assessment. *Ultrasound in obstetrics & gynecology : the official journal of the International Society of Ultrasound in Obstetrics and Gynecology*, 26(3):227–232, sep 2005. (Cited on page 26.)
- [83] E Hernandez-Andrade, M Patwardhan, M Cruz-Lemini, and S Luewan. Early Evaluation of the Fetal Heart. *Fetal Diagnosis and Therapy*, 42(3):161–173, 2017. (Cited on page 8.)
- [84] Bo Hjorth. EEG analysis based on time domain properties. *Electroencephalography and Clinical Neurophysiology*, 29(3):306–310, 1970. (Cited on page 130.)

- [85] E H Hon. Instrumentation of fetal heart rate and fetal electrocardiography. II. A vaginal electrode. *American journal of obstetrics and gynecology*, 86:772–784, jul 1963. (Cited on page 30.)
- [86] E H Hon. Noise reduction in fetal electrocardiography. *Medical arts and sciences*, 18:63–66, 1964. (Cited on page 37.)
- [87] Dirk Hoyer, Eva-Maria Kowalski, Alexander Schmidt, Florian Tetschke, Samuel Nowack, Anja Rudolph, Ulrike Wallwitz, Isabelle Kynass, Franziska Bode, Janine Tegtmeyer, Kathrin Kumm, Liviu Moraru, Theresa Götz, Jens Haueisen, Otto W. Witte, Ekkehard Schleußner, and Uwe Schneider. Fetal autonomic brain age scores, segmented heart rate variability analysis, and traditional short term variability. *Frontiers in Human Neuroscience*, 8:948, 2014. (Cited on page 17.)
- [88] Dirk Hoyer, Jan Zebrowski, Dirk Cysarz, Hernani Goncalves, Adelina Pytlik, Celia Amorim-Costa, Joao Bernardes, Diogo Ayres-de Campos, Otto W Witte, Ekkehard Schleussner, Lisa Stroux, Christopher Redman, Antoniya Georgieva, Stephen Payne, Gari Clifford, Maria G Signorini, Giovanni Magenes, Fernando Andreotti, Hagen Malberg, Sebastian Zauseder, Igor Lakhno, and Uwe Schneider. Monitoring fetal maturation-objectives, techniques and indices of autonomic function. *Physiological measurement*, 38(5):R61–R88, may 2017. (Cited on page 17.)
- [89] X B Huang, J A Crowe, J M Herbert, and M S Woolfson. A windows application for real-time fetal ECG analysis. *Computers and biomedical research, an international journal*, 27(6):419–433, dec 1994. (Cited on page 37.)
- [90] Maria G Jafari and Jonathon A Chambers. Fetal electrocardiogram extraction by sequential source separation in the wavelet domain. *IEEE transactions on bio-medical engineering*, 52(3):390–400, mar 2005. (Cited on page 36.)
- [91] N Jamil, T M T Sembok, and Z A Bakar. Noise removal and enhancement of binary images using morphological operations. In *2008 Inter-*

- national Symposium on Information Technology*, volume 4, pages 1–6, 2008. (Cited on page 83.)
- [92] Fahimeh Jamshidian-Tehrani and Reza Sameni. Fetal ECG extraction from time-varying and low-rank noninvasive maternal abdominal recordings. *Physiological measurement*, 39(12):125008, 2018. (Cited on pages 16 and 56.)
- [93] L. Jana. *Early Fetal Heart Development: 0-9 Weeks*. The Dr. Spock Company, 2004. (Cited on pages xi and 6.)
- [94] Bageshree Cheulkar Janette F. Strasburger and Ronald T. Wakai. Magnetocardiography for fetal arrhythmias. *Heart Rhythm*, 5(7):1073–1076, 2008. (Cited on page 10.)
- [95] Joo OhKim Jeffrey P.Phelan. Fetal heart rate observations in the brain-damaged infant. *Seminars in Perinatology*, 24(3):221–9, 2000. (Cited on page 17.)
- [96] Zhang Jie-Min, Xiaolin Huang, Guan Qun, Liu Tie-Bing, Li Ping, Zhao Ying, and Hongxing Liu. Some regularity on how to locate electrodes for higher fecg snrs. *Chinese Physics B*, 24, 03 2015. (Cited on page 63.)
- [97] Caroline B. Jones John M. Simpson. Structural heart disease in the fetus. *Pediatric and Congenital Cardiology, Cardiac Surgery and Intensive Care*, pages 201–225, 2014. (Cited on page 1.)
- [98] Alistair E W Johnson, Joachim Behar, Fernando Andreotti, Gari D Clifford, and Julien Oster. Multimodal heart beat detection using signal quality indices. *Physiological measurement*, 36(8):1665–1677, aug 2015. (Cited on page 39.)
- [99] R Kahankova, R Martinek, and P Bilik. Fetal ECG extraction from abdominal ECG using RLS based adaptive algorithms. In *2017 18th International Carpathian Control Conference (ICCC)*, pages 337–342, 2017. (Cited on pages 36, 116, and 138.)

- [100] P P Kanjilal, S Palit, and G Saha. Fetal ECG extraction from single-channel maternal ECG using singular value decomposition. *IEEE Transactions on Biomedical Engineering*, 44(1):51–59, 1997. (Cited on page 36.)
- [101] Evaggelos C Karvounis, Markos G Tsipouras, Dimitrios I Fotiadis, and Katerina K Naka. An automated methodology for fetal heart rate extraction from the abdominal electrocardiogram. *IEEE transactions on information technology in biomedicine : a publication of the IEEE Engineering in Medicine and Biology Society*, 11(6):628–638, nov 2007. (Cited on page 63.)
- [102] A Khamene and S Negahdaripour. A new method for the extraction of fetal ECG from the composite abdominal signal. *IEEE transactions on bio-medical engineering*, 47(4):507–516, apr 2000. (Cited on page 36.)
- [103] A H Khandoker, F Marzbanrad, Y Kimura, S A Nuaimi, and M Palaniswami. Assessing the development of fetal myocardial function by a novel Doppler myocardial performance index. In *2016 38th Annual International Conference of the IEEE Engineering in Medicine and Biology Society (EMBC)*, pages 3753–3756, 2016. (Cited on page 27.)
- [104] Ahsan Khandoker, Emad Ibrahim, Sayaka Oshio, and Yoshitaka Kimura. Validation of beat by beat fetal heart signals acquired from four-channel fetal phonocardiogram with fetal electrocardiogram in healthy late pregnancy. *Scientific Reports*, 8(1):13635, 2018. (Cited on page 11.)
- [105] Ahsan H Khandoker, Yoshitaka Kimura, Takuya Ito, Naoaki Sato, Kunihiro Okamura, and Marimuthu Palaniswami. Antepartum non-invasive evaluation of opening and closing timings of the cardiac valves in fetal cardiac cycle. *Medical & biological engineering & computing*, 47(10):1075–1082, oct 2009. (Cited on page 45.)
- [106] N V Kiruthika, B Prabhakar, and M R Reddy. Automated Assessment of Aortic Regurgitation using 2D Doppler Echocardiogram. In *Proceedings of the 2006 IEEE International Workshop on Imaging Systems and*

- Techniques (IST 2006)*, pages 95–99, 2006. (Cited on pages xiii, 44, 72, 74, 76, 77, 79, 81, 97, and 106.)
- [107] Joseph Kisslo and David Bruce Adams. Principles of doppler echocardiography and the doppler examination # 1. 2001. (Cited on pages 21, 22, and 52.)
- [108] Paul Kligfield, Leonard S Gettes, James J Bailey, Rory Childers, Barbara J Deal, E William Hancock, Gerard van Herpen, Jan A Kors, Peter Macfarlane, David M Mirvis, Olle Pahlm, Pentti Rautaharju, Galen S Wagner, Mark Josephson, Jay W Mason, Peter Okin, Borys Surawicz, and Hein Wellens. Recommendations for the standardization and interpretation of the electrocardiogram: part I: the electrocardiogram and its technology a scientific statement from the American Heart Association Electrocardiography and Arrhythmias Committee, Council on Clin. *Journal of the American College of Cardiology*, 49(10):1109–1127, mar 2007. (Cited on pages 35 and 123.)
- [109] M. Kotas, J. Jezewski, A. Matonia, and T. Kupka. Towards noise immune detection of fetal qrs complexes. *Computer Methods and Programs in Biomedicine*, 97(3):241 – 256, 2010. (Cited on pages 32 and 34.)
- [110] J Kovacevic and M Vetterli. *Wavelets and Subband Coding*. Prentice-Hall signal processing series. Prentice Hall PTR, 1995. (Cited on page 124.)
- [111] F Kovács, K Kádár, Gábor Hosszú, Á T. Balogh, Tamas Zsedrovits, N Kersner, A Nagy, and Gy Jeney. Screening of congenital heart diseases with fetal phonocardiography. *International Journal of Biomedical and Biological Engineering*, 9(6), 2015. (Cited on page 10.)
- [112] Benjamin J. Landis, Allison Levey, Stephanie M. Levasseur, Julie S. Glickstein, Charles S. Kleinman, Lynn L. Simpson, and Ismee A. Williams. Prenatal diagnosis of congenital heart disease and birth outcomes. *Pediatr Cardiol.*, 34(3):597–605, 2013. (Cited on page 8.)
- [113] Christopher A. Lear, Jenny A. Westgate, Austin Ugwumadu, Jan G. Nijhuis, Peter R. Stone, Antoniya Georgieva, Tomoaki Ikeda, Guido

- Wassink, Laura Bennet, and Alistair J. Gunn. Understanding fetal heart rate patterns that may predict antenatal and intrapartum neural injury. *Semin Pediatr Neurol*, 28(3):3–16, 2018. (Cited on page 17.)
- [114] Sang Lee and Yu-Dong Kim. Sizing of Spray Particles Using Image Processing Techniques. *KSME Intern. J.*, 18:879–894, 2004. (Cited on page 82.)
- [115] Chavdar Levkov, Georgy Mihov, Ratcho Ivanov, Ivan Daskalov, Ivaylo Christov, and Ivan Dotsinsky. Removal of power-line interference from the ECG: a review of the subtraction procedure. *BioMedical Engineering OnLine*, 4(1):50, 2005. (Cited on page 35.)
- [116] Q Li, R G Mark, and G D Clifford. Robust heart rate estimation from multiple asynchronous noisy sources using signal quality indices and a Kalman filter. *Physiological measurement*, 29(1):15–32, jan 2008. (Cited on pages 37 and 39.)
- [117] Qiao Li, Cadathur Rajagopalan, and Gari D Clifford. A machine learning approach to multi-level ECG signal quality classification. *Computer methods and programs in biomedicine*, 117(3):435–447, dec 2014. (Cited on page 40.)
- [118] S L Lima-Herrera, C Alvarado-Serrano, and P R Hernández-Rodríguez. Fetal ECG extraction based on adaptive filters and Wavelet Transform: Validation and application in fetal heart rate variability analysis. In *2016 13th International Conference on Electrical Engineering, Computing Science and Automatic Control (CCE)*, pages 1–6, 2016. (Cited on pages 36 and 116.)
- [119] D B Lindsley. Heart and brain potentials of human fetuses in utero. By Donald B. Lindsley, 1942. *The American journal of psychology*, 100(3-4):641–646, 1987. (Cited on page 30.)
- [120] Chengyu Liu, Xiangyu Zhang, Lina Zhao, Feifei Liu, Xingwen Chen, Yingjia Yao, and Jianqing Li. Signal Quality Assessment and Lightweight

- QRS Detection for Wearable ECG SmartVest System. *IEEE Internet of Things Journal*, PP:1, 2018. (Cited on page 142.)
- [121] Guangchen Liu and Yihui Luan. An adaptive integrated algorithm for non-invasive fetal ECG separation and noise reduction based on ICA-EEMD-WS. *Medical & biological engineering & computing*, 53(11):1113–1127, nov 2015. (Cited on page 36.)
- [122] Selma Alves Valente do Amaral Lopes, Isabel Cristina Britto Guimarães, Sofia Fontes de Oliva Costa, Angelina Xavier Acosta, Kyoko Abe Sandes, and Carlos Maurício Cardeal Mendes. Mortality for critical congenital heart diseases and associated risk factors in newborns. a cohort study. *Arquivos brasileiros de cardiologia*, 111(5):666–673, nov 2018. (Cited on page 8.)
- [123] V Magagnin, L Delfino, S Cerutti, M Turiel, and E G Caiani. Nearly automated analysis of coronary Doppler flow velocity from transthoracic ultrasound images: validation with manual tracings. *Medical & Biological Engineering & Computing*, 45(5):483–493, 2007. (Cited on pages xiii, 44, 72, 74, 76, 82, 84, 98, and 106.)
- [124] A Mahajan, A Henry, N Meriki, E Hernandez-Andrade, F Crispi, L Wu, and A W Welsh. The (Pulsed-Wave) Doppler Fetal Myocardial Performance Index: Technical Challenges, Clinical Applications and Future Research. *Fetal Diagnosis and Therapy*, 38(1):1–13, 2015. (Cited on pages 45 and 46.)
- [125] Stéphane Mallat. *A wavelet tour of signal processing*. Elsevier, 1999. (Cited on pages 123 and 124.)
- [126] N. Marchon and G. Naik. Electrode positioning for monitoring fetal ecg: A review. In *2015 International Conference on Information Processing (ICIP)*, pages 5–10, Dec 2015. (Cited on page 54.)
- [127] Ariane J. Marelli, Raluca Ionescu-Ittu, Andrew S. Mackie, Liming Guo, Nandini Dendukuri, and Mohammed Kaouache. Lifetime Prevalence of

- Congenital Heart Disease in the General Population From 2000 to 2010. *Circulation*, 130(9):749–756, aug 2014. (Cited on page 8.)
- [128] Suzanna M M Martens, Chiara Rabotti, Massimo Mischi, and Rob J Sluijter. A robust fetal ECG detection method for abdominal recordings. *Physiological Measurement*, 28(4):373–388, 2007. (Cited on pages 63 and 144.)
- [129] R Martinek, R Kahankova, H Skutova, P Koudelka, J Zidek, and J Koziorek. Adaptive signal processing techniques for extracting abdominal fetal electrocardiogram. In *2016 10th International Symposium on Communication Systems, Networks and Digital Signal Processing (CSNDSP)*, pages 1–6, 2016. (Cited on pages 36 and 116.)
- [130] Radek Martinek, Radana Kahankova, Jan Nedoma, Marcel Fajkus, and Kristýna Cholevová. Fetal ECG Preprocessing Using Wavelet Transform. pages 39–43, 2018. (Cited on pages 35 and 124.)
- [131] J P Martinez, R Almeida, S Olmos, A P Rocha, and P Laguna. A wavelet-based ECG delineator: evaluation on standard databases. *IEEE Transactions on Biomedical Engineering*, 51(4):570–581, 2004. (Cited on page 128.)
- [132] Faezeh Marzbanrad, Ahsan H Khandoker, Yoshitaka Kimura, Marimuthu Palaniswami, and Gari D Clifford. Assessment of Fetal Development Using Cardiac Valve Intervals. *Frontiers in physiology*, 8:313, 2017. (Cited on page 45.)
- [133] Faezeh Marzbanrad, Lisa Stroux, and Gari D Clifford. Cardiotocography and beyond: A review of one-dimensional doppler ultrasound application in fetal monitoring. *Physiological Measurement*, 39, 07 2018. (Cited on page 10.)
- [134] Jay W Mason, David G Strauss, Martino Vaglio, and Fabio Badilini. Correction of the QRS duration for heart rate. *Journal of electrocardiology*, 54:1–4, 2019. (Cited on pages 35 and 54.)

- [135] Debabrata Maulik, Navin C Nanda, and Vasant D Saini. Fetal doppler echocardiography: Methods and characterization of normal and abnormal hemodynamics. *American Journal of Cardiology*, 53(4):572–578, feb 1984. (Cited on page 43.)
- [136] Dev Maulik, Navin C Nanda, Devika Maulik, and Gustavo Vilchez. A brief history of fetal echocardiography and its impact on the management of congenital heart disease. *Echocardiography (Mount Kisco, N.Y.)*, 34(12):1760–1767, dec 2017. (Cited on page 43.)
- [137] Nana Aba Mensah-Brown, Ronald T Wakai, Bageshree Cheulkar, Shardha Srinivasan, and Janette F Strasburger. Assessment of left ventricular pre-ejection period in the fetus using simultaneous magnetocardiography and echocardiography. *Fetal diagnosis and therapy*, 28(3):167–174, 2010. (Cited on page 45.)
- [138] Michel Misiti, Yves Misiti, Georges Oppenheim, and Jean-Michel Poggi. *Wavelets and their Applications*, volume 330. Wiley Online Library, 2007. (Cited on pages 123, 124, and 125.)
- [139] S. Muceli, D. Pani, and L. Raffo. Non-invasive real-time fetal ECG extraction - A block-on-line DSP implementation based on the JADE algorithm. In *BIOSIGNALS 2008 - Proceedings of the 1st International Conference on Bio-inspired Systems and Signal Processing*, volume 2, pages 458–463, 2008. (Cited on page 114.)
- [140] Guy P Nason and Bernard W Silverman. The stationary wavelet transform and some statistical applications. In *Wavelets and statistics*, pages 281–299. Springer, 1995. (Cited on page 124.)
- [141] K Nicolaides, G Rizzo, and K Hecher. *Doppler in Obstetrics*. The Fetal Medicine Foundation, 2002. (Cited on pages 23 and 25.)
- [142] M. Nii, R M Hamilton, L Fenwick, J C P Kingdom, K S Roman, and E T Jaeggi. Assessment of fetal atrioventricular time intervals by tissue

- doppler and pulse doppler echocardiography: normal values and correlation with fetal electrocardiography. *Heart*, 92(12):1831–1837, 2006. (Cited on page 26.)
- [143] Saman Noorzadeh, Bertrand Rivet, and Pierre-Yves Gumery. A multi-modal approach using a non-parametric model to extract fetal ecg. pages 832–836, 04 2015. (Cited on page 36.)
- [144] T F Oostendorp, A van Oosterom, and H W Jongsma. Electrical properties of tissues involved in the conduction of foetal ECG. *Med Biol Eng Comput*, 27(3):322–324, May 1989. (Cited on pages 2, 16, 30, and 52.)
- [145] T F Oostendorp, A van Oosterom, and H W Jongsma. The fetal ECG throughout the second half of gestation. *Clinical Physics and Physiological Measurement*, 10(2):147–160, may 1989. (Cited on page 63.)
- [146] Thom Oostendorp, A van Oosterom, and H W Jongsma. The effect of changes in the conductive medium of the fetal ecg throughout gestation. *Clinical physics and physiological measurement*, 10:11–20, 1989. (Cited on pages 2 and 52.)
- [147] Christina Orphanidou, Timothy Bonnici, Peter Charlton, David Clifton, David Vallance, and Lionel Tarassenko. Signal-quality indices for the electrocardiogram and photoplethysmogram: derivation and applications to wireless monitoring. *IEEE journal of biomedical and health informatics*, 19(3):832–838, may 2015. (Cited on pages 39, 40, and 142.)
- [148] Nobuyuki Otsu. A threshold selection method from gray-level histograms. *Systems, Man and Cybernetics, IEEE Transactions on*, 9:62–66, 1979. (Cited on page 82.)
- [149] J Pan and W J Tompkins. A Real-Time QRS Detection Algorithm. *IEEE Transactions on Biomedical Engineering*, BME-32(3):230–236, 1985. (Cited on pages 129 and 139.)
- [150] S V Pandit. ECG baseline drift removal through STFT. In *Proceedings of 18th Annual International Conference of the IEEE Engineering in*

- Medicine and Biology Society*, volume 4, pages 1405–1406 vol.4, 1996. (Cited on page 35.)
- [151] D Pani, S Argiolas, and L Raffo. A DSP algorithm and system for real-time fetal ECG extraction. In *2008 Computers in Cardiology*, pages 1065–1068, 2008. (Cited on page 114.)
- [152] JinHyeong Park, S Kevin Zhou, John Jackson, and Dorin Comaniciu. Automatic Mitral Valve Inflow Measurements from Doppler Echocardiography. In Dimitris Metaxas, Leon Axel, Gabor Fichtinger, and Gábor Székely, editors, *Medical Image Computing and Computer-Assisted Intervention – MICCAI 2008*, pages 983–990, Berlin, 2008. Springer Berlin Heidelberg. (Cited on page 44.)
- [153] Hemanth Peddaneni. Comparison of algorithms for fetal ecg extraction. 2004. (Cited on page 63.)
- [154] Donald B Percival and Andrew T Walden. *Wavelet methods for time series analysis*, volume 4. Cambridge university press, 2006. (Cited on page 125.)
- [155] J-C Pesquet, Hamid Krim, and Hervé Carfantan. Time-invariant orthonormal wavelet representations. *IEEE transactions on signal processing*, 44(8):1964–1970, 1996. (Cited on page 124.)
- [156] M Peters, J Crowe, J F Pieri, H Quartero, B Hayes-Gill, D James, J Stinstra, and S Shakespeare. Monitoring the fetal heart non-invasively: a review of methods. *Journal of perinatal medicine*, 29(5):408–416, 2001. (Cited on page 10.)
- [157] Stephanie Pildner von Steinburg, Anne-Laure Boulesteix, Christian Lederer, Stefani Grunow, Sven Schiermeier, and Hatzmann. What is the "normal" fetal heart rate? *PeerJ*, 1:e82–e82, jun 2013. (Cited on pages 24 and 85.)

- [158] M A Pozniak, J A Zagzebski, and K A Scanlan. Spectral and color Doppler artifacts. *Radiographics : a review publication of the Radiological Society of North America, Inc*, 12(1):35–44, jan 1992. (Cited on page 86.)
- [159] Swarnalatha Rajaguru and Prasad D.V. *A Novel Technique for Extraction of FEEG using Multi Stage Adaptive Filtering*, volume 10. apr 2010. (Cited on pages 36 and 116.)
- [160] P Randall, S Brealey, S Hahn, K S Khan, and J M Parsons. Accuracy of fetal echocardiography in the routine detection of congenital heart disease among unselected and low risk populations: a systematic review. *BJOG: An International Journal of Obstetrics & Gynaecology*, 112(1):24–30, 2005. (Cited on page 43.)
- [161] S. Ravindrakumar and K. Bommannaraja K. Certain investigation on de-noising the multichannel abdominal ecg signal using various adaptive noise suppression techniques. *Australian Journal of Basic and Applied Sciences*, 9(5):372–380, 2015. (Cited on pages 36, 55, 114, and 116.)
- [162] S. Ravindrakumar and K. B. Raja. Fetal ecg extraction and enhancement in prenatal monitoring — review and implementation issues. In *Trends in Information Sciences Computing(TISC2010)*, pages 16–20, Dec 2010. (Cited on page 63.)
- [163] Rui Rodrigues. Fetal beat detection in abdominal ECG recordings: global and time adaptive approaches. *Physiological Measurement*, 35(8):1699–1711, 2014. (Cited on page 116.)
- [164] Maria Romano, Luigi Iuppariello, Alfonso Maria Ponsiglione, Giovanni Improta, Paolo Bifulco, and Mario Cesarelli. Frequency and Time Domain Analysis of Foetal Heart Rate Variability with Traditional Indexes: A Critical Survey. *Computational and mathematical methods in medicine*, 2016:9585431, 2016. (Cited on page 17.)
- [165] Michael Rooijackers, Chiara Rabotti, Hinke Lau, Guid Oei, Jan Bergmans, and Massimo Mischi. Feasibility study of a new method for low-complexity

- fetal movement detection from abdominal ecg recordings. *IEEE journal of biomedical and health informatics*, 20, 07 2015. (Cited on page 18.)
- [166] Michael J Rooijackers, Chiara Rabotti, S Guid Oei, and Massimo Mischi. Low-complexity R-peak detection for ambulatory fetal monitoring. *Physiological measurement*, 33(7):1135–1150, jul 2012. (Cited on page 63.)
- [167] M.J. Rooijackers, S. Song, C. Rabotti, S.G. Oei, J.W.M. Bergmans, E. Cantatore, and M. Mischi. Influence of electrode placement on signal quality for ambulatory pregnancy monitoring. *Computational and Mathematical Methods in Medicine*, 2014:960980–1/12, 2014. (Cited on page 63.)
- [168] K G Rosen and I Kjellmer. Changes in the fetal heart rate and ECG during hypoxia. *Acta physiologica Scandinavica*, 93(1):59–66, jan 1975. (Cited on page 30.)
- [169] Andreas F Ruckstuhl, Matthew P Jacobson, Robert W Field, and James A Dodd. Baseline subtraction using robust local regression estimation. *Journal of Quantitative Spectroscopy and Radiative Transfer*, 68(2):179–193, 2001. (Cited on page 35.)
- [170] Adalina Sacco, Javaid Muglu, Ramesan Navaratnarajah, and Matthew Hogg. ST analysis for intrapartum fetal monitoring. *The Obstetrician & Gynaecologist*, 17:5–12, 2014. (Cited on pages 10, 16, and 18.)
- [171] R Sameni. A linear Kalman Notch Filter for Power-Line Interference Cancellation. In *The 16th CSI International Symposium on Artificial Intelligence and Signal Processing (AISP 2012)*, pages 604–610, 2012. (Cited on page 35.)
- [172] Reza Sameni. *The Open-Source Electrophysiological Toolbox (OSET), version 3.14*, 2018. (Cited on pages 55 and 59.)
- [173] Reza Sameni and Gari D. Clifford. A review of fetal ecg signal processing; issues and promising directions. *Open pacing, electrophysiology & therapy journal*, 3:4–20, 2010. (Cited on pages 15, 31, 32, 54, and 114.)

- [174] Reza Sameni, Christian Jutten, and Mohammad B Shamsollahi. A deflation procedure for subspace decomposition. *Signal Processing, IEEE Transactions on*, 58(4):2363–2374, 2010. (Cited on page 56.)
- [175] Jeremy P Campbell Sarah K Griffiths. Placental structure, function and drug transfer. *Continuing Education in Anaesthesia Critical Care & Pain*, 15(2):84–89, 2015. (Cited on page 1.)
- [176] U Satija, B Ramkumar, and M S Manikandan. A Review of Signal Processing Techniques for Electrocardiogram Signal Quality Assessment. *IEEE Reviews in Biomedical Engineering*, 11:36–52, 2018. (Cited on pages 40 and 142.)
- [177] Ali H Sayed. *Adaptive Filters*. Wiley-IEEE Press, 2008. (Cited on page 116.)
- [178] Uwe Schneider, Franziska Bode, Alexander Schmidt, Samuel Nowack, Anja Rudolph, Eva-Maria Doelcker, Peter Schlattmann, Theresa Götz, and Dirk Hoyer. Developmental milestones of the autonomic nervous system revealed via longitudinal monitoring of fetal heart rate variability. *PLOS ONE*, 13:1–13, 07 2018. (Cited on page 17.)
- [179] N. ScottAdzick. Open fetal surgery for life-threatening fetal anomalies. *Semin Fetal Neonat Med.*, 15:1–8, 2009. (Cited on page 1.)
- [180] Chunshi Sha, Jian Hou, Hongxia Cui, and Jianxin Kang. Gray Level-Median Histogram Based 2D Otsu's Method. pages 30–33, 2015. (Cited on pages 53 and 82.)
- [181] Maha Shadaydeh, Yegui Xiao, and Rabab Ward. Extraction of fetal ECG using adaptive Volterra filters. In *European Signal Processing Conference*, 2008. (Cited on pages 36 and 116.)
- [182] S A Shakespeare, J A Crowe, B R Hayes-Gill, K Bhogal, and D K James. The information content of Doppler ultrasound signals from the fetal heart. *Medical & biological engineering & computing*, 39(6):619–626, nov 2001. (Cited on pages 10, 45, and 46.)

- [183] O Shechner, M Scheinowitz, M S Feinberg, and H Greenspan. Automated method for Doppler echocardiography image analysis. In *2004 23rd IEEE Convention of Electrical and Electronics Engineers in Israel*, pages 177–180, 2004. (Cited on page 44.)
- [184] P Shechner, M Sheinovitz, M Feinberg, and H Greenspan. Image analysis of Doppler echocardiography for patients with atrial fibrillation. In *2004 2nd IEEE International Symposium on Biomedical Imaging: Nano to Macro (IEEE Cat No. 04EX821)*, pages 488–491 Vol. 1, 2004. (Cited on page 44.)
- [185] M G Signorini, Andrea Fanelli, and Giovanni Magenes. Monitoring Fetal Heart Rate during Pregnancy: Contributions from Advanced Signal Processing and Wearable Technology. *Computational and mathematical methods in medicine*, 2014:707581, 2014. (Cited on page 17.)
- [186] Maria G Signorini, Giovanni Magenes, Sergio Cerutti, and Domenico Arduini. Linear and nonlinear parameters for the analysis of fetal heart rate signal from cardiotocographic recordings. *IEEE transactions on biomedical engineering*, 50(3):365–374, mar 2003. (Cited on pages 10, 17, and 59.)
- [187] Ikaro Silva, Joachim Behar, Reza Sameni, Tingting Zhu, Julien Oster, Gari D Clifford, and George B Moody. Noninvasive Fetal ECG: the PhysioNet/Computing in Cardiology Challenge 2013. *Computing in cardiology*, 40:149–152, mar 2013. (Cited on pages 32, 34, and 116.)
- [188] John M Simpson. Impact of fetal echocardiography. *Annals of pediatric cardiology*, 2(1):41–50, 2009. (Cited on pages 8 and 21.)
- [189] Steven W Smith. *The Scientist and Engineer's Guide to Digital Signal Processing*. California Technical Publishing, San Diego, CA, USA, 1997. (Cited on page 79.)
- [190] Vinayak Smith, Senthuran Arunthavanathan, Amrish Nair, Diane Ansermet, Fabricio da Silva Costa, and Euan Morrison Wallace. A systematic

- review of cardiac time intervals utilising non-invasive fetal electrocardiogram in normal fetuses. *BMC pregnancy and childbirth*, 18(1):370, sep 2018. (Cited on page 42.)
- [191] Leif Sörnmo and Pablo Laguna. *Bioelectrical signal processing in cardiac and neurological applications*, volume 8. Academic Press, 2005. (Cited on pages 123 and 124.)
- [192] Janette F Strasburger, Bageshree Cheulkar, and Ronald T Wakai. Magnetocardiography for fetal arrhythmias. *Heart rhythm*, 5(7):1073–1076, jul 2008. (Cited on page 10.)
- [193] Lisa Stroux, Christopher Redman, Antoniya Georgieva, Stephen J. Payne, and Gari D. Clifford. Doppler-based fetal heart rate analysis markers for the detection of early intrauterine growth restriction. *Acta Obstetricia et Gynecologica Scandinavica*, 96, 09 2017. (Cited on page 17.)
- [194] M Suganthy and S Manjula. Enhancement of SNR in fetal ECG signal extraction using combined SWT and WLSR in parallel EKF. *Cluster Computing*, mar 2018. (Cited on page 36.)
- [195] Eleonora Sulas, Emanuele Ortu, Luigi Raffo, Monica Urru, Roberto Tumbarello, and Danilo Pani. Automatic Recognition of Complete Atrioventricular Activity in Fetal Pulsed-Wave Doppler Signals. *Annual International Conference of the IEEE Engineering in Medicine and Biology Society. IEEE Engineering in Medicine and Biology Society. Annual Conference*, 2018:917–920, jul 2018. (Cited on pages 44, 75, 76, 82, and 90.)
- [196] Eleonora Sulas, Emanuele Ortu, Monica Urru, Alessandra Cadoni, Roberto Tumbarello, Luigi Raffo, and Danilo Pani. Fetal Pulsed-Wave Doppler Atrioventricular Activity Detection by Envelope Extraction and Processing. In *Computing in Cardiology - vol. 45*, 2018. (Cited on pages xiii, 44, 53, 72, 75, 82, 83, 84, 85, 90, 91, 101, and 106.)
- [197] Borys Surawicz, Rory Childers, Barbara J Deal, and Leonard S Gettes. AHA/ACCF/HRS Recommendations for the Standardization and Inter-

- pretation of the Electrocardiogram. *Circulation*, 119(10):e235–e240, 2009. (Cited on page 139.)
- [198] B. Suriseti and R. M. Dansereau. Multi-modal fetal ecg extraction using multi-kernel gaussian processes. In *2017 IEEE Global Conference on Signal and Information Processing (GlobalSIP)*, pages 943–947, Nov 2017. (Cited on page 36.)
- [199] R Swarnalath and Dr. Vishnu Prasad. Maternal ECG Cancellation in Abdominal Signal Using ANFIS and Wavelets. 2010. (Cited on page 36.)
- [200] T Syeda-Mahmood, P Turaga, D Beymer, F Wang, A Amir, H Greenspan, and K Pohl. Shape-based similarity retrieval of Doppler images for clinical decision support. In *2010 IEEE Computer Society Conference on Computer Vision and Pattern Recognition*, pages 855–862, 2010. (Cited on pages xiii, 44, 72, 73, 76, 82, 83, 84, 97, and 106.)
- [201] A T. Walden and A Contreras Cristan. *The phase-corrected undecimated discrete wavelet packet transform and its application to interpreting the timing of events*, volume 454. aug 1998. (Cited on page 125.)
- [202] Dragoş Taralunga, Georgeta Ungureanu, Ilinca Gussi, Rodica Strungaru, and Werner Wolf. Fetal ECG Extraction from Abdominal Signals: A Review on Suppression of Fundamental Power Line Interference Component and Its Harmonics. *Computational and mathematical methods in medicine*, 2014:239060, feb 2014. (Cited on page 36.)
- [203] Myles J O Taylor, Mark J Smith, Matthew Thomas, Andrew R Green, Floria Cheng, Salome Oseku-Afful, Ling Y Wee, Nicholas M Fisk, and Helena M Gardiner. Non-invasive fetal electrocardiography in singleton and multiple pregnancies. *BJOG : an international journal of obstetrics and gynaecology*, 110(7):668–678, jul 2003. (Cited on pages 42, 63, 139, 141, and 142.)
- [204] Myles J O Taylor, Matthew J Thomas, Mark J Smith, Salome Oseku-Afful, Nicholas M Fisk, Andrew R Green, Sara Paterson-Brown, and He-

- lena M Gardiner. Non-invasive intrapartum fetal ECG: preliminary report. *BJOG : an international journal of obstetrics and gynaecology*, 112(8):1016–1021, aug 2005. (Cited on page 42.)
- [205] CHUWA TEI. New non-invasive index for combined systolic and diastolic ventricular function. *J Cardiol.*, 26(2):135–136, 1995. (Cited on page 26.)
- [206] H.J.M ter Brake, A.P Rijpma, J.G Stinstra, J Borgmann, H.J Holland, H.J.G. Krooshoop, M.J Peters, J Flokstra, Rik Quartero, and Horst Rogalla. Fetal magnetocardiography: Clinical relevance and feasibility. *Physica C: Superconductivity*, 368:10–17, 03 2002. (Cited on page 10.)
- [207] Snehal G. Thalkar and Dhananjay Upasani. Various techniques for removal of power line interference from ecg signal. 2013. (Cited on page 35.)
- [208] V Tomek, J Janousek, O Reich, J Gilik, R A Gebauer, and J Skovranek. Atrioventricular conduction time in fetuses assessed by Doppler echocardiography. *Physiological research*, 60(4):611–616, 2011. (Cited on page 26.)
- [209] J Tschirren, R M Lauer, and M Sonka. Automated analysis of Doppler ultrasound velocity flow diagrams. *IEEE Transactions on Medical Imaging*, 20(12):1422–1425, 2001. (Cited on pages xiii, 44, 72, 73, 76, 77, 80, 83, 84, 97, and 106.)
- [210] B Tutschek and K G Schmidt. Pulsed-wave tissue Doppler echocardiography for the analysis of fetal cardiac arrhythmias. *Ultrasound in Obstetrics & Gynecology*, 38(4):406–412, 2011. (Cited on pages 22 and 43.)
- [211] Mihaela Ungureanu, Johannes W Bergmans, Massimo Mischi, S Guid Oei, and Rodica Strungaru. Improved method for fetal heart rate monitoring. *Conference proceedings : ... Annual International Conference of the IEEE Engineering in Medicine and Biology Society. IEEE Engineering in Medicine and Biology Society. Annual Conference*, 6:5916–5919, 2005. (Cited on page 63.)

- [212] J A van Alsté, W van Eck, and O E Herrmann. ECG baseline wander reduction using linear phase filters. *Computers and Biomedical Research*, 19(5):417–427, 1986. (Cited on page 35.)
- [213] Denise van der Linde, Elisabeth E M Konings, Maarten A Slager, Maarten Witsenburg, Willem A Helbing, Johanna J M Takkenberg, and Jolien W Roos-Hesselink. Birth prevalence of congenital heart disease worldwide. *Journal of the American College of Cardiology*, 58(21):2241 LP – 2247, nov 2011. (Cited on page 8.)
- [214] Lucas J van Vliet, Ian T Young, and Guus L Beckers. A nonlinear laplace operator as edge detector in noisy images. *Computer Vision, Graphics, and Image Processing*, 45(2):167–195, 1989. (Cited on pages 80 and 81.)
- [215] Vladimir N Vapnik. *The Nature of Statistical Learning Theory*. Springer-Verlag, Berlin, Heidelberg, 1995. (Cited on pages 91 and 130.)
- [216] R von Borries, J Pierluissi, and H Nazeran. Wavelet Transform-Based ECG Baseline Drift Removal for Body Surface Potential Mapping. *Annual International Conference of the IEEE Engineering in Medicine and Biology Society. IEEE Engineering in Medicine and Biology Society. Annual Conference*, 4:3891–3894, 2005. (Cited on page 35.)
- [217] R Vullings, C H L Peters, R J Sluijter, M Mischi, S G Oei, and J W M Bergmans. Dynamic segmentation and linear prediction for maternal ECG removal in antenatal abdominal recordings. *Physiological measurement*, 30(3):291–307, mar 2009. (Cited on page 63.)
- [218] Rik Vullings, Chris Peters, Massimo Mischi, Guid Oei, and Jan Bergmans. Maternal ecg removal from non-invasive fetal ecg recordings. pages 1394–1397, 08 2006. (Cited on page 63.)
- [219] Annette Wacker-Gussmann, Cordula Plankl, Maria Sewald, Karl-Theo Maria Schneider, Renate Oberhoffer, and Silvia M Lobmaier. Fetal cardiac time intervals in healthy pregnancies - an observational study by fetal ECG (Monica Healthcare System). *Journal of perinatal medicine*, 46(6):587–592, aug 2018. (Cited on page 42.)

- [220] Y Wang, Y Fu, and Z He. Fetal Electrocardiogram Extraction Based on Fast ICA and Wavelet Denoising. In *2018 2nd IEEE Advanced Information Management, Communicates, Electronic and Automation Control Conference (IMCEC)*, pages 466–469, 2018. (Cited on page 36.)
- [221] Z Wang, G Slabaugh, M Zhou, and T Fang. Automatic tracing of blood flow velocity in pulsed Doppler images. In *2008 IEEE International Conference on Automation Science and Engineering*, pages 218–222, 2008. (Cited on page 45.)
- [222] Philip A. Warrick, Emily F. Hamilton, Doina Precup, and Robert E. Kearney. Classification of normal and hypoxic fetuses from systems modeling of intrapartum cardiotocography. *IEEE Transactions on Biomedical Engineering*, 57:771–779, 2010. (Cited on page 10.)
- [223] R. Weber, D. Stambach, and E. Jaeggi. Diagnosis and management of common fetal arrhythmias. *J Saudi Heart Assoc*, 23(2):61–66, 2011. (Cited on pages 1, 9, 10, 11, 16, and 23.)
- [224] B. Widrow and S.D. Stearns. Adaptive signal processing. *Prentice-Hall Signal Processing Series*, 52, 1985. (Cited on pages 55, 116, and 148.)
- [225] Bernard Widrow, J. K. Glover, J. M. McCool, John Kaunitz, C. S. Williams, R H Hearn, J. R. Zeidler, Jr. Eugene Dong, and Robert C. Goodlin. Adaptive noise cancelling: Principles and applications. *Proceedings of the IEEE*, 63:1692–1716, 1975. (Cited on pages 30, 36, and 55.)
- [226] Barth William. Cardiac surgery in pregnancy. *Clin Obstet Gynecol.*, 52(4):630–646, 2009. (Cited on page 1.)
- [227] Shuicai Wu, Yanni Shen, Zhuhuang Zhou, Lan Lin, Yanjun Zeng, and Xiaofeng Gao. Research of fetal ECG extraction using wavelet analysis and adaptive filtering. *Computers in Biology and Medicine*, 43(10):1622–1627, oct 2013. (Cited on page 36.)

- [228] Wang XF. The use of fetal echocardiography for pregnancy diagnosis. *Chin J Obstet Gynecol.*, 7:187–190, 1973. (Cited on page 43.)
- [229] V Zarzoso and A K Nandi. Noninvasive fetal electrocardiogram extraction: blind separation versus adaptive noise cancellation. *IEEE Transactions on Biomedical Engineering*, 48(1):12–18, 2001. (Cited on pages 36 and 114.)
- [230] V Zarzoso, A K Nandi, and E Bacharakis. Maternal and foetal ECG separation using blind source separation methods. *IMA journal of mathematics applied in medicine and biology*, 14(3):207–225, sep 1997. (Cited on page 30.)
- [231] Jie-Min Zhang, Qun Guan, Li-Ming Tang, Tie-Bing Liu, Hong-Xing Liu, Xiao-Lin Huang, and Jun-Feng Si. Position difference regularity of corresponding r-wave peaks for maternal ECG components from different abdominal points. *Chinese Physics B*, 23(1):018701, jan 2014. (Cited on page 63.)
- [232] Zhidong Zhao and Yefei Zhang. Sqi quality evaluation mechanism of single-lead ecg signal based on simple heuristic fusion and fuzzy comprehensive evaluation. *Frontiers in physiology*, 9:727, 2018. (Cited on pages 129 and 143.)
- [233] S K Zhou, F Guo, J H Park, G Carneiro, J Jackson, M Brendel, C Simopoulos, J Otsuki, and D Comaniciu. A probabilistic, hierarchical, and discriminant framework for rapid and accurate detection of deformable anatomic structure. In *2007 IEEE 11th International Conference on Computer Vision*, pages 1–8, 2007. (Cited on page 44.)
- [234] S Ziani, A Jbari, and L Belarbi. Fetal electrocardiogram characterization by using only the continuous wavelet transform CWT. In *2017 International Conference on Electrical and Information Technologies (ICEIT)*, pages 1–6, 2017. (Cited on page 36.)
- [235] M Zolgharni, N M Dhutia, G D Cole, M R Bahmanyar, S Jones, S M A Sohaib, S B Tai, K Willson, J A Finegold, and D P Francis. Automated

Aortic Doppler Flow Tracing for Reproducible Research and Clinical Measurements. *IEEE Transactions on Medical Imaging*, 33(5):1071–1082, 2014. (Cited on pages xiii, 44, 72, 74, 76, 82, 83, 84, 97, 102, and 106.)

Acknowledgments

I gratefully acknowledge the Sardinia Regional Government for supporting my PhD research work (P.O.R. F.S.E., European Social Fund 2014-2020).

A sincere thank to my scientific supervisors in Eindhoven, Dr. Rik Vullings and Dr. Massimo Mischi, that guided me during my 10-months of Placedoc in The Netherlands. I acknowledge the Placedoc Mobility Program to support my research abroad.

I wish to thank the team headed by Dr. Roberto Tumbarello, Division of Paediatric Cardiology, AOB Hospital (Cagliari, Italy), for their clinical support. A special thank to Dr. Monica Urru for the time she spent working with me during the last three years.

I would like to give a special thanks to Dr. Reza Sameni, for his technical support in presenting to the audience the dataset described in this PhD work.

I thank Dr. Arnaldo Guimarães Batista and Dr. Bertrand Rivet for the efforts they made in reading and reviewing my thesis.

I would also like to thank my colleagues in University of Cagliari and Eindhoven University of Technology for the time spent together. A special thank to Giulia Baldazzi, with whom I productively collaborated during the last months of my research work.

Last but not least, I would like to thank my supervisors Dr. Danilo Pani and Dr. Luigi Raffo. Special gratitude to Dr. Danilo Pani that has been an incomparable scientific and life guide.

Curriculum Vitae



Eleonora Sulas received the B.Sc. degree (magna cum laude) in biomedical engineering from the University of Cagliari, Italy, in 2014, and the M.Sc. degree in biomedical engineering from the Politecnico of Torino, Italy, in 2016. She has been pursuing the Ph.D. degree in electronic and computer engineering with the Department of Electrical and Electronic Engineering, University of Cagliari, since October 2016. Her main research activity is focused on biomedical signal processing algorithms, non-invasive fetal ECG extraction, and embedded systems.

If you are interested in the project, check the following link (minute 1.13): <http://www.raai.it/dl/RaiTV/programmi/media/ContentItem-db6c5b65-f3b3-4f30-b307-075bd0d64e1e.html>.

Work Experience

Self-employed contract as Embedded Engineer Jan 2019 - Feb 2019

University of Cagliari, Italy

Hardware and firmware implementation of an electronic board to transmit (via Bluetooth) and to acquire pressure measurement in smart garments.

Self-employed contract as Embedded Engineer May 2018 - June 2018

University of Cagliari, Italy

Hardware and firmware implementation of an electronic board to transmit, via Bluetooth, and acquire ECG and respiration signals, heart and respiration rate, with real-time signal processing on board.

Awards

Awarded best graduating student, Università di Cagliari, 2014.

Best Poster in International Joint Conference on Biomedical Engineering Systems and Technologies (Biostec), Funchal, Madeira, Portugal, Jan. 2018.

Patent applications

- P3031IT00 The present invention refers to a sensorized garment in contact with the skin that detects biometric parameters.
- P3032IT00 The actual invention provides a composition for a conductive polymeric material suitable for making electrodes for recording electrophysiological signals.